AFOSR 67-0519

CRUSTAL STUDIES
CONTINUATION OF BASIC RESEARCH IN CRUSTAL STUDIES
ANNUAL REPORT

Max K. Miller, Project Scientist
FL 7-5411 Ext. 317

A. Frank Linville Hugh K. Harris

TEXAS INSTRUMENTS INCORPORATED
Science Services Division
P.O. Box 5621
Dallas, Texas 75222

Contract No.: AF 49(638)-1588
Date of Contract: 1 January 1966
Contract Expiration Date: 30 June 1967
Amount of Contract: $110,420.00

Prepared for

AIR FORCE OFFICE OF SCIENTIFIC RESEARCH (SRPG)
1400 Wilson Boulevard
Arlington, Virginia 22209

Sponsored by

ADVANCED RESEARCH PROJECTS AGENCY
ARPA Order No. 292, Amendment 20
Project Code No. 8652

30 January 1967

AFOSR 67-0519

Distribution of this document is unlimited

CRUSTAL STUDIES
CONTINUATION OF BASIC RESEARCH IN CRUSTAL STUDIES
ANNUAL REPORT

Max K. Miller, Project Scientist
FL 7-5411 Ext. 317

A. Frank Linville Hugh K. Harris

TEXAS INSTRUMENTS INCORPORATED
Science Services Division
P.O. Box 5621
Dallas, Texas 75222

Contract No.: AF 49(638)-1588
Date of Contract: 1 January 1966
Contract Expiration Date: 30 June 1967
Amount of Contract: $110,420.00

Prepared for

AIR FORCE OFFICE OF SCIENTIFIC RESEARCH (SRPG)
1400 Wilson Boulevard
Arlington, Virginia 22209

Sponsored by

ADVANCED RESEARCH PROJECTS AGENCY
ARPA Order No. 292, Amendment 20
Project Code No. 8652

30 January 1967

Requests for additional copies by agencies of the Department of Defense, their contractors, or other government agencies should be directed to

DEFENSE DOCUMENTATION CENTER (DDC)
CAMERON STATION
ALEXANDRIA, VIRGINIA 22314

Department of Defense contractors must be established by the cognizant military agency of their project or contract.

All other persons and organizations should apply to the

Clearinghouse for Federal Scientific and Technical Information (CFSTI)
Sills Building
5285 Port Royal Road
Springfield, Virginia 22151

ABSTRACT

The work performed under Contract AF 49(638)-1588 falls into two categories: (1) mode theory and applications and (2) scattering studies.

Crustal models have been constructed for the Tonto Forest Seismological Observatory (TFO) in Arizona and the Large Aperature Seismic Array (LASA) in Montana.

A long period event recorded at TFO with epicenter in Southern California was time partitioned and Rayleigh wave dispersion in the frequency range of 0.025 to 0.175 was derived. With these data, the adequacy of the TFO model crust has been substantiated at low frequencies by a comparison of theoretical and experimental dispersion curves.

The mode separation studies include the design and application of mode separation processors to separate the M_{2i} mode from the Rayleigh mode in the frequency range 0.0 to 0.25 cps by use of field data.

An analog model having a crustal layer with an abrupt thickness change (3 cm to 5 cm) was used for scattering studies. The source was located on the surface of the model. The dominant leaking mode of propagation in the thin end of the model is PL_{22}. Theory predicts that this energy is primarily scattered into the leaking mode PL_{23} in the 5-cm end. There is also some evidence of wave propagation which is not readily explained in terms of modes.

Filtering techniques were used to analyze energy scattered by small surface irregularities. The primary scattered energy is a reflection of a portion of the incident Rayleigh wave.

This research was supervised by Dr. Milo M. Backus

The principal authors of this report are

Max K. Miller
Hugh K. Harris
A. Frank Linville

Stanley J. Laster was program manager for this project until September 1966. He has been available for consultation since that date and has offered suggestions for the preparation of this report.

TABLE OF CONTENTS

LIST OF TABLES

LIST OF TABLES (CONTD)

LIST OF ILLUSTRATIONS

LIST OF ILLUSTRATIONS (CONTD)

LIST OF ILLUSTRATIONS (CONTD)

LIST OF ILLUSTRATIONS (CONTD)

LIST OF ILLUSTRATIONS (CONTD)

LIST OF ILLUSTRATIONS (CONTD)

BLANK PAGE

SECTION I
SUMMARY

This annual technical report deals with work performed during the period 1 January 1966 to 31 December 1966. The work was divided into two major areas. Section II is a discussion of mode theory and its applications, and scattering due to inhomogeneities is discussed in Section III.

A. MODE THEORY AND APPLICATION

Applications of theoretical computations which lead to modal seismograms for a given crustal section of the earth are discussed in this report.

Theoretical crustal models were constructed for the Tonto Forest Seismological Observatory (TFO) and for the Large Aperature Seismic Array (LASA). The model used for TFO consisted of four layers and a half-space. The 5-layer model crust for LASA is based on measurements of Steinhart and Meyer.[1]

A long-period event with epicenter in Southern California recorded at TFO was time-partitioned, and the Rayleigh wave dispersion in the frequency range 0.025 to 0.175 cps was derived. Theoretical and experimental dispersion curves were compared at these frequencies. The model was perturbed slightly, and no significant changes resulted.

Theoretical computations precict that 10 higher-order normal modes may be expected in the TFO crust for frequencies up to 1.0 cps, and their amplitudes will be relatively small compared to the amplitude of M_{11}. The long period field recordings available were band-limited in such a manner that only the two lowest order modes may be observed.

Mode separation processors were designed and applied to separate the M_{21} mode from the M_{11} mode in the frequency range 0.0 to 0.25 cps using a TFO event whose epicenter was in Jalisco, Mexico. Two array processing schemes were used for mode separation. The first makes use of the frequency-velocity and amplitude relationships, and the second makes additional use of the 2-component (horizontal-vertical) relationships.

The theoretically computed mode separation processors did not reject the dominant M_{11} mode as much as was predicted by the computed filter response. Further investigation of the Jalisco event revealed that the Rayleigh mode had anomalous f-k characteristics; i.e., the Rayleigh mode dispersion estimates computed between various pairs of stations were inconsistent.

B. SCATTERING STUDIES

Analog models may be used in order to verify the theory and understanding of elastic wave propagation. In addition, these laboratory studies, although somewhat idealized, can be performed to give insight into the nature of practical geophysical problems.

Scattering studies were performed using an anlog model having a crustal layer with an abrupt thickness change (transition zone). There is a well developed leaking mode (PL_{22}) propagating in the thin end. Theory indicates that this PL_{22} mode in the thin end approximately corresponds to the PL_{23} mode in the thick end.

The shear mode portion of the recording shows a definite decrease in velocity occuring just past the transition zone. Theoretical dispersion curves show that if M_{21} on the thin end is scattered into M_{21} on the thick end, a decrease in phase veloctiy at each frequency results. Frequency-wavenumber analysis was used in an attempt to measure this velocity change.

SECTION II

MODE THEORY AND APPLICATIONS

A. DISCUSSION OF THE MODE THEORY

Three fairly distinct applications of theoretical computations leading to modal seismograms for selected regions of the earth's crust, which will be discussed in this section, are as follows:

- Synthetic seismograms can be constructed and compared with laboratory recordirgs from controlled analog models
- A set of mode rejection filters can be designed to attenuate ambient surface wave noise while simultaneously passing any significant signal energy present
- A model is assumed to possess the correct average properties of the earth's crust and then is tested by requiring the theoretical dispersion curves to agree with experimental dispersion curves

Our understanding of elastic wave propagation in a plane-layered medium is sufficiently complete at this time to justify the construction of synthetic seismograms to be compared in a feature-for-feature manner with laboratory recordings from controlled analog models.[2] In this way, layer structure may be studied without interference from the many geologic anomalies present in the real world.

A further extension of this approach is the investigation of configurations typifying lateral geologic nonuniformities by reproducing their essential features in an analog model. This model can be analyzed mathematically through perturbing and combining the modal solutions of simpler plane-layered crustal representations. One persistent difficulty in such simulation efforts is in adequately defining the source and receiver properties, a problem which is even more formidable when dealing with actual field data.

Under the assumption that much of the ambient surface wave noise measured by an array is regionally generated modal energy, a set of mode rejection filters can be designed to attenuate this noise while simultaneously passing any significant signal energy present, e.g., the P phase. If the signal is chosen to be a particular mode, such as the second order M_{21} shear mode (perhaps to be associated with the L_g phase of seismology), and the other modes are taken to be noise, one has the mode separation problem discussed by Laster and Linville.[3]

Theoretical dispersion curves for the modes completely specify their frequency-wavenumber coordinates (Figure II-1). These coordinates are adequate for multichannel filter design. Indeterminancy of source and receiver properties is not a crucial factor, although it is desirable and possible to include physically reasonable source-receiver constraints on the design. (Having no constraints is equivalent to a uniform weighting of modal power.) A vertical shear source at the surface is commonly assumed in calculating mode separation filters for the analog models now being studied. A better weighting of the power in f-k space is expected by introducing this simple source spectrum.

While an accurate and precise model of the earth's mean crust is implicitly assumed in implementing the mode theory in the above two ways, the third application of the theory is an inverse operation. The validity of a model hypothesized to possess the correct average properties of the earth's crust is tested by requiring the theoretical dispersion curves to agree with experimental dispersion curves within specified limits. A good match indicates proper layer velocities, thicknesses and densities. An explicit knowledge of the dependency of the accuracy of the calculations upon the uniquen s of the assumed crustal configuration is needed in this last application. Note that a correspondence between theoretical and experimental seismograms is not required; only the dispersion curves need coincide.

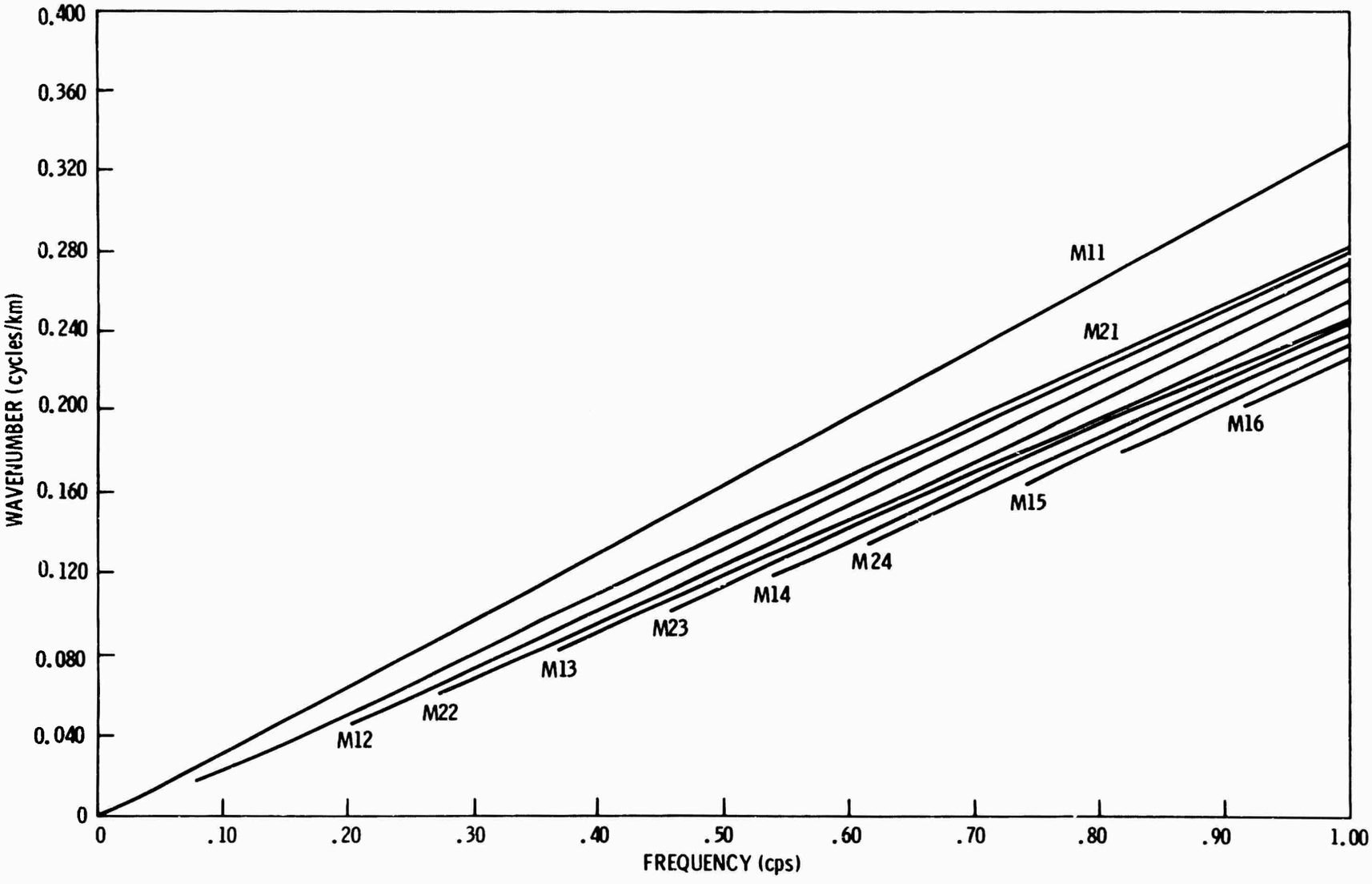

Figure II-1. Frequency-Wavenumber Representation of the TFO Normal Modes M_{11} through M_{16}

B. TFO CRUSTAL MODEL

1. Geophysics of Tonto Forest Seismological Observatory (TFO)

The TFO extended array of seismographs consists of eight mobile long-range seismic monitoring (LRSM) vans and TFO. The topography and geology of the station sites vary significantly because the extended array straddles the Colorado Plateau boundary in an X shape, with a NW-SE leg approximately 325 km long and a SW-NE leg approximately 287 km long (Figure II-2). This fact suggests that it will prove difficult to represent the entire area covered by the extended array with a single plane-layered model.

The TFO site itself is considered to be in the Basin and Range province since it is roughly 12 mi south of the Mogollon Rim, the southern boundary of the Colorado Plateau. (Significant scattering of seismic waves could occur in the vicinity of the Mogollon Rim.) The Diamond Rim fault, about 10 mi south of the Mogollon Rim, is the major structural feature in the area. The sedimentary cover at TFO is heterogeneous. Furthermore, a complete interpretation of the deep crust between the Diamond Rim fault to the north and Star Valley to the south is still being sought. It has been surmised by Harley et al[4] that there is a transition in crustal structure in the immediate vicinity of TFO.

The crustal model finally constructed for calculations pertaining to the TFO extended array was the one most appropriate for the TFO site. The model's physical parameters are given in Table II-1.

Except for layer 2, the model compressional velocities and layer thicknesses are the best estimates available from Harley[4] and Linville and Laster.[5]

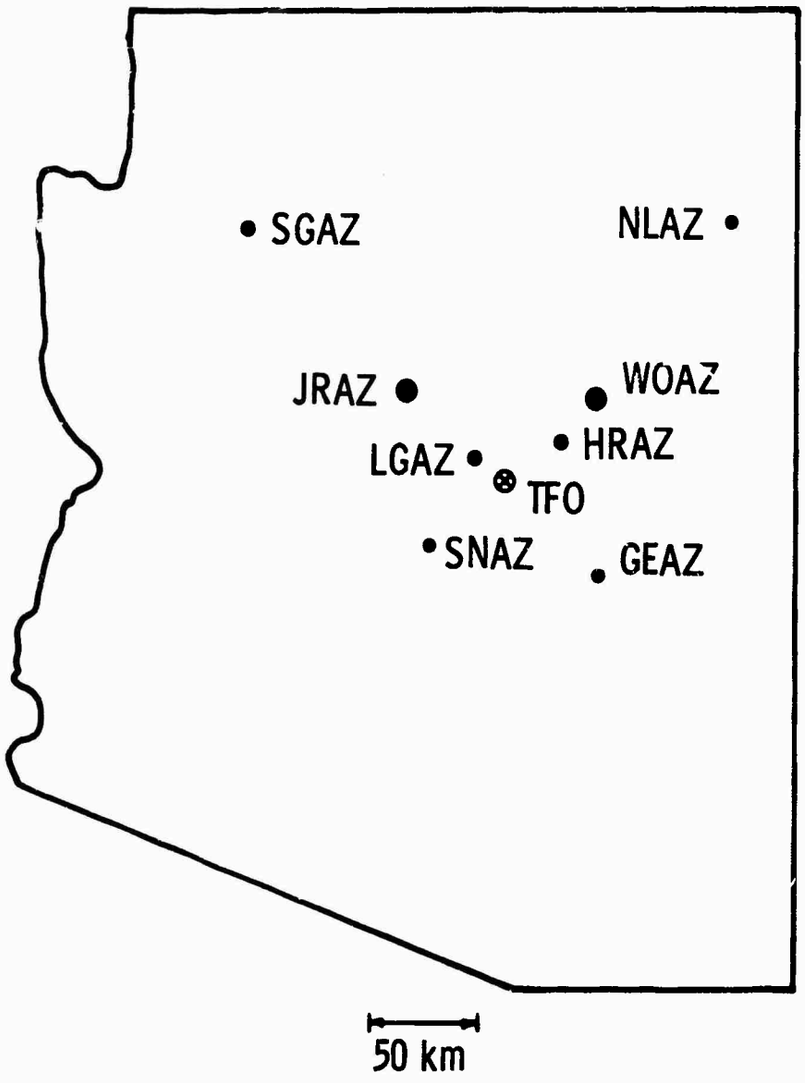

Figure II-2. Configuration of the TFO Extended Array

Table II-1

PHYSICAL PARAMETERS FOR TFO CRUSTAL MODEL

Layer	Compressional Velocity, α (km/sec)	Shear Velocity, β (km/sec)	Layer Thickness (km)
1	4.8	2.77	0.5
2	5.9	3.41	4.0
3	6.1	3.52	16.0
4	7.0	4.04	16.0
Half-space	7.9	4.56	∞

In the paper by Linville and Laster, a theoretical 2-layer crustal dispersion curve was fitted to an experimental curve obtained from high frequency recordings of a series of calibration shots by the USGS. The result was a determination of the compression velocity and layer thickness for the surface layer in the vicinity of TFO (layer 1 in Table II-1).

In the paper by Harley, two nuclear explosions and a series of USGS calibration shots yielded multiple determinations of P_n, P_g and P* arrival times. From these data and the results of an earlier study of the crust near TFO, the four remaining compressional velocities of Table II-1 were derived.

The shear velocities of this model were obtained under the assumption that the elastic parameters, λ and μ, are roughly equal. This approximation has been found to be legitimate for most rocks, and the resulting equation for the shear velocities, $\beta = \alpha/\sqrt{3}$, is referred to as Poisson's relation.

An estimate of the importance of significant lateral variations in the physical parameters of Table II-1 is possible. A significant lateral variation is a horizontal change in geologic structure of the order of magnitude of the model layer structure occurring within a distance less than that characteristic of the TFO extended array dimensions. When such a geologic discontinuity occurs, mode theory predictions based on plane layers can deviate appreciably from the results based on field measurements. Therefore, provided any laterial discontinuities present possess a distance scale in excess of about 200 km, the crustal model of Table II-1 can serve as a valid interpretative tool for local dispersion studies at source-receiver separations ranging from 300 to 1200 km in the region around TFO.

2. Mode Calculations for TFO Crust

The largest and smallest modal group velocities of concern in the TFO model are 7.9 and 2.77 km/sec, respectively. It follows that the largest time separation of the various modes studies occurs between the leaky modes traveling at 7.9 km/sec and the normal modes traveling at 2.77 km/sec. The time interval between the slowest and fastest modes is proportional to the source-receiver separation; for distances up to 1200 km it will not exceed 420 sec. For a sample rate of 0.5 sec, implying a folding frequency of 1.0 cps, (2N+1) = 841 time sample points are required. (This count takes the first point at t = 0.0 sec.) The frequency resolution of the resulting 420-sec gate is given by

$$\Delta f = \frac{1}{(2N+1)\Delta t} = \frac{1}{420.5} = 0.0023781212 \text{ cps}$$

and the number of independent frequency-domain sample points is 421.

Computations were carried out in the frequency domain with the Δf previously determined. Eleven normal modes and six leaky modes were found between 0.0 and 1.0 cps for the crustal model of Table II-1.

The phase-velocity dispersion curves for both leaky and normal modes are shown in Figure II-3. There is a noticable distention in the M_{13}, M_{23} and M_{14} curves at about 4.04 km/sec, the shear velocity of the fourth layer. The lower shear modes converge toward the shear velocity of the third layer (3.52 km/sec) as they approach 1.0 cps. The first three leaky modes very nearly couple onto the M_{22}, M_{13} and M_{23} normal modes at their respective cutoff frequencies, although the alignment is incomplete because the leaky mode calculations did not extend to normal mode cutoff.

Figure II-4 shows normal mode group velocity vs frequency at TFO. There is a group velocity maxima for each mode beginning with M_{12}. Furthermore, the higher the order of the mode, the higher the group velocity maxima. A straight line through the maxima falls at about 3.9 km/sec at 1.0 cps. If this trend continues at high frequencies, the group velocity will equal the phase velocity within an intermediate layer of the model. This type of structure in the dispersion curves has been noted for 2-layer model studied in an earlier report.[2]

Normal mode excitation is displayed in Figures II-5 through II-9. The M_{11} amplitude is an order of magnitude greater than the amplitude of any other mode. As usual, the vertical amplitude exceeds the horizontal amplitude for any one mode, and the modal amplitudes decrease with increasing mode number. Compared to the adjacent modes, the M_{24} excitation appears to be more constant in the 0.80 to 0.91 cps frequency band.

The first and second Love mode dispersion curves for the TFO model are given in Figure II-10. The second order Love mode dispersion is very similar to the M_{21} shear mode dispersion. This result is due to chance, as far as is known at present.

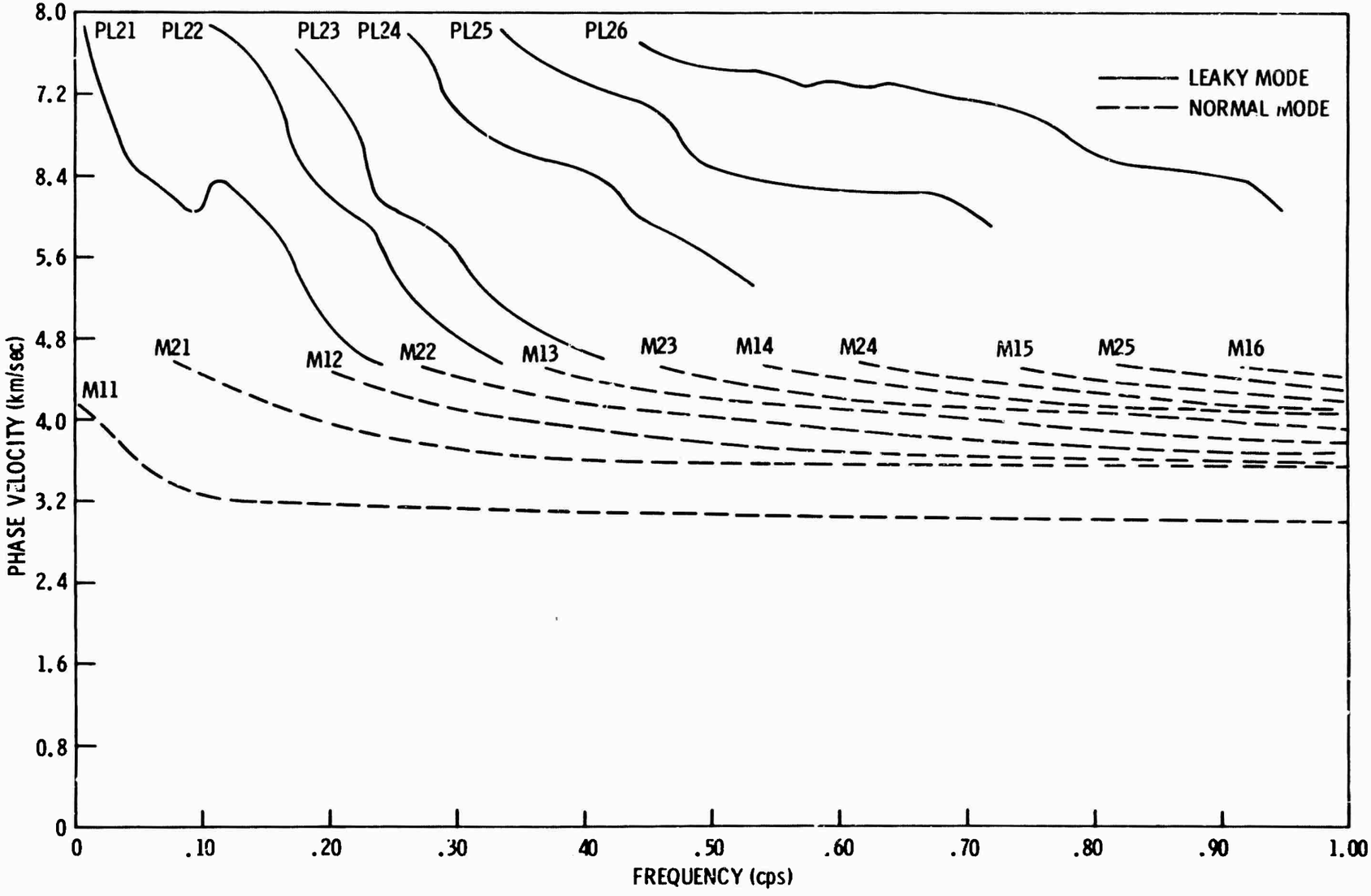

Figure II-3. Leaky (PL) Mode and Normal Mode Phase Velocity vs Frequency at TFO

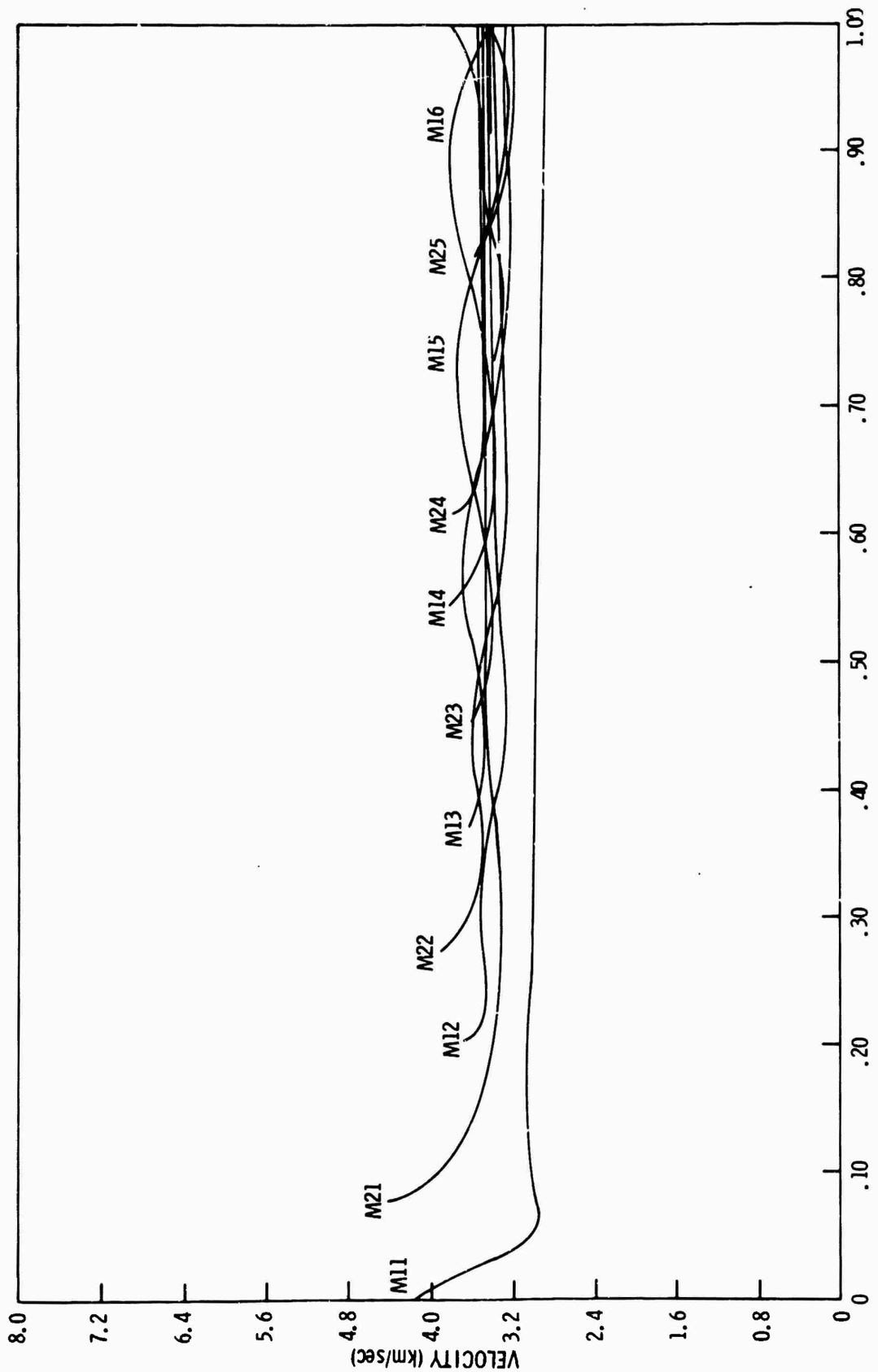

Figure II-4. Normal Mode Group Velocity vs Frequency for M_{11} through M_{16} at TFO

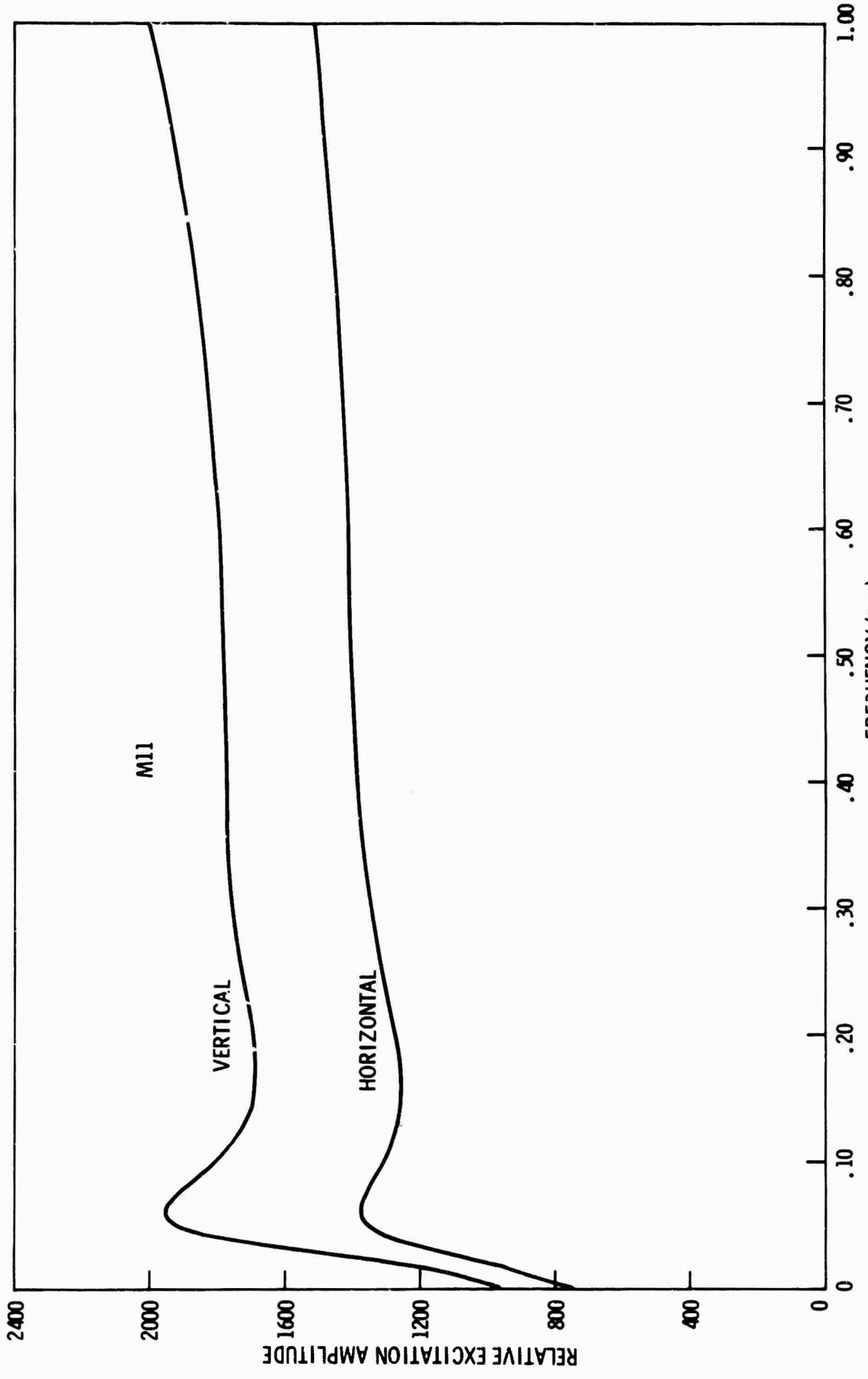

Figure II-5. Horizontal and Vertical Excitation Functions for Normal Mode M_{11} at TFO

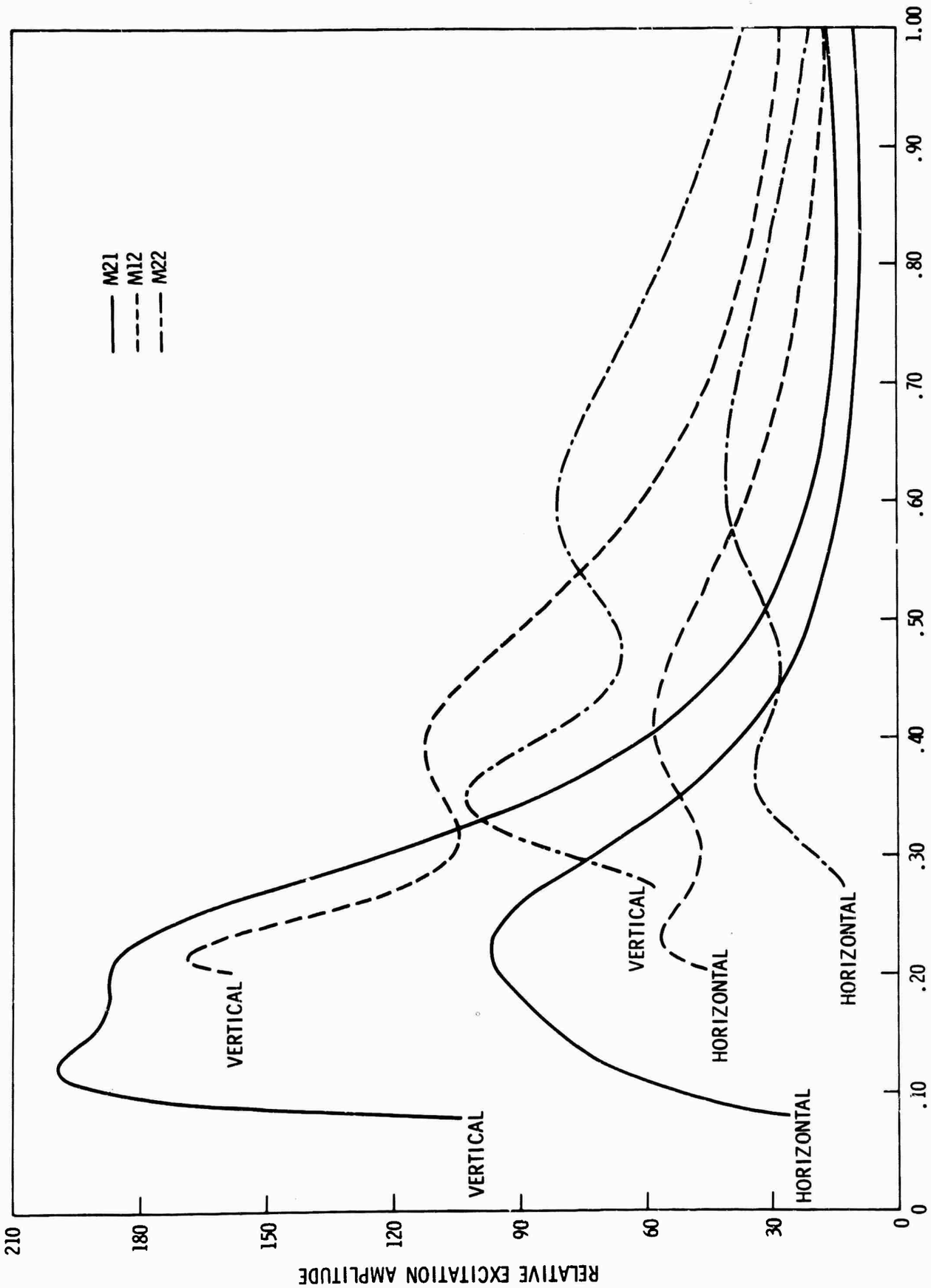

Figure II-6. Horizontal and Vertical Excitation Functions for Normal Modes M_{12}, M_{21} and M_{22} at TFO

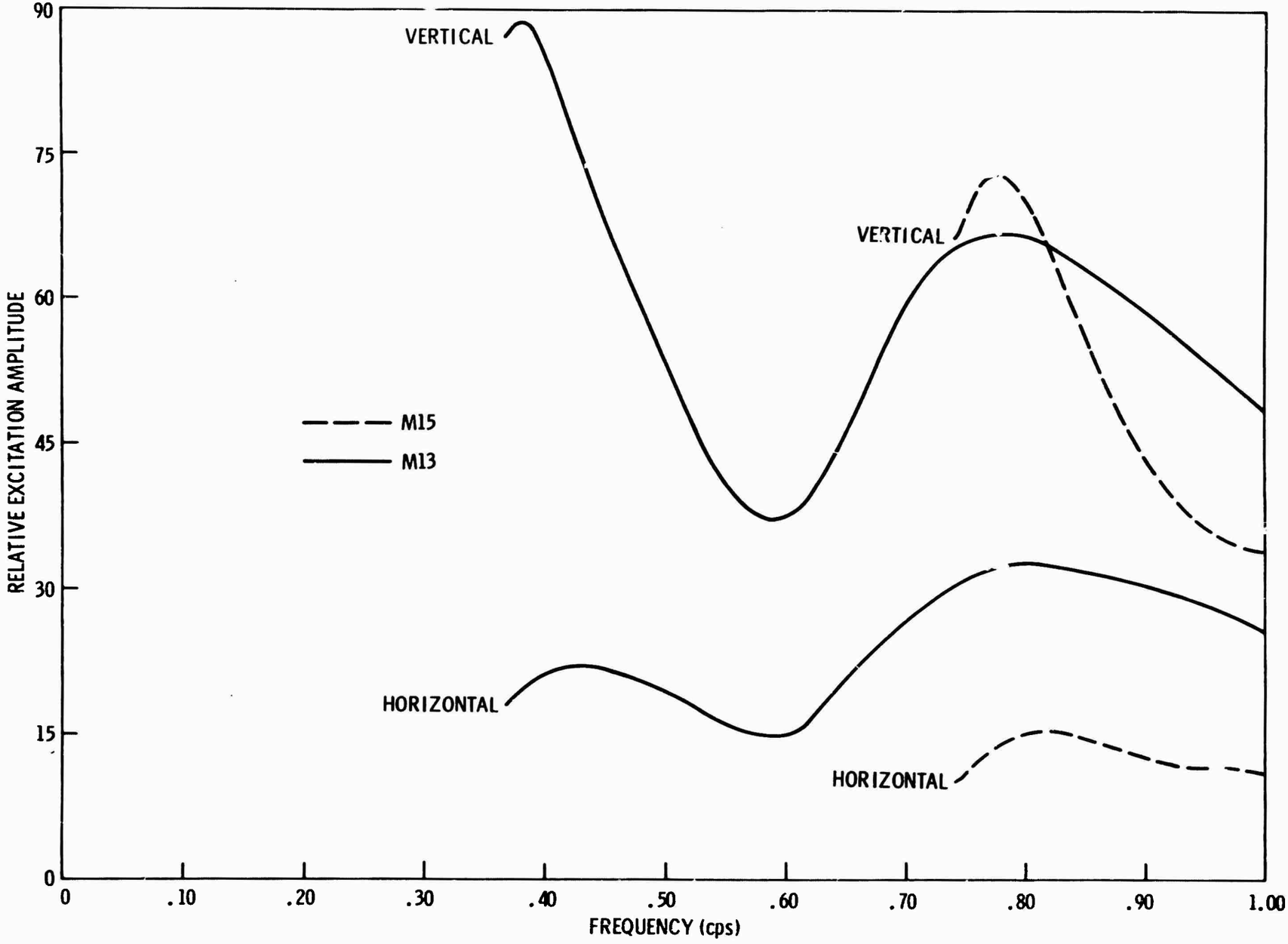

Figure II-7. Horizontal and Vertical Excitation Functions for Normal Modes M_{13} and M_{15} at TFO

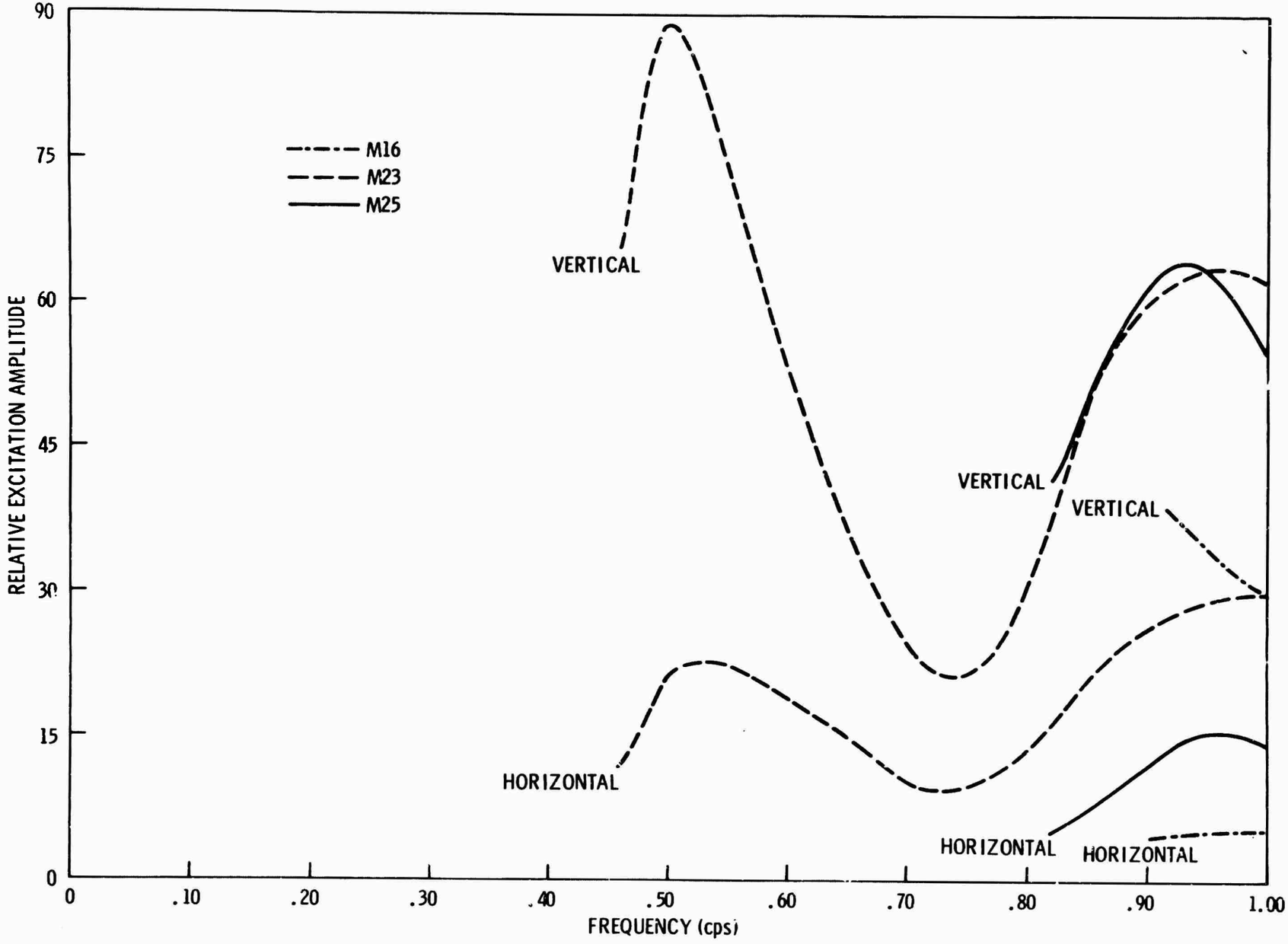

Figure II-8. Horizontal and Vertical Excitation Functions for Normal Modes M_{23}, M_{25} and M_{16} at TFO

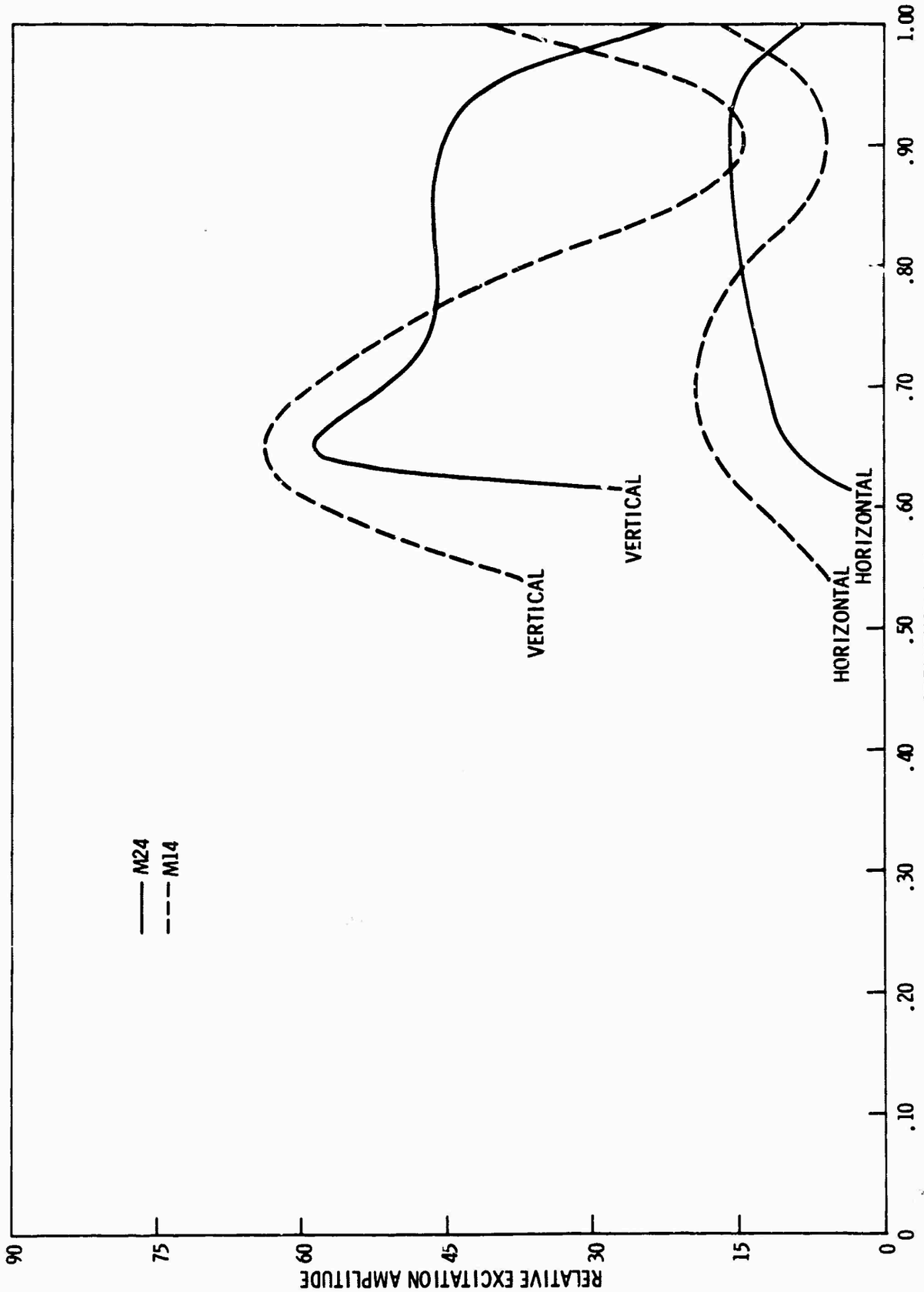

Figure II-9. Horizontal and Vertical Excitation Functions for Normal Modes M_{14} and M_{24} at TFO

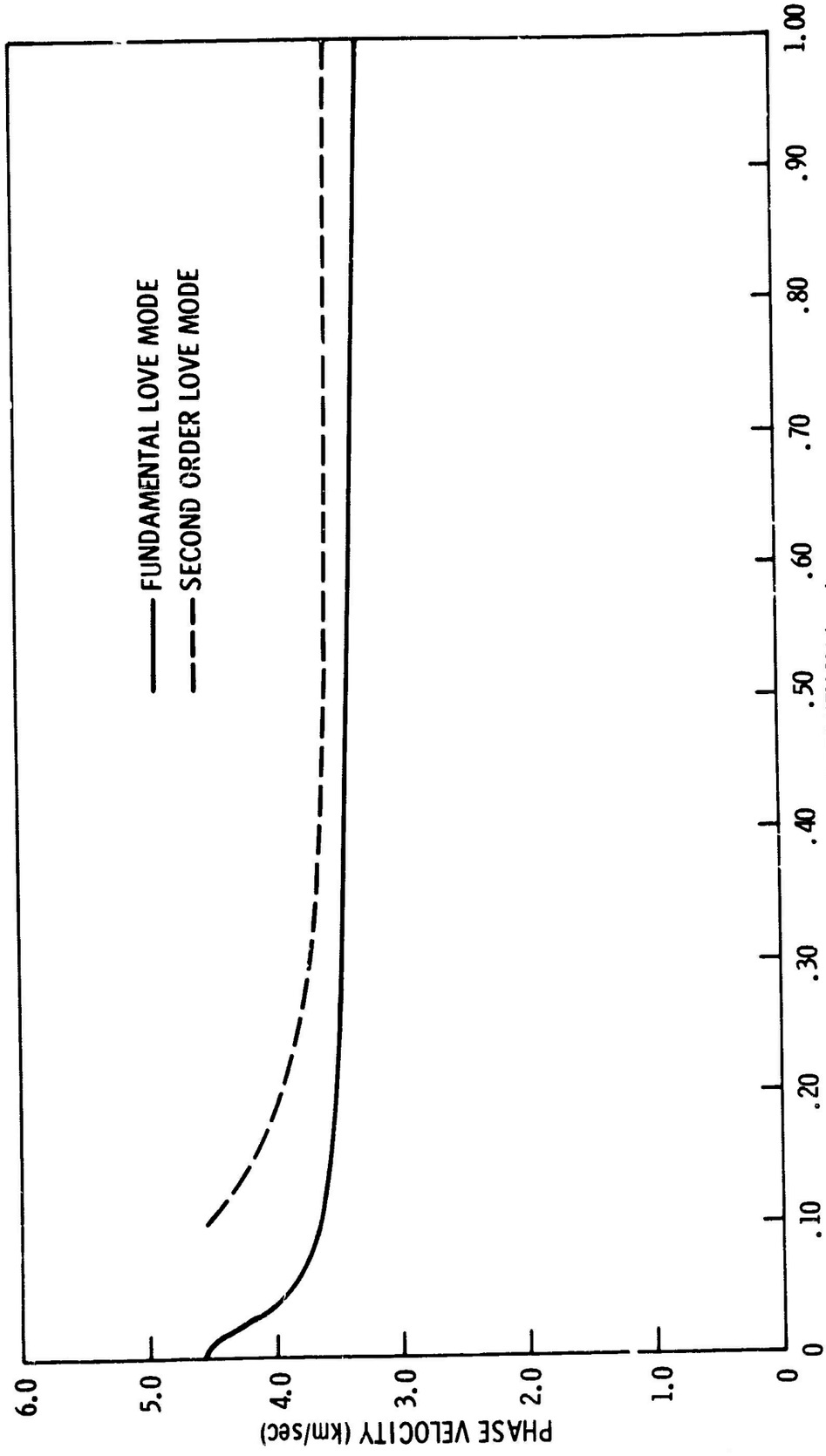

Figure II-10. Phase Velocity vs Frequency for Fundamental and Next Higher Love Mode at TFO

It is often useful to have a graph giving the wavelength of each mode at a given phase velocity for comparison with the physical dimensions of the geological structure or the detector array. Such a graph is given in Figure II-11 of this report. It includes all 11 normal modes and the fundamental Love mode.

Figures II-12 through II-14 give the leaky mode excitation at TFO. Figures II-15 through II-17 are plots of the accompanying attenuation in db/sec. The attenuation/unit time is calculated from the attenuation/unit distance ($= \gamma$) by multiplying the latter by the group velocity. The PL modal amplitudes decay exponentially in space according to $e^{-\gamma x}$. Even though the leaky mode excitation amplitudes typically increase with increasing attenuation, the net effect is one of rapid decay with distance. Each leaky mode excitation graph exhibits at least three distinct amplitude maxima which do not increase or decrease according to frequency. Although the time attenuation curves, together with the excitation curves, indicate that the largest part of the modal power is concentrated in a band of frequencies near cutoff frequency, there appear to be important peaks in modal power for frequencies other than cutoff. Figures II-18 through II-20 display leaky mode group and phase velocity vs frequency. Again the behavior of the dispersion curves in the vicinity of intermediate layer velocities is similar to that noted for the 2-layer model studies in the Basic Research in Crustal Studies.[2] The presence of the third and fourth layers in the TFO model is most evident at high frequencies in the high order modes.

3. Review of Available Data

Field recordings have been obtained from the TFO extended array. This array qualifies as having an aperature large enough to separate lower order, low frequency crustal modes by applying multichannel filtering techniques.

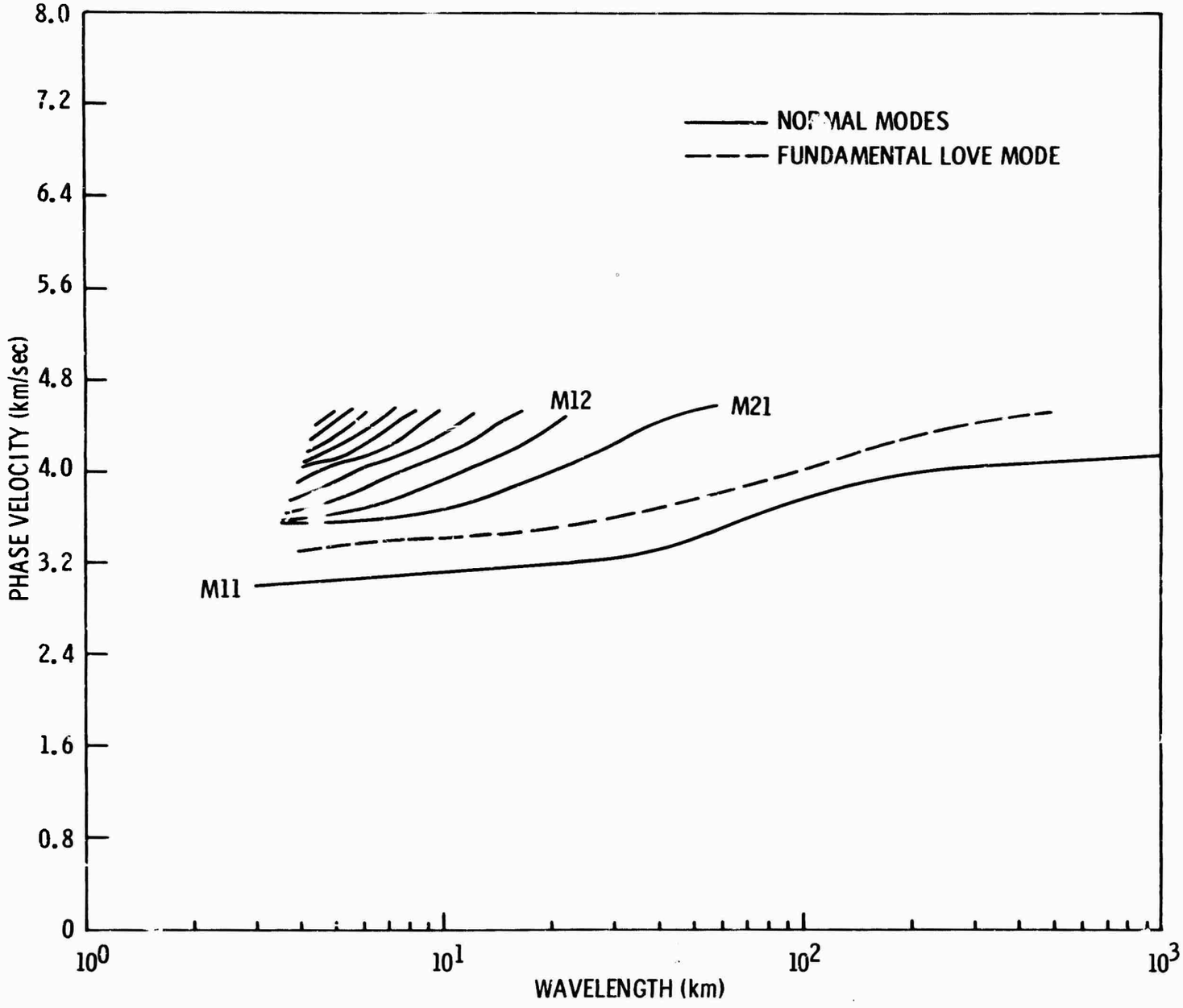

Figure II-11. Phase Velocity vs Wavelength for All Normal Modes and the Fundamental Love Mode at TFO

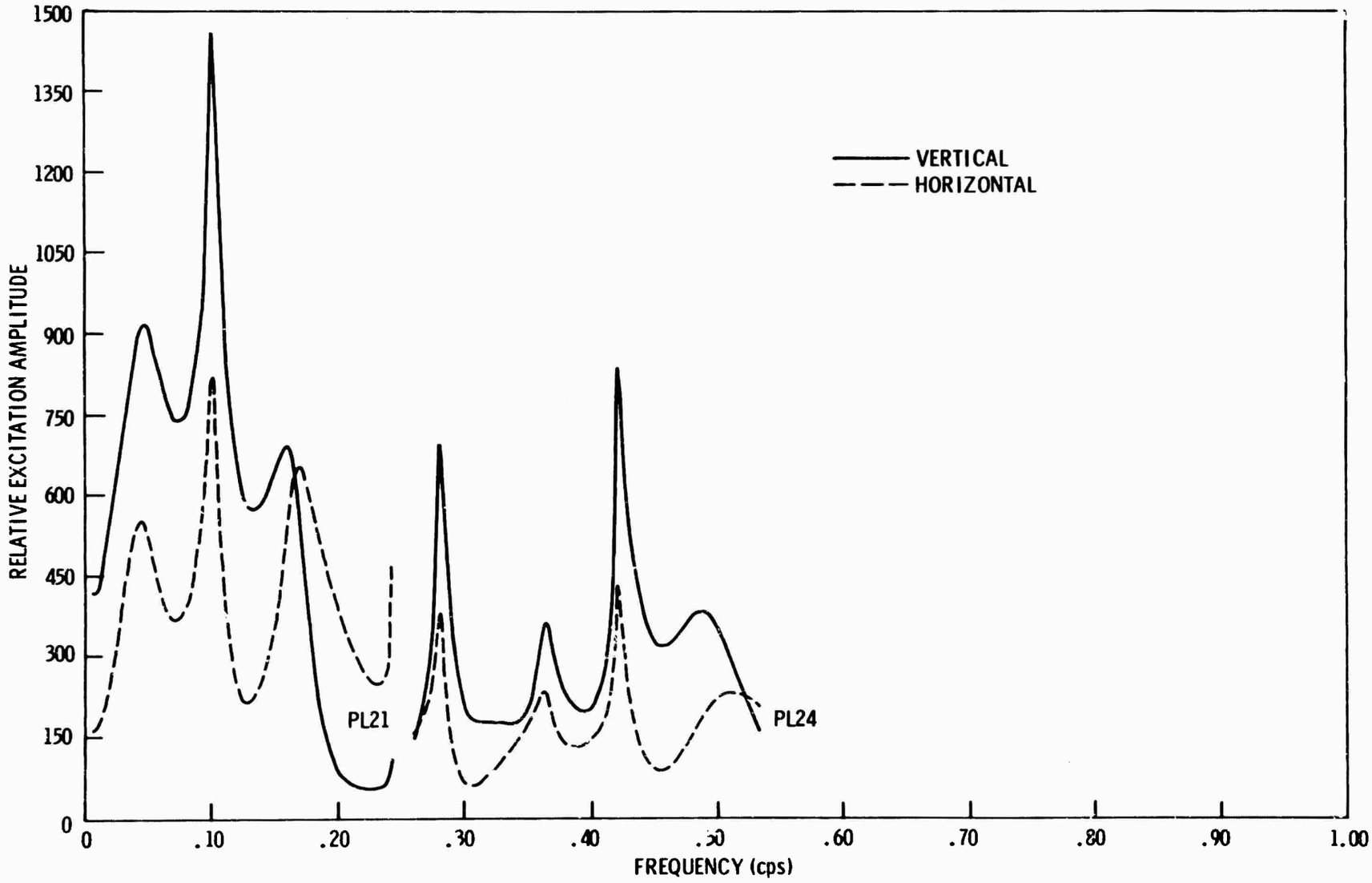

Figure II-12. Horizontal and Vertical Excitation Functions for Leaky Modes PL_{21} and PL_{24} at TFO

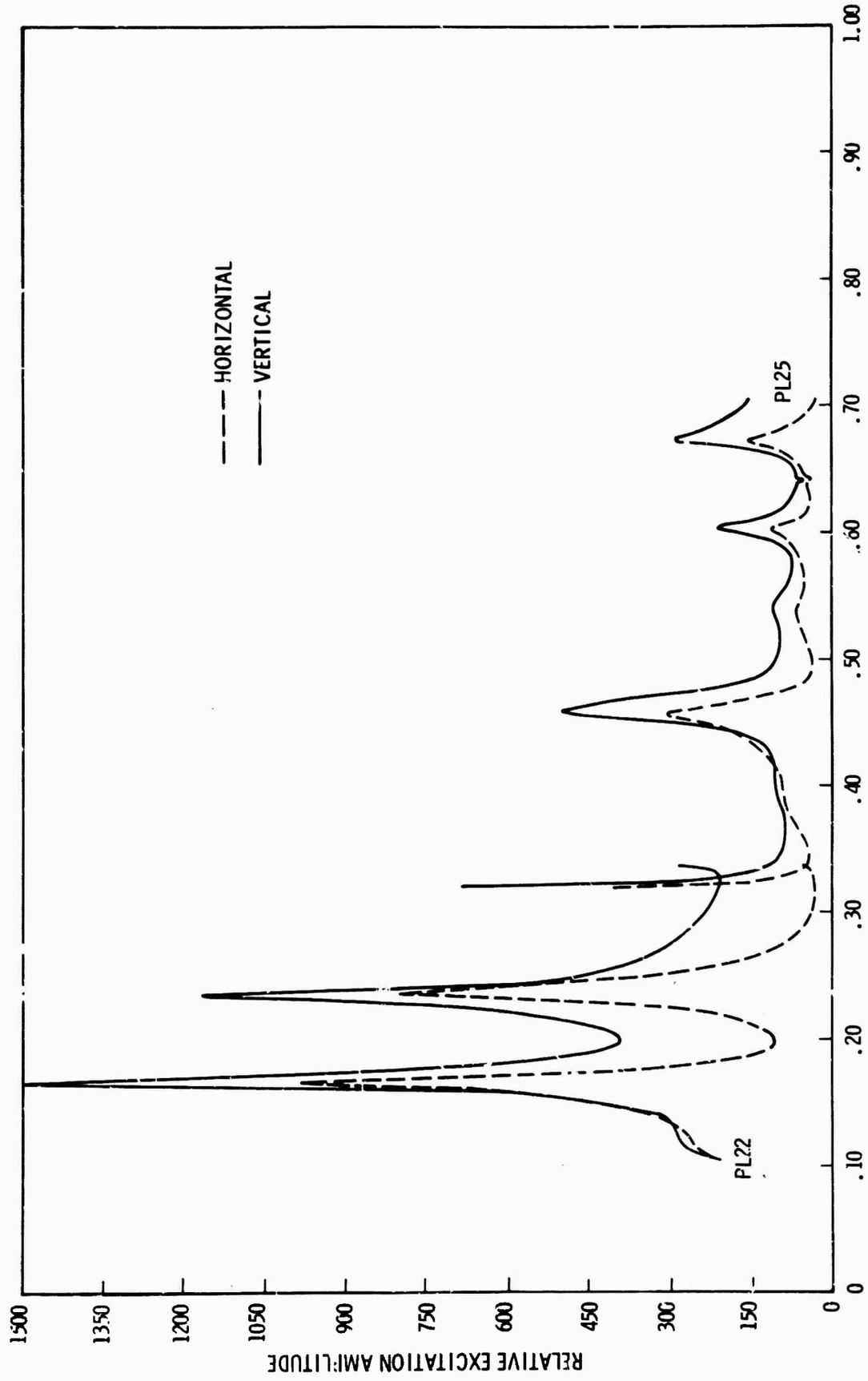

Figure II-13. Horizontal and Vertical Excitation Functions for Leaky Modes PL_{22} and PL_{25} at TFO

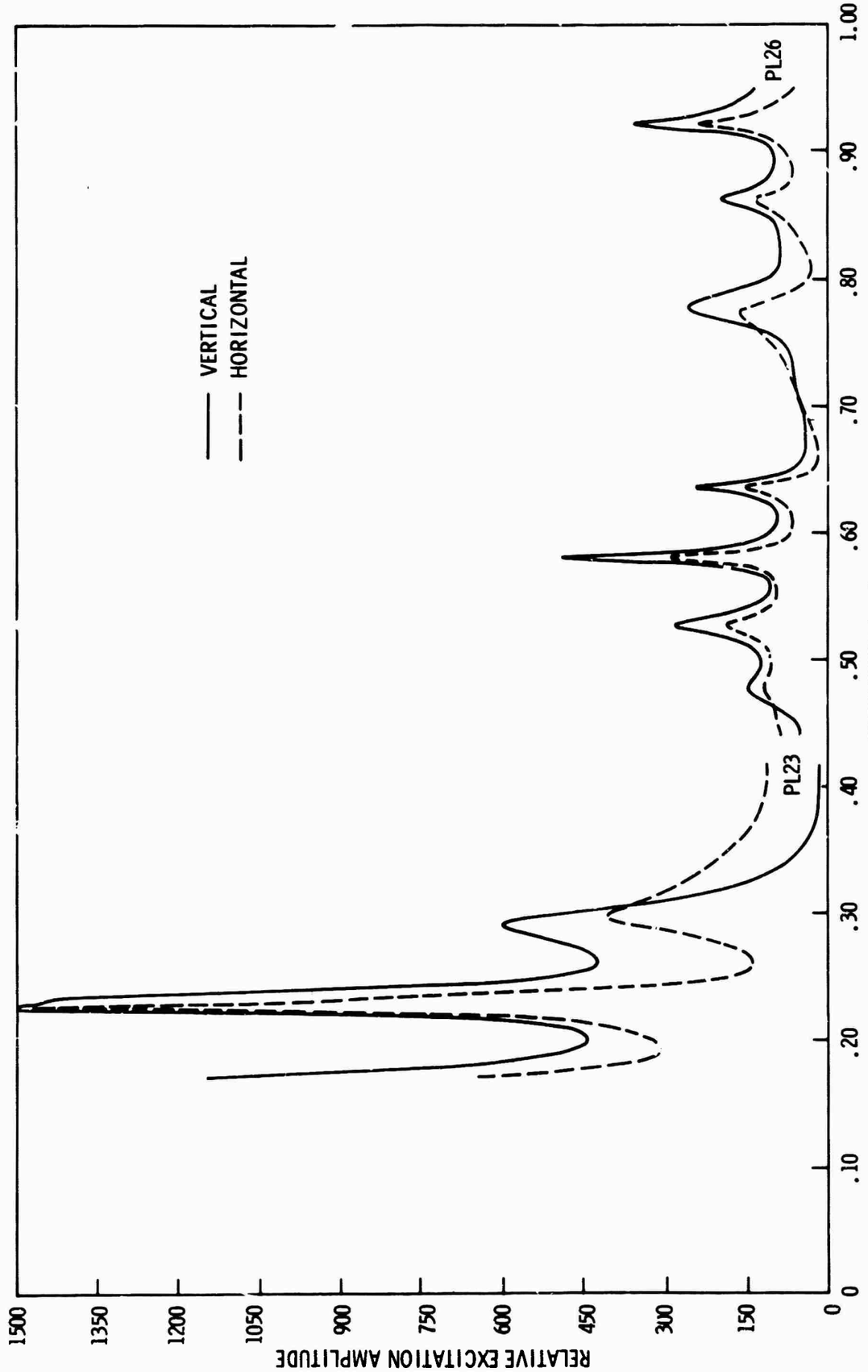

Figure II-14. Horizontal and Vertical Excitation Functions for Leaky Modes PL_{23} and PL_{26} at TFO

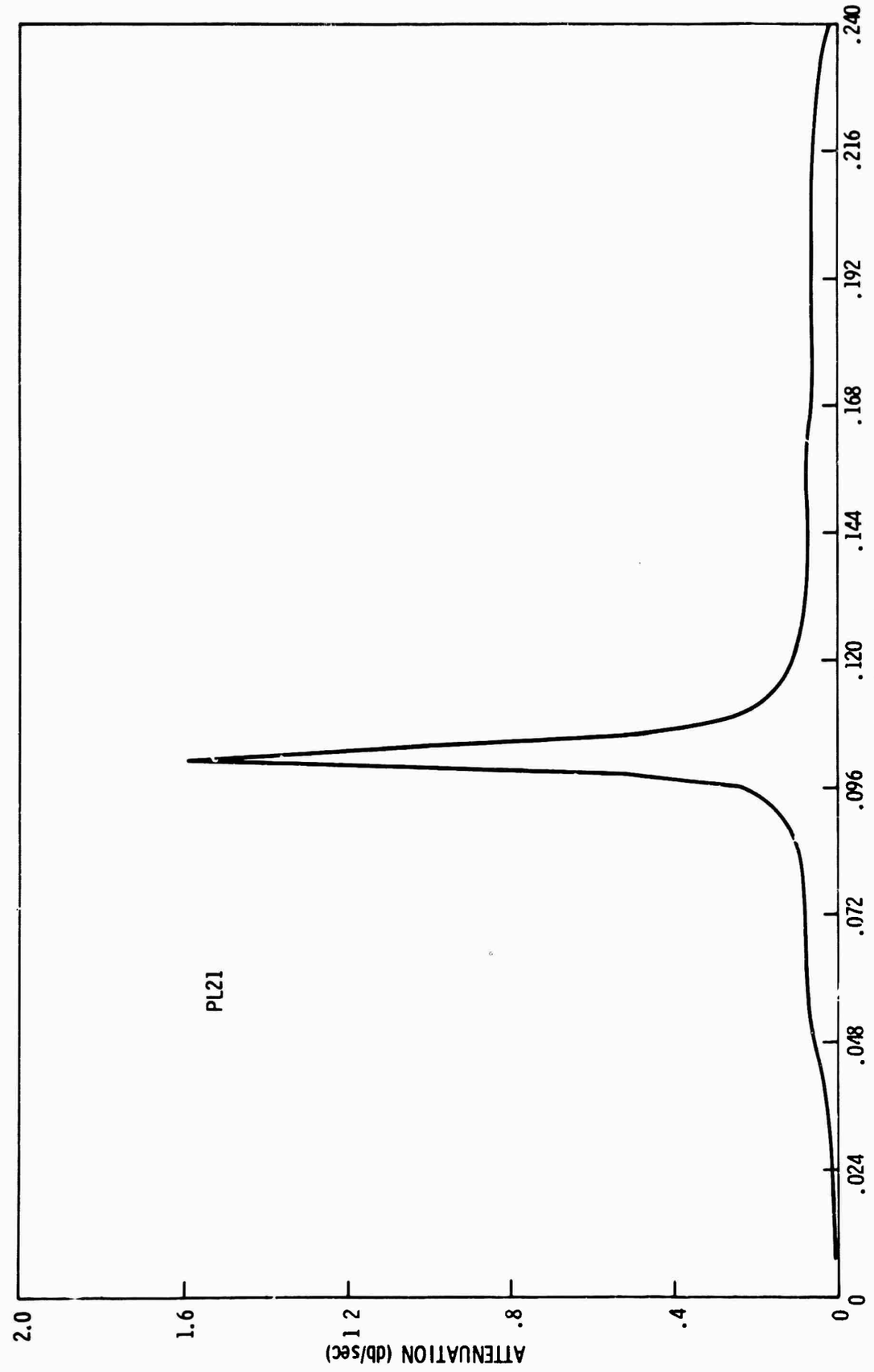

Figure II-15. Time Attenuation Rate for Leaky Mode PL_{21} as a Function of Frequency At TFO

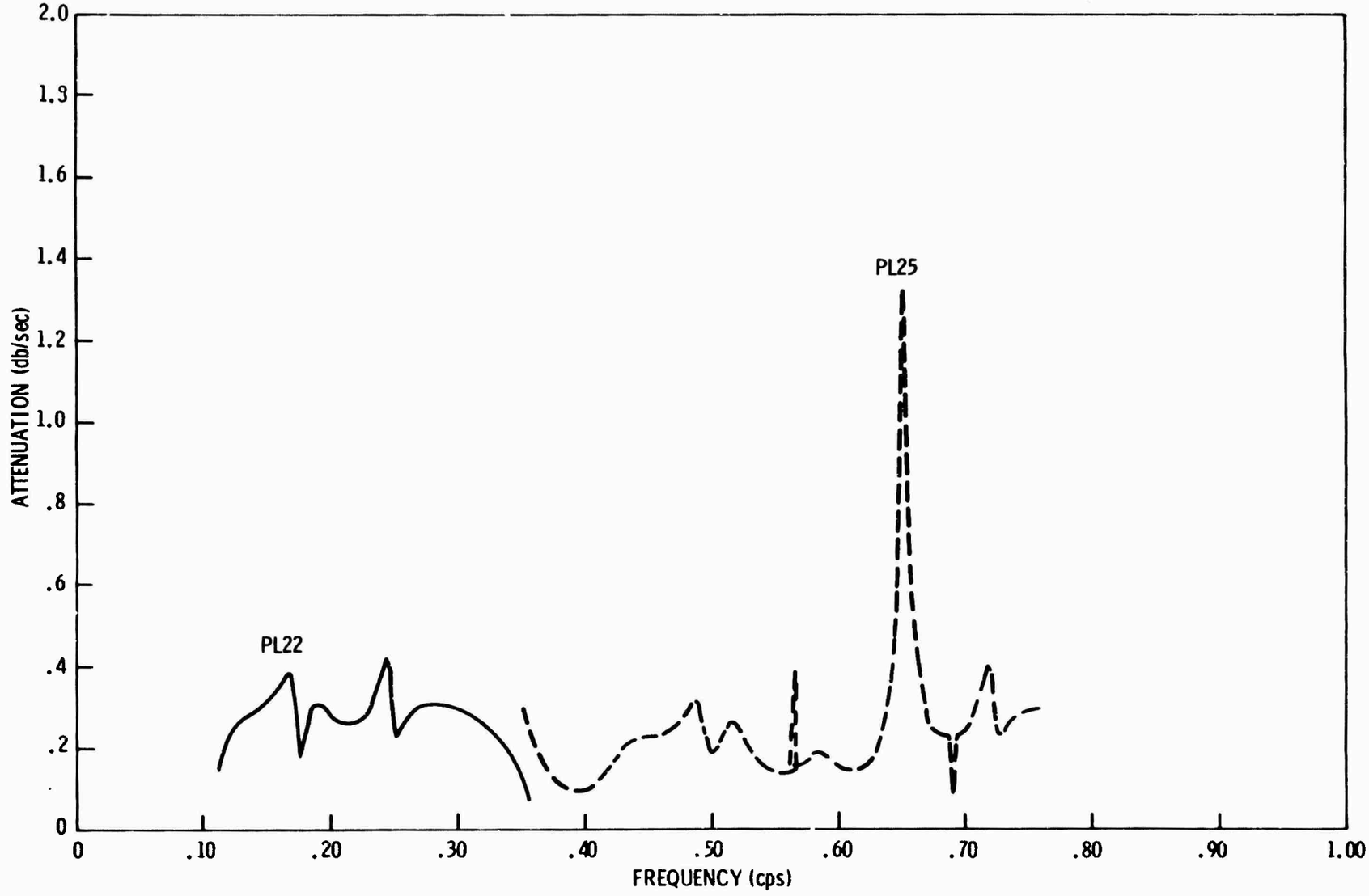

Figure II-16. Time Attenuation Rate for Leaky Modes PL_{22} and PL_{25} as a Function of Frequency at TFO

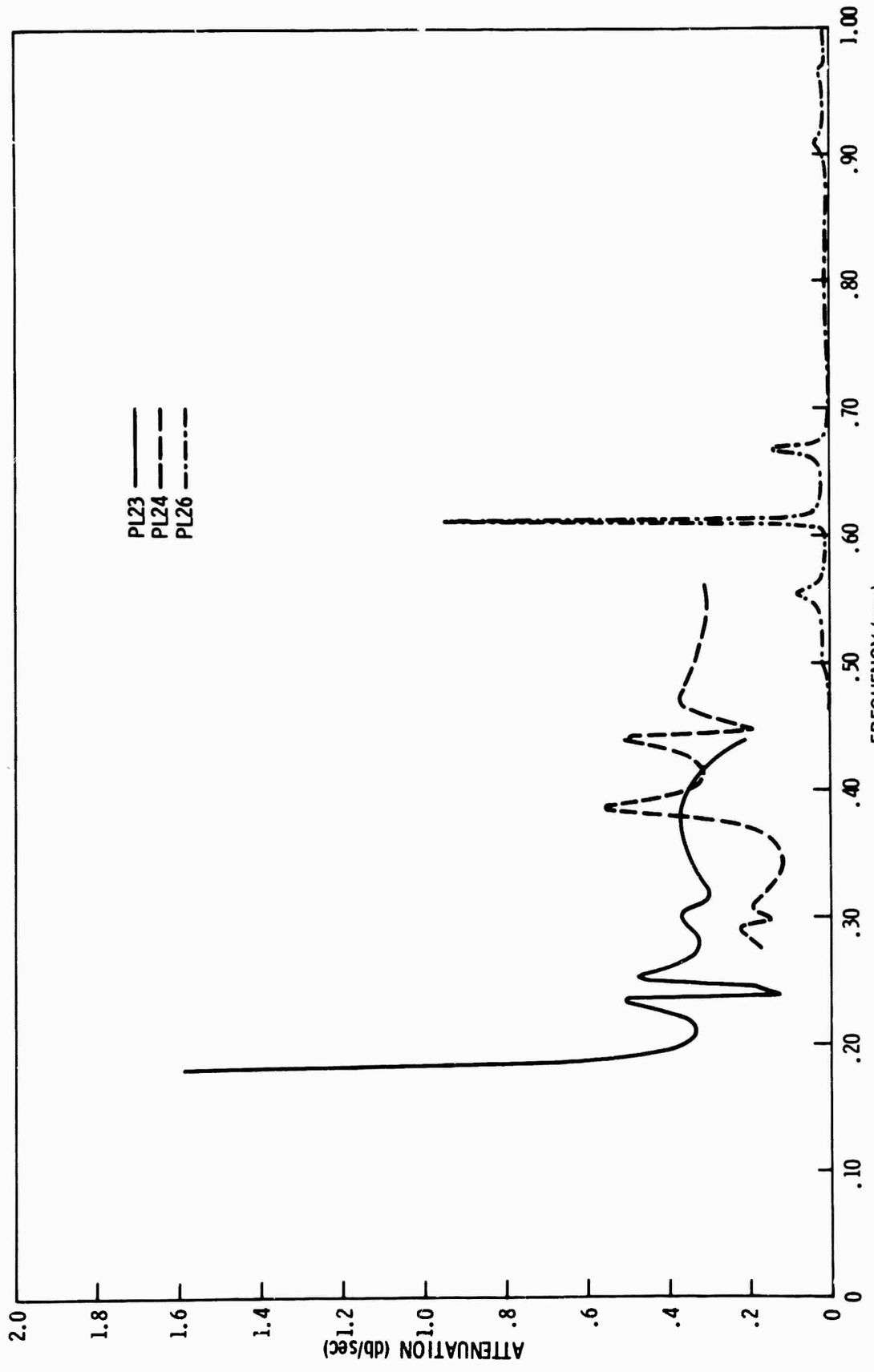

Figure II-17. Time Attenuation Rate for Leaky Modes PL_{23}, PL_{24} and PL_{26} as a Function of Frequency at TFO

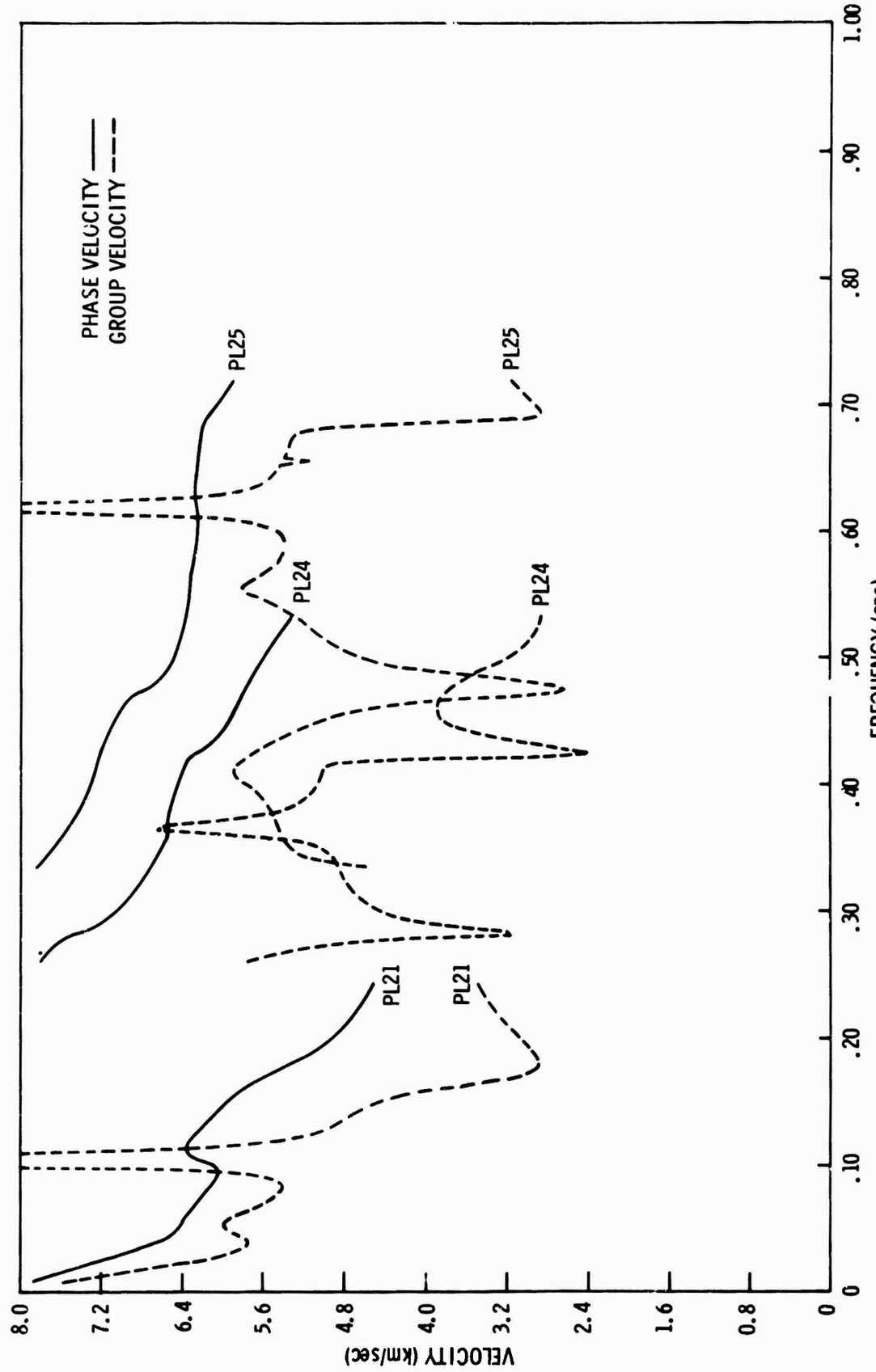

Figure II-18. Leaky Mode Phase and Group Velocity vs Frequency for PL_{21}, PL_{24} and PL_{25} at TFO

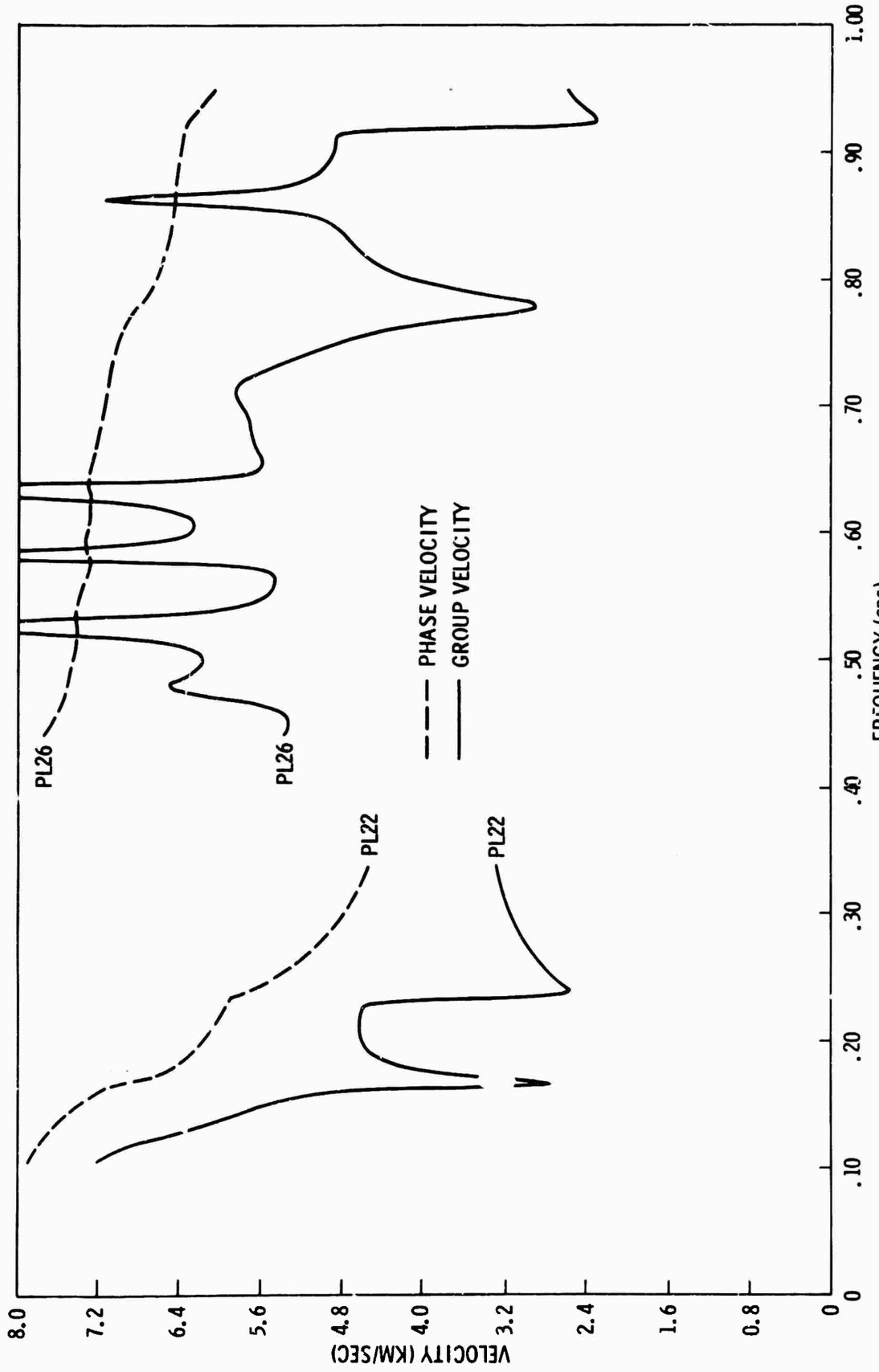

Figure II-19. Leaky Mode Phase and Group Velocity vs Frequency for PL_{22} and PL_{26} at TFO

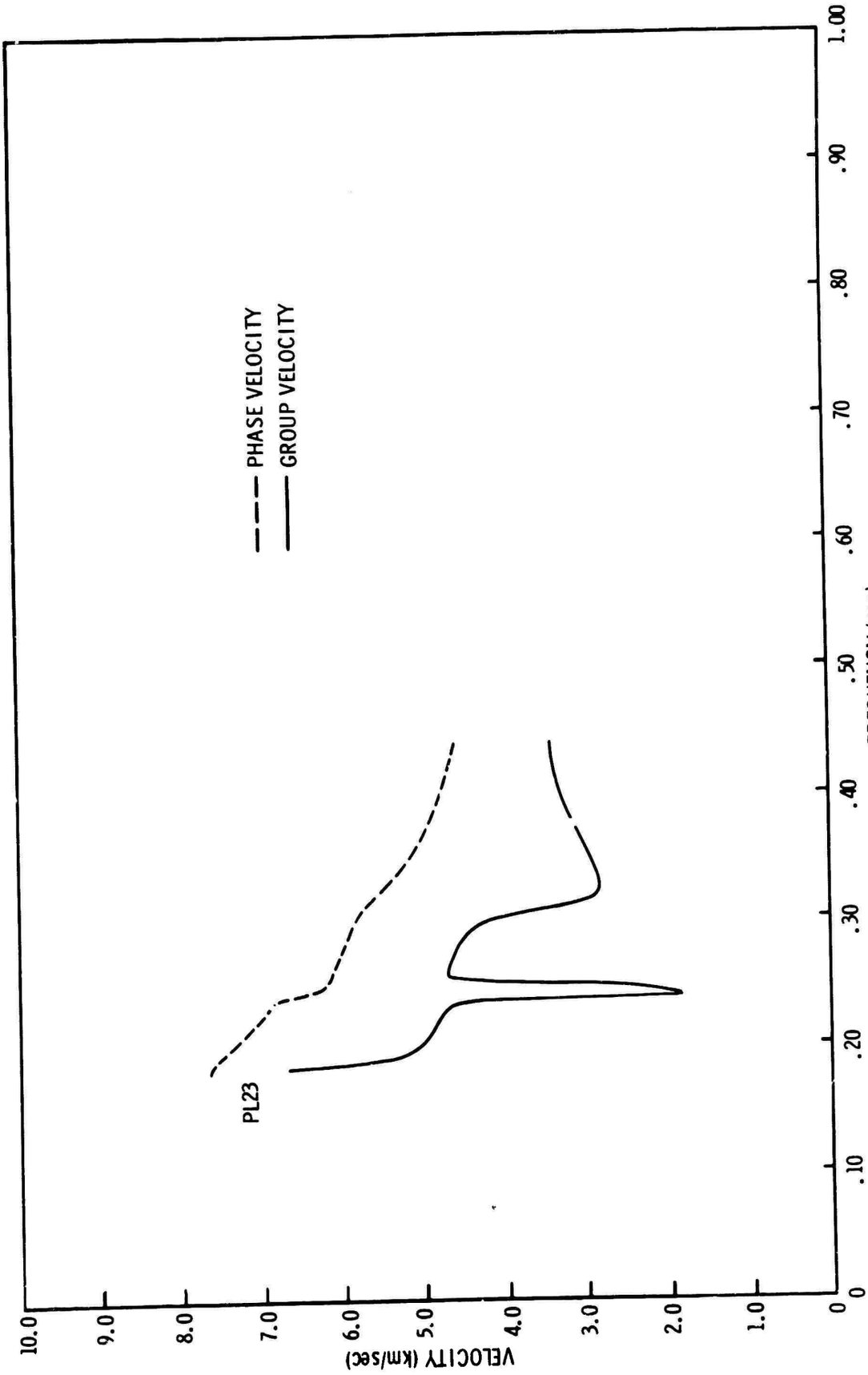

Figure II-20. Leaky Mode Phase and Group Velocity vs Frequency for PL_{23} at TFO

Figure II-2 shows the station locations of the TFO extended array, and Table II-2 gives station name, elevation, rock-type, and coordinates for the nine array locations.

Table II-2

TFO EXTENDED ARRAY

Station Name	Code Name	Elevation (ft)	Rock Type	Latitude (N)	Longitude (W)
Seligman	SG	5500	Limestone	35°38'27"	113°15'39"
Jerome	JR	4300	Alluvium	34°49'32"	111°59'25"
Long Valley	LG	5800	Tuff	34°24'28"	111°32'45"
TFO	TFO	4890	Granite	34°16'04"	111°16'13"
Globe	GE	4840	Slate	33°46'32"	110°31'41"
Nazilini	NL	6300	Siltstone	35°48'25"	109°37'43"
Winslow	WO	5200	Sandstone	34°52'35"	110°37'15"
Heber	HR	6150	Limestone	34°40'11"	110°45'59"
Sunflower	SN	2900	Wthrd. Granite	33°51'49"	111°41'34"

Three channels of data (vertical, radial and transverse) are recorded at each location by Sprengnether long-period seismometers. The block diagram of Figure II-21 shows data and recording systems for the long-period large aperture array at TFO. Recording was done on the Astrodata Digital Acquisition System at a 50-msec sample interval. The response of the recording system (Figure II-22) is seen to be highly peaked at 0.045 cps and the recordings are considered to be narrowband.

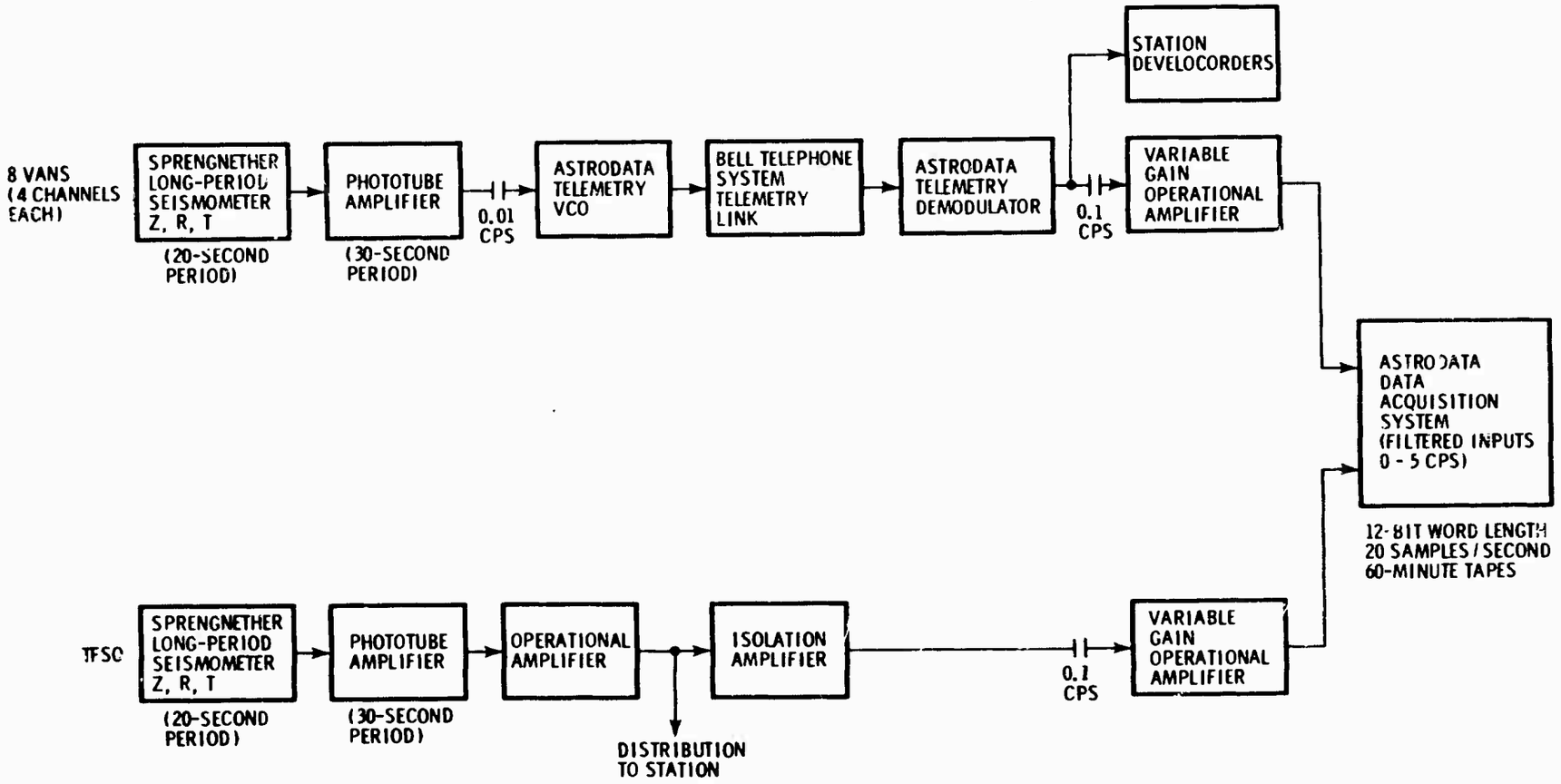

Figure II-21. Block Diagram of Data and Recording Systems for Long-Period Large Aperture Array at TFO

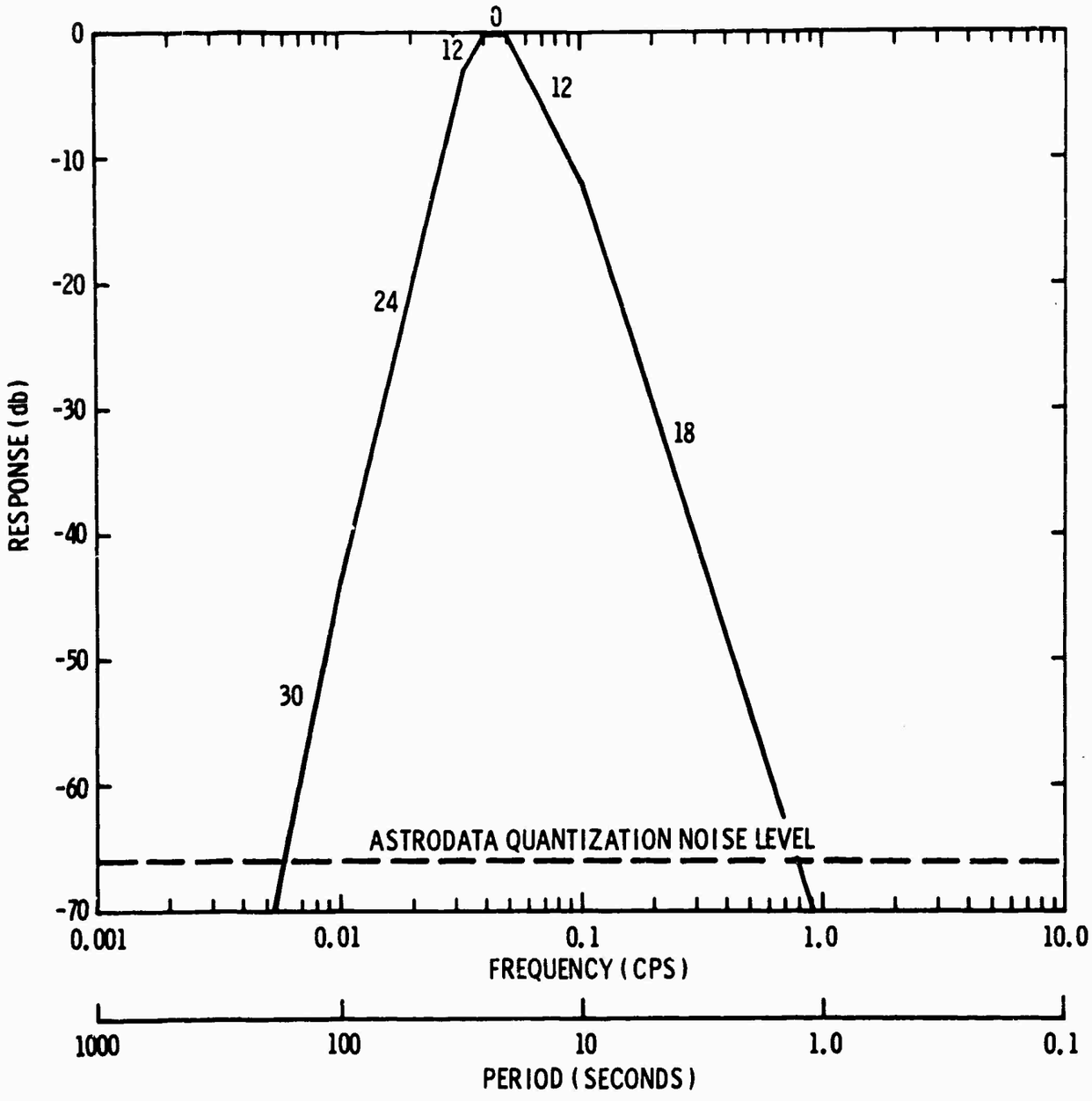

Figure II-22. Recording System Composite Response

The effect of the recording system response is to bandlimit the data. So, for a crust such as TFO, the modes of propagation that may be recorded on the se smograms are limited to continental PL mode (PL_{21}), fundamental Rayleigh (M_{11}), first higher-order normal mode (M_{21}), fundamental Love mode, and the first higher-order Love mode.

Recordings were antialias filtered, resampled to a 0.5-sec sample interval, gain-corrected from calibration analysis, and then reformatted at the Seismic Data Laboratory for input to the IBM system associated with TIAC.* The data processing operations preceding Texas Instruments analysis is shown in Figure II-23.

Ideally, mode separation techniques would best be applied to events with epicentral distances less than 1000 km. The only event available which has an epicentral distance less than 1000 km was an earthquake from Southern California. Table II-3 describes associated PDE (Preliminary Determination Epicenters) information for this earthquake.

Table II-3

ASSOCIATED PDE INFORMATION
FOR
SOUTHERN CALIFORNIA EVENT

Location	Southern California
Date	26 September 1965
Origin Time	07:00:00.9
Latitude	34.7° N
Longitude	116.5° W
Magnitude	4.6
Depth	16 km

*Texas Instruments Automatic Computer, Trademark of Texas Instruments Incorporated

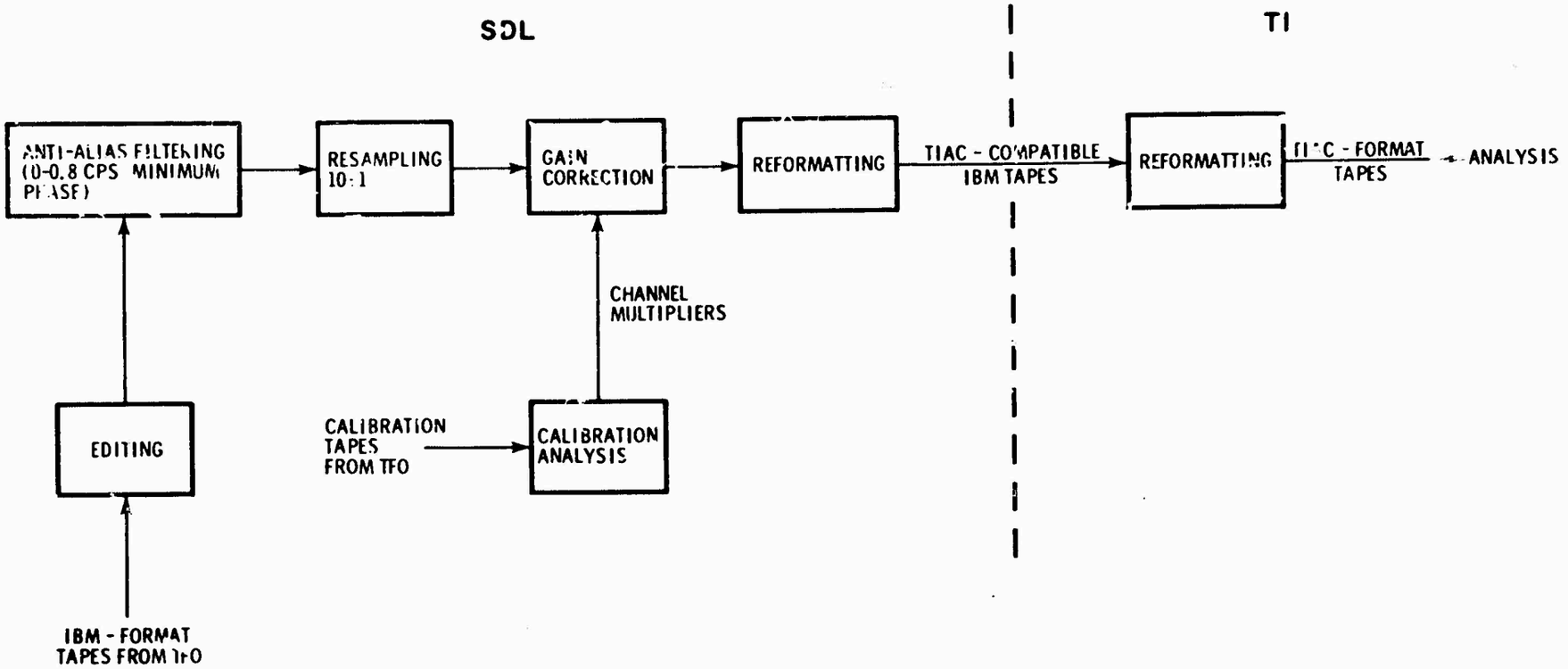

Figure II-23. Block Diagram of Data Processing Operations Preceding Texas Instruments Analysis

Figure II-24 shows seismograms of the event in variable area display. Table II-4 gives the channel identification, distance and azimuth for each recording station. Due to various malfunctions of the data systems, 11 out of 27 channels were not usable for this event. Only the 16 good channels are shown.

Table II-4

CHANNEL IDENTIFICATION, DISTANCE, AND AZIMUTH FOR SOUTHERN CALIFORNIA EVENT

Channel No.	Station Code	Component	Azimuth (Station to Epicenter)	Distance (km)
1	SG	Z	251.45°	312.75
2	JR	Z	269.35°	412.75
3	SN	Z	283.18°	451.85
4	TFO	Z	277.17°	482.34
5	WO	Z	269.53°	537.95
6	NL	Z	260.88°	636.66
7	JR	R	269.35°	412.75
8	SN	R	283.18°	451.85
9	TFO	R	277.17°	482.34
10	WO	R	269.53°	537.95
11	NL	R	260.88°	636.66
12	JR	T	269.35°	412.75
13	SN	T	283.18°	451.85
14	TFO	T	277.17	482.34
15	WO	T	269.53°	537.95
16	NL	T	260.88°	636.66

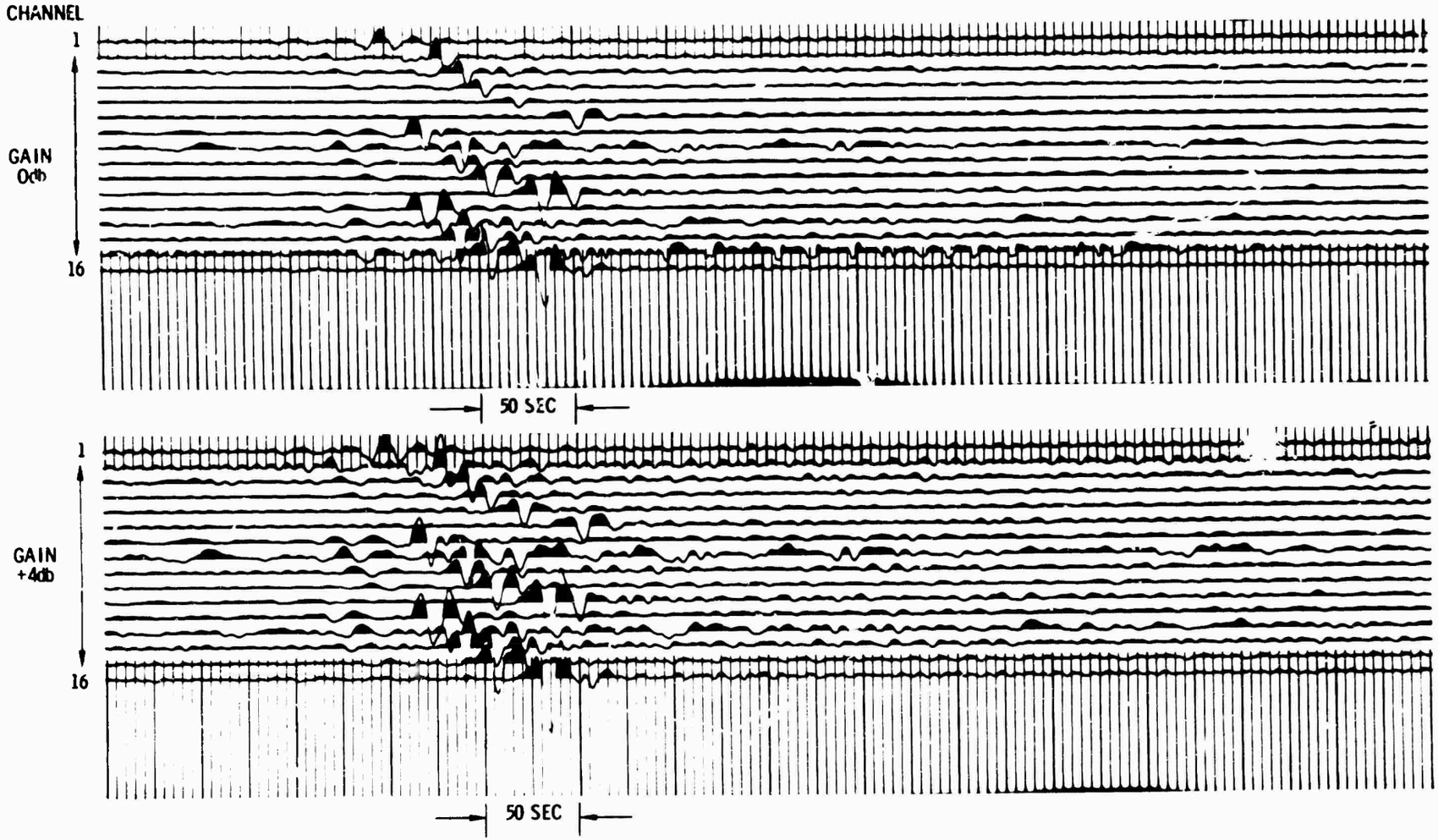

Figure II-24. Seismogram Recording of the Southern California Event (Channel Identification is Given in Table II-4)

Since independent mode separation processors must be designed at two output locations to effect mode separation in order to measure the average dispersion between the two outputs, it was desirable to obtain events which were recorded at several spatial locations. Two additional events were obtained even though their epicentral distances were larger than desired.

The first event is from Jalisco, Mexico, and has an epicentral distance of about 1800 km. Table II-5 describes associated PDE information for this event.

Table II-5

ASSOCIATED PDE INFORMATION
FOR
JALISCO, MEXICO, EVENT

Location	East of Jalisco, Mexico
Date	22 September 1965
Origin Time	14:36:10
Latitude	18.7° N
Longitude	107.3° W
Magnitude	4.8
Depth	33 km

Figure II-25 shows seismograms of this event in variable area display. Table II-6 gives the channel identification, distance and azimuth for each recording station. This event has 21 usable data channels recorded at seven spatial locations.

An examination of the event showed that the TFO radial and transverse components were transposed, while the radial component appeared to have about 6 db higher gain than the other channels. Also, the three Long Valley channels were inverted with respect to the other stations. All subsequent processing took the above observations into account.

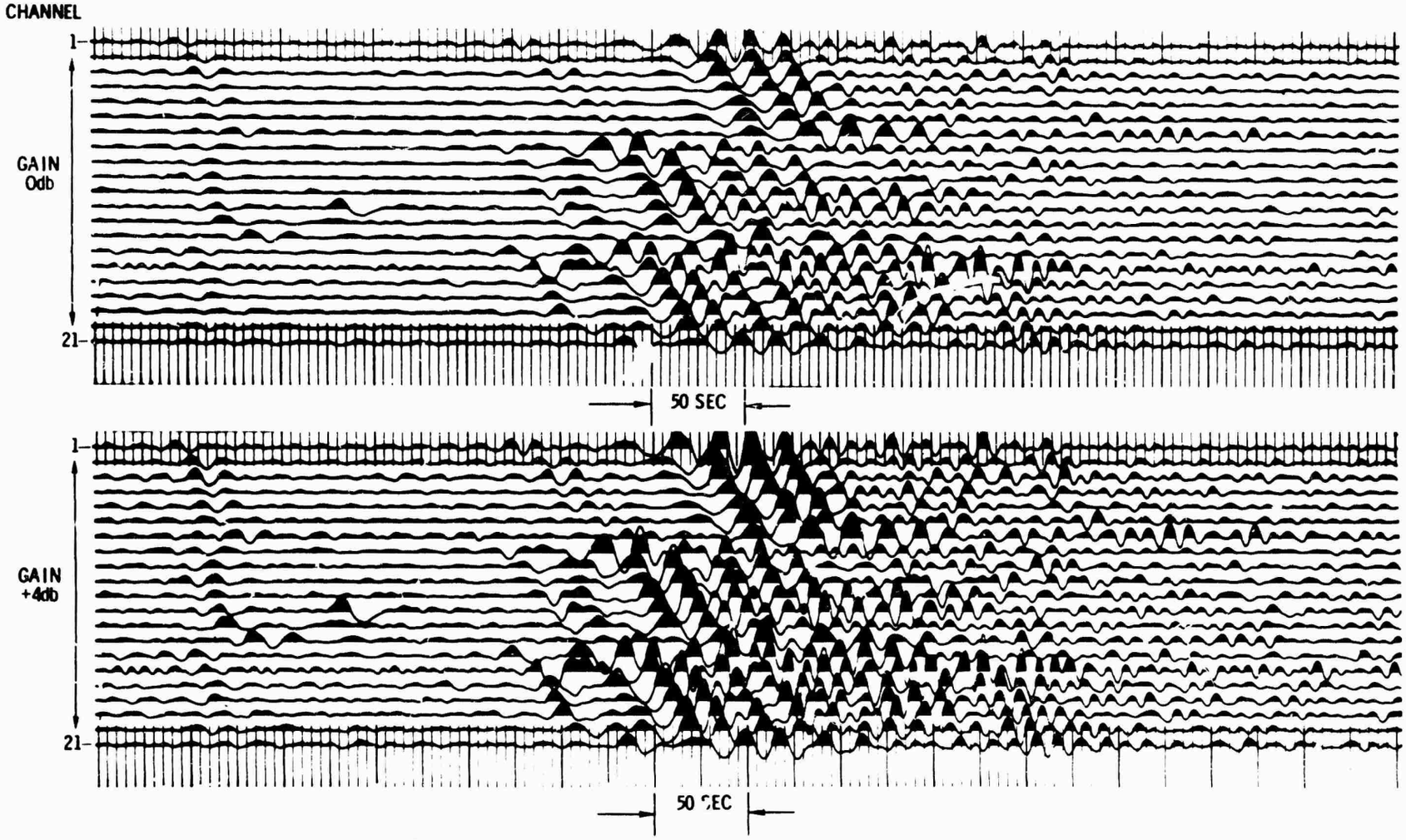

Figure II-25. Seismogram Recording of the Jalisco, Mexico, Event (Channel Identification is Given in Table II-6)

Table II-6

CHANNEL IDENTIFICATION, DISTANCE AND AZIMUTH
FOR JALISCO EVENT

Channel No.	Station Code	Component	Azimuth (Station to Epicenter)	Distance (km)
1	GE	Z	167.97°	1700.66
2	TFO	Z	166.14°	1767.11
3	LG	Z	165.34°	1788.39
4	HR	Z	168.15°	1800.26
5	WO	Z	168.78°	1820.58
6	JR	Z	164.25°	1843.76
7	SG	Z	161.09°	1964.49
8	GE	R	167.97°	1700.66
9	TFO	R	166.14°	1767.11
10	LG	R	165.34°	1788.39
11	HR	R	168.15°	1800.26
12	WO	R	168.78°	1820.58
13	JR	R	164.25°	1843.76
14	SG	R	161.09°	1964.49
15	GE	T	167.97°	1700.66
16	TFO	T	166.14°	1767.11
17	LG	T	165.34	1788.39
18	HR	T	168.15°	1800.26
19	WO	T	168.78°	1820.58
20	JR	T	164.25°	1843.76
21	SG	T	161.09°	1964.49

The second event is from Oaxaca, Mexico, and has an epicentral distance of about 2600 km. Table II-7 describes associated PDE information for this event.

Table II-7

ASSOCIATED PDE INFORMATION
FOR
OAXACO, MEXICO, EVENT

Location	Near Coast of Oaxaca, Mexico
Date	20 September 1965
Origin Time	11:31:43.6
Latitude	15.4° N
Longitude	94.6° W
Magnitude	4.3
Depth	58 km

Seismograms of the event are shown in Figure II-26. Table II-8 gives the channel identification and azimuth for each recording station.

4. Dispersion Estimates

Normal-mode dispersion in a plane-layered model simply corresponds to a frequency-dependent phase shift. Therefore, a transfer function may be determined which will propagate a given mode from one location to another which is a unit distance away. A single-channel spatial prediction filter, carrying one channel into the other, may be computed from the auto- and crosscorrelation functions of the two traces. This prediction filter is equivalent to the transfer function if only one mode is present. The dispersion of the mode may then be determined from the phase of the transfer function.

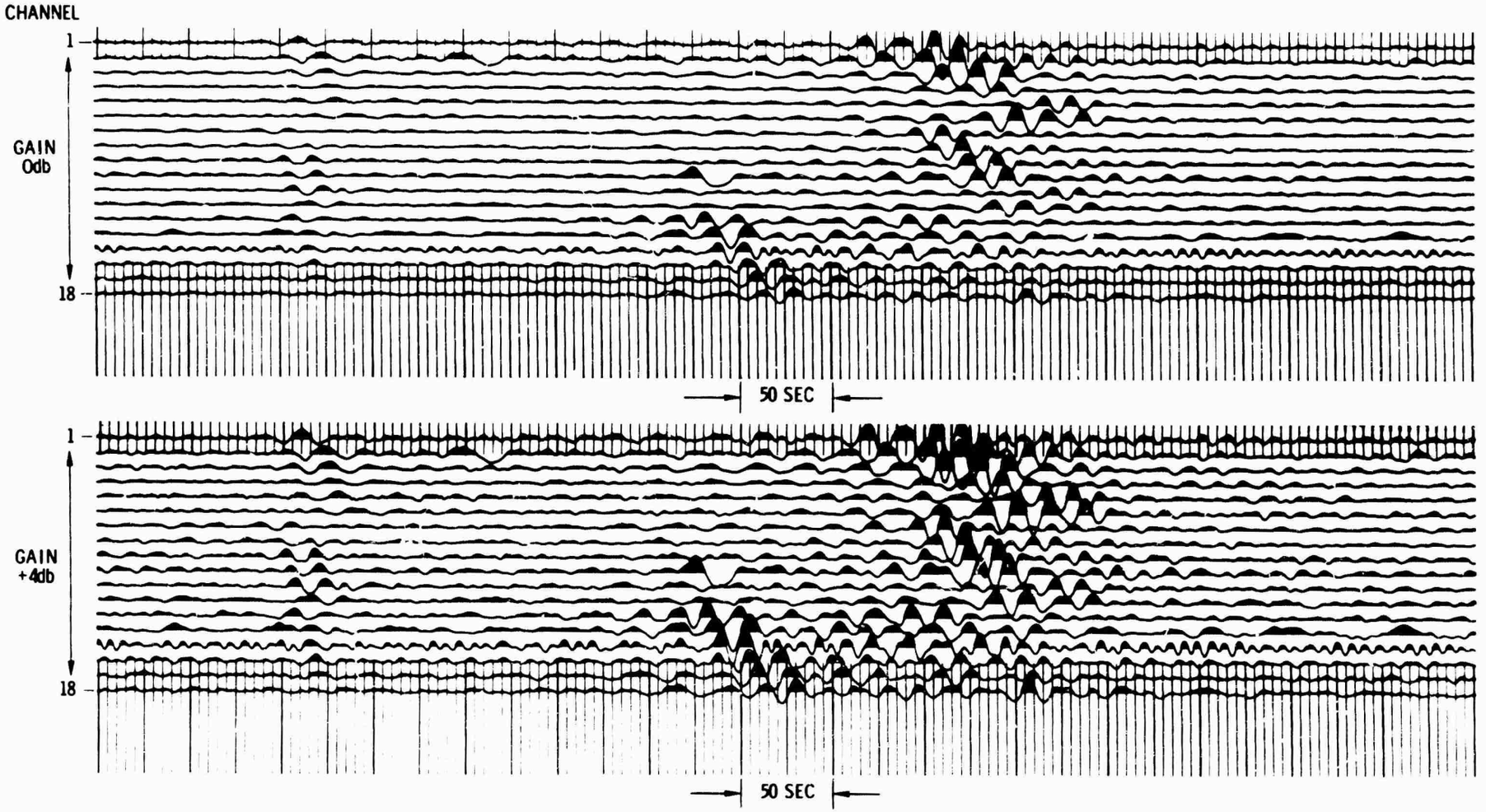

Figure II-26. Seismogram Recording of the Oaxaca, Mexico, Event (Channel Identification is Given in Table II-8)

Table II-8

CHANNEL IDENTIFICATION, DISTANCE AND AZIMUTH
FOR OAXACO EVENT

Channel No.	Station Code	Component	Azimuth (Station to Epicenter	Distance (km)
1	GE	Z	137.75°	2592.59
2	SN	Z	135.82°	2667.14
3	TFO	Z	137.25°	2672.85
4	WO	Z	139.42°	2684.08
5	NL	Z	142.68°	2707.22
6	JR	Z	136.72°	2763.10
7	GE	R	137.75°	2592.59
8	SN	R	135.82°	2667.14
9	HR	R	138.83°	2675.05
10	WO	R	139.42°	2684.08
11	NL	R	142.68°	2707.22
12	JR	R	136.72°	2763.10
13	GE	T	137.75°	2592.59
14	SN	T	135.82°	2667.14
15	TFO	T	137.25°	2672.85
16	HR	T	138.83°	2675.05
17	WO	T	139.42°	2684.08
18	JR	T	142.68°	2707.22

Rayleigh and Love wave dispersion estimates have been measured from the Southern California event using the vertical and horizontal components, respectively. Figure II-27 is a polar plot showing the azimuth and distance of each station from the epicenter. The Rayleigh wave dispersion estimates computed between various paris of stations are shown in Figure II-28 along with the theoretical dispersion curve for the TFO crust.

Agreement between the experimental and theoretical curves is good over the frequency range 0.025 to 0.175 cps in all cases except Jerome-to-Sunflower and Sunflower-to-TFO. An inspection of the polar plot (Figure II-27) shows that these two pairs of stations have epicentral separations which are smaller (40 and 30 km) than any of the other pairs used. Their dispersion curves agree somewhat between frequencies of 0.1 to 0.15 cps, where the wavelength being measured is of the order of or less than the station separation. This is consistent with the physical condition that if accurate dispersion measurements are to be made, the station separations should be equal to or greater than the wavelengths being measured. Another possible reason for the poor agreement between these two pairs of stations is that the Sunflower data channel has not recorded data faithfully.

Love-wave dispersion estimates were next computed by time partitioning the Love wave portion of the horizontal component with orientation more transverse to the great circle path from epicenter-to-station. The results, along with the theoretical dispersion curves, are shown in Figure II-29.

Next, the two horizontal components were rotated through the proper angle to give a horizontal component with orientation exactly transverse to the great circle path from epicenter-to-station. Dispersion measurements from the rotated components are also shown in Figure II-29.

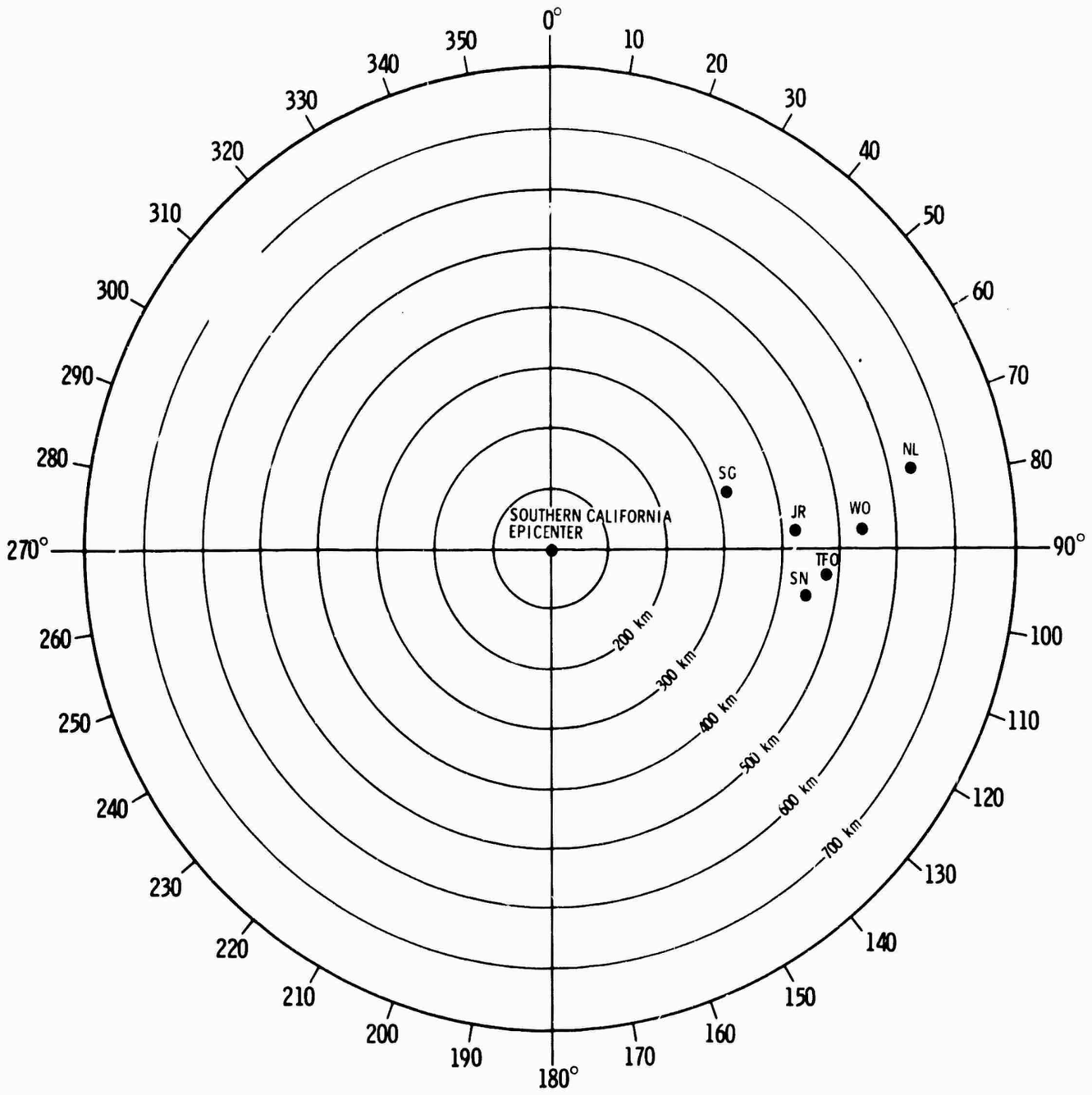

Figure II-27. Azimuthal Distribution of TFO Recording Stations for the Southern California Event

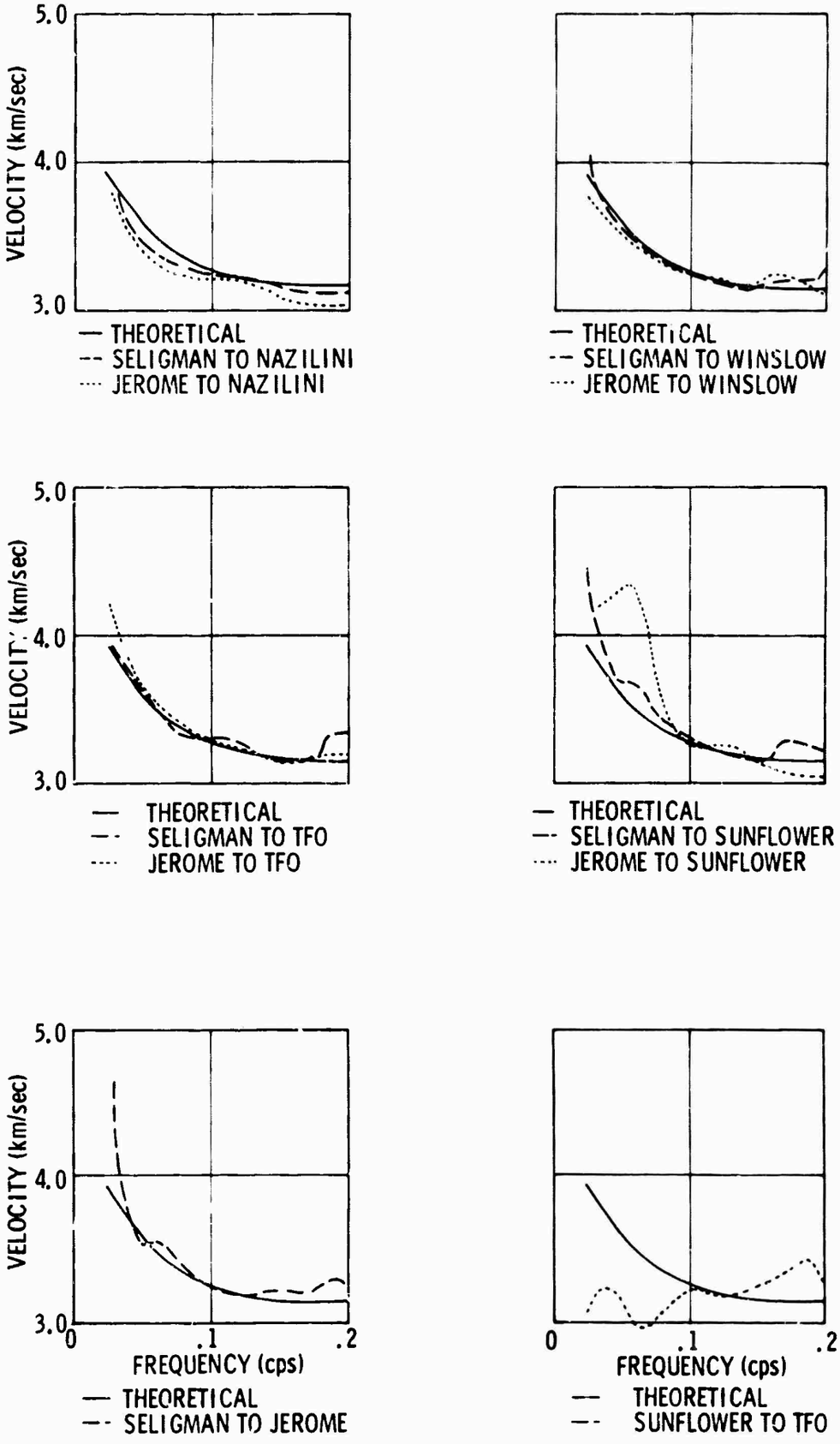

Figure II-28. Rayleigh Wave Dispersion Estimates Measured from the Southern California Event Using the Vertical Component

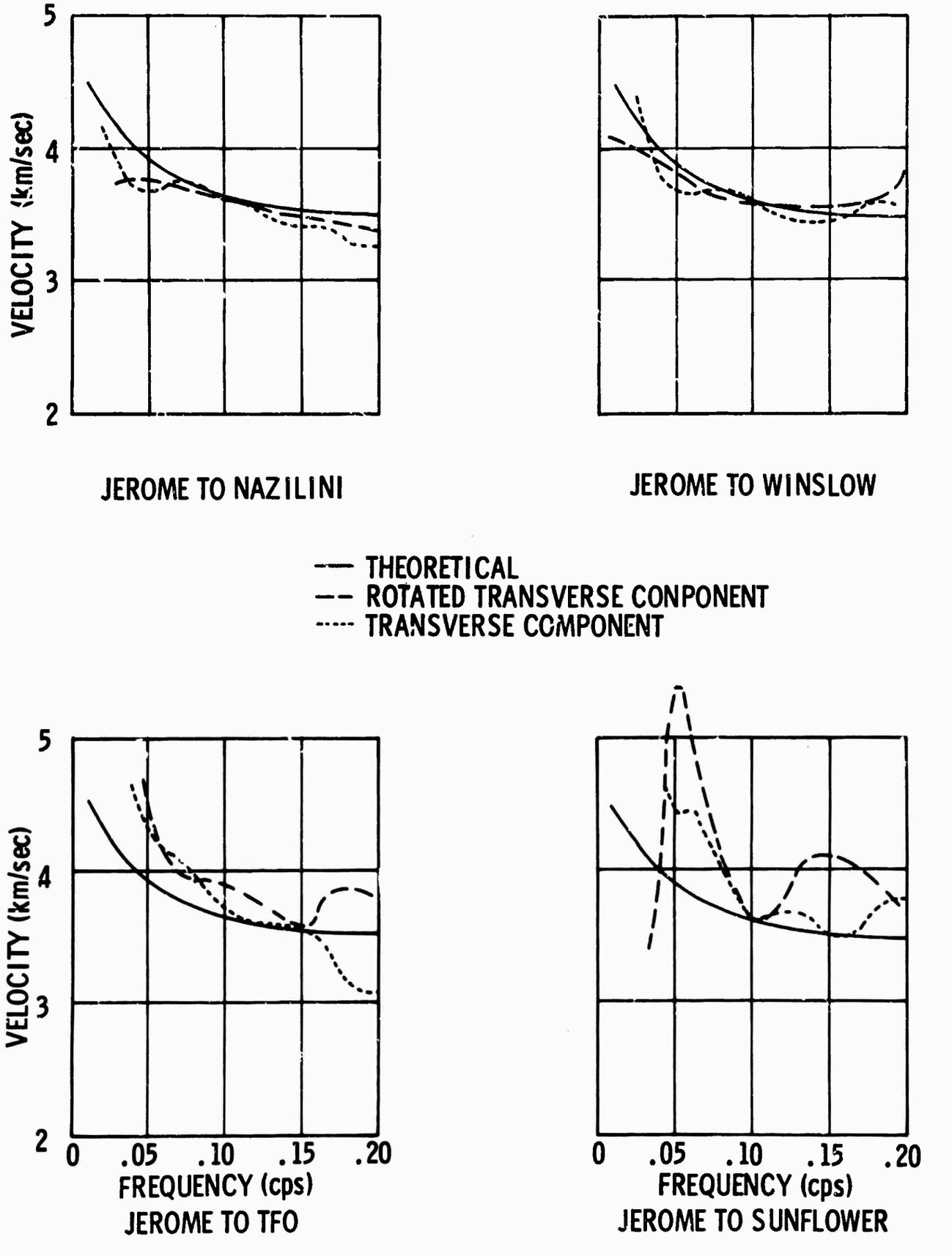

Figure II-29. Love Wave Dispersion Estimates Measured from the Southern California Event Using the Transverse Component

Agreement between experiment and theory is better after rotating the components, which is to be expected since the horizontal component before rotation will contain a horizontal component of the Rayleigh wave motion in addition to the Love wave. Here again the estimates are poor when the station separation is small (Jerome-to-TFO and Jerome-to-Sunflower).

5. TFO Model Fit

Dispersive wave motion is a common feature in seismic records, but despite the relative abundance of experimental data it is difficult to obtain precise dispersion information. Ideally, a dispersion analysis requires a strong source ($M \approx 6$) having a broadband frequency spectrum with the source situated at one end of an inline seismometer array. It is desirable that the array length be longer than the largest wavelength of interest ($\lambda = c/f$) by a minimum of several wavelengths, and that the spacing between detectors be approximately equal and small enough to allow consideration of low-velocity/high-frequency energy. Where possible, each seismograph should have three equalized components, and the path defined by the array should be free from major crustal irregularities. In no study are all of these conditions satisfied.

In the case of the long-period seismometer recordings obtained using the extended TFO array, the most interpretable modal energy, from the standpoint of dispersion, is the M_{11} shear mode. Since the dispersive behavior of this mode is well understood and readily measurable, it can be used as a partial check on the model. An experimental Rayleigh wave dispersion curve, obtained between the Seligman and Winslow sites (~ 260 km apart) for an earthquake originating in Southern California, was fitted (in the least-mean-square sense) by varying the shear velocities of layers 2 through 5 of the TFO model crust. This was done at 12 frequencies between 0.034 to 0.145 cps. Much of the crustal information contained in the lowest order TFO shear mode falls in this frequency band.

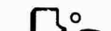

The resulting shear velocities (β) are β_2 = 2.95 km/sec, β_3 = 3.58 km/sec, β_4 = 4.08 km/sec, and β_5 = 4.54 km/sec (half-space). The layer 2 velocity decrease of 13.5 percent was the lone modification; all other changes were only about 0.1 percent. The dispersion points of the original model, the final adjusted model and the measured Rayleigh wave for the 12 frequencies are given in the first four columns of Table II-9.

Table II-9

MODEL INVERSION RESULTS

Frequency (cps)	Original Model (km/sec)	Experimental Data (km/sec)	Adjusted Model (km/sec)	Four Kilometer Model (km/sec)
0.035	3.78	3.72	3.72	3.68
0.045	3.65	3.57	3.61	3.54
0.055	3.52	3.51	3.51	3.43
0.065	3.43	3.44	3.42	3.34
0.075	3.36	3.36	3.36	3.28
0.085	3.31	3.31	3.31	3.23
0.095	3.27	3.27	3.27	3.19
0.105	3.24	3.24	3.24	3.15
0.115	3.23	3.21	3.21	3.12
0.125	3.21	3.18	3.19	3.09
0.135	3.19	3.16	3.17	3.07
0.145	3.19	3.16	3.16	3.04

At least one-half the data points of both models agree closely with the experimental points of the dispersion estimate. The two lowest frequencies, corresponding to wavelengths of the order of 105 km, show the greatest difference. Consequently, it seems odd that the relatively thin

second layer (4 km) undergoes such a drastic change while the remaining layers are essentially unaltered. The shear velocity of layer 1 (0.5 km thick) was not allowed to vary in the fit because the layer was so thin that it was not expected to influence dispersion at periods exceeding 10 sec. To a lesser degree, the same reasoning applies to layer 2. The low velocity of layer 2 in the adjusted model suggests that an increase in the thickness of the top layer might yield a better fit. The thickness of layer 1 was increased to 4 km, and again the shear velocities of layers 2 through 5 were allowed to vary while a least-mean-square fit of the dispersion curves was made. The layer 2 shear velocity decreased 1.2 percent, layer 3 velocityincreased 4 percent, layer 4 shear velocity increased 2.5 percent, and layer 5 shear velocity decreased 1.5 percent. The dispersion points computed with these new model parameters are given in the fifth column of Table II-9.

The agreement between the experiment and the 4-km model is not as good as that obtained with the original model. In order to quantitatively assess the significance of the velocity changes in going from one model crust to another, a program has been written to compute the derivative of the model phase velocity with respect to one of the following variables:

- Compressional velocity (α)
- Shear velocity (β)
- Density (ρ)

The derivative is computed at each frequency specified for each layer in the model. Thus, layer derivatives of phase velocity (C), with respect to shear velocity (β), can be plotted vs frequency. These curves indicate frequencies at which each each layer exerts its strongest effect for a small change $\Delta\beta$, in β.

Two plots (Figures II-30 and II-31) have been made for the two lowest order shear modes of the Table II-1 TFO model crust. The modal dispersion curves are most sensitive at low frequencies to changes in shear velocity of the half-space. Modifications of the uppermost layer's shear velocities have negligible effect at low freqeuncies and little effect at relatively high frequencies for these low-order modes. This means that the large increase in β_2 just discussed could only alter the dispersion curve slightly, which is the case.

The velocity parameters for layers 3 through 5 were suffi- accurate that they were not perturbed. The conclusion drawn is that the present crustal model for TFO (Table II-1) is adequate for the frequency range from 0.035 to 0.145 cps. A study now in progress is extending this frequency range to 0.22 cps and provides an additional check at the low frequencies. At present, the adequacy of the TFO crustal model for frequencies above 0.2 cps depends principally on its intimate association with a satisfactory low frequency model.

6. Mode Separation

This section deals with the problem of measuring experimental dispersion curves from long-period seismograms recorded by the TFO extended array. If a single mode could be recorded at two locations, then the dispersion curve for that mode could be determined by use of Fourier transform methods.[3,6]

As previously discussed, dispersion curves were measured from field recordings by time-partitioning the Rayleigh mode portion of the records and using Fourier transform methods on the raw data. Good agreement with theory was obtained because the fundamental Rayleigh mode overwhelms the other modes and may be considered to be the only mode present.

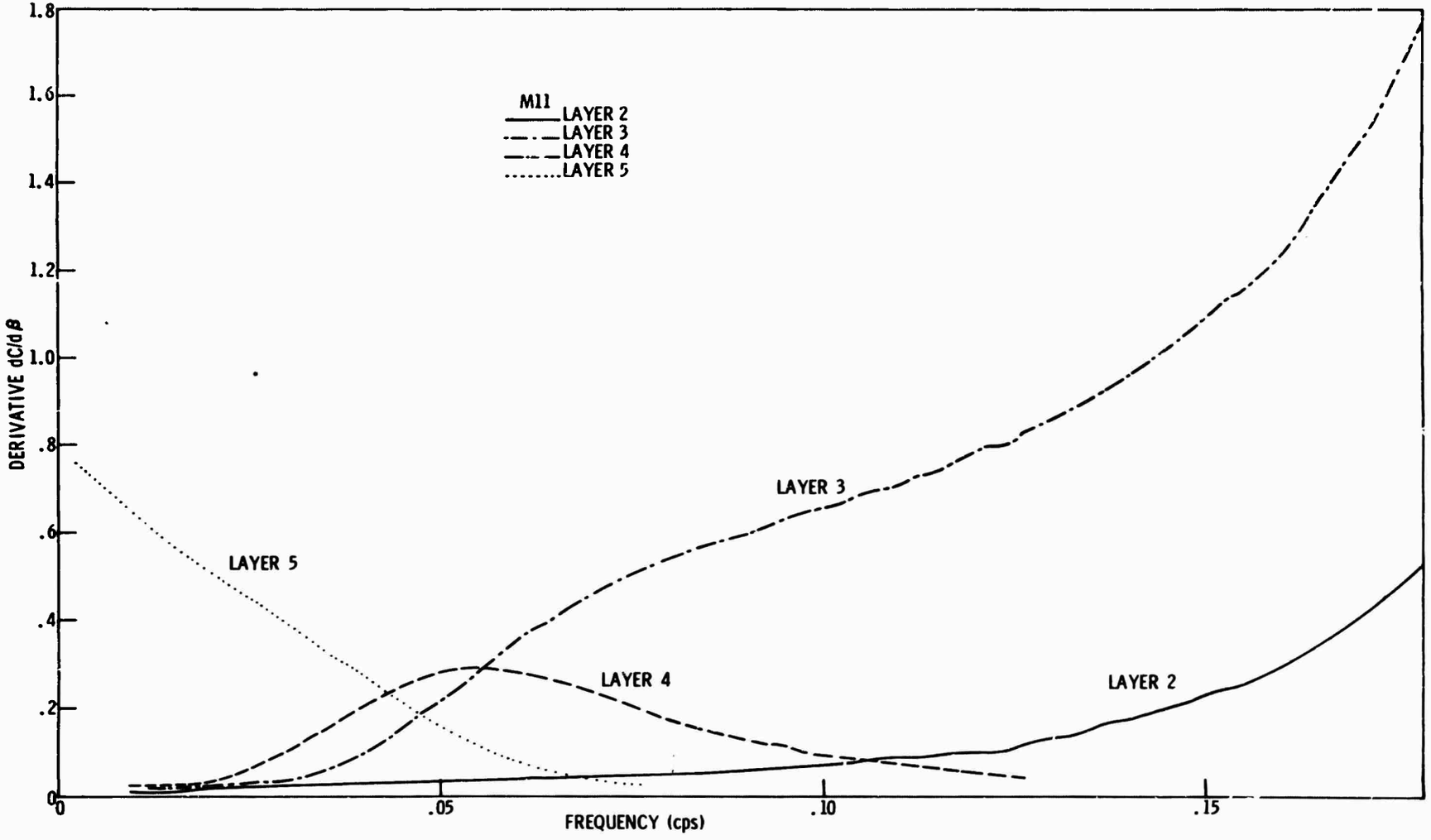

Figure II-30. Layer Derivatives for Normal Mode M_{11} at TFO

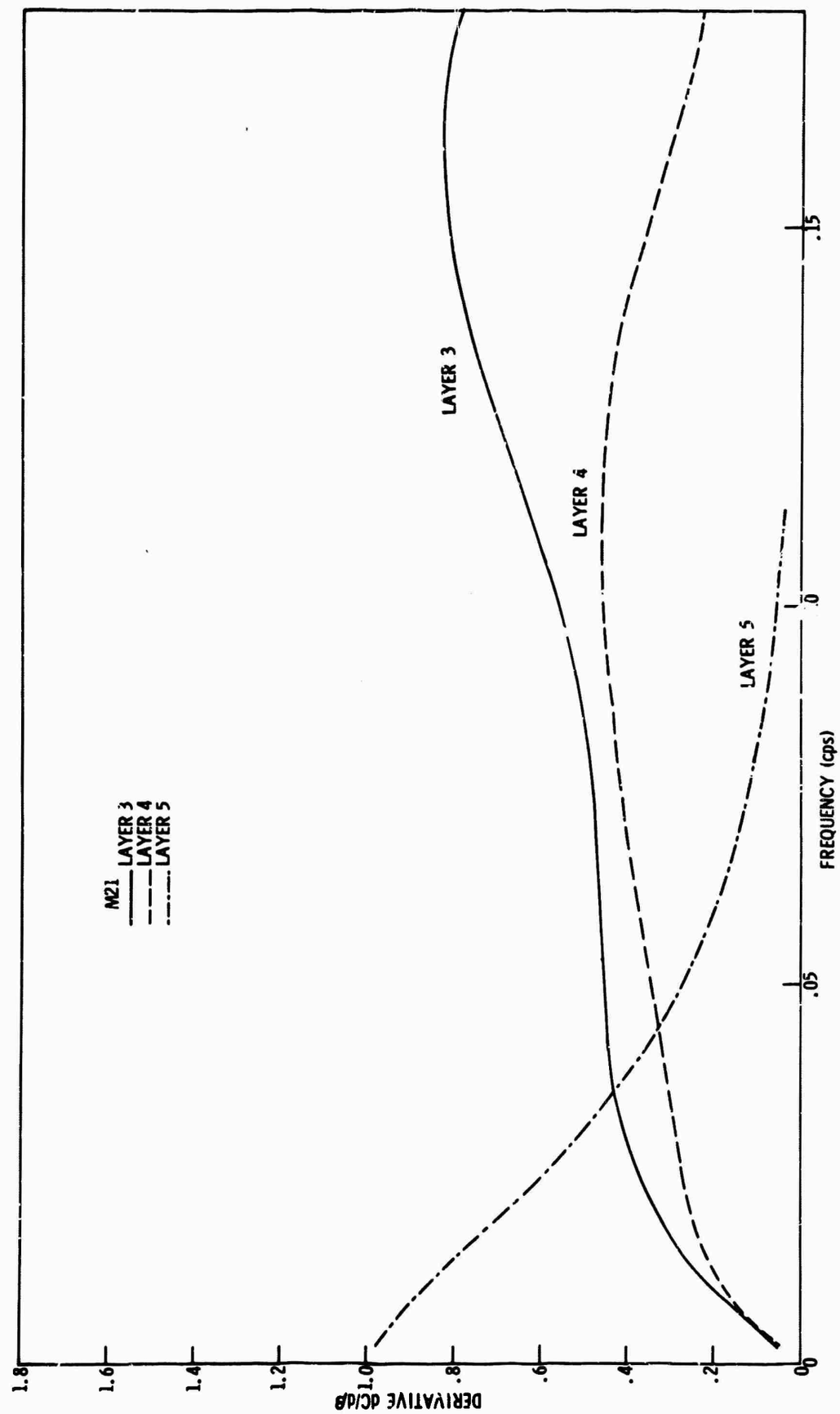

Figure II-31. Layer Derivatives for Normal Mode M_{21} at TFO

Theoretical computations predict that 10 higher-order normal modes may be expected in a crust such as TFO between frequencies of 0.0 and 1.0 cps, and these modes will have relatively small amplitudes compared to the fundamental Rayleigh mode. In order to separate these higher-order normal modes which overlap the Rayleigh mode in both arrival time and frequency, it is necessary to apply a mode separation technique which makes use of the frequency dependent phase velocity of dispersive modes.

The Jalisco event was selected for mode separation since it was recorded at more spatial locations than either the Southern California event or the Oaxaca event. Figure II-32 shows a polar plot of the station locations and azimuths from the Jalisco epicenter.

Autocorrelation functions were computed from the vertical time traces recorded at Globe, TFO and Seligman. The time gate used in the correlation process contained the entire event from P-wave through Rayleigh coda. Spectra of the autocorrelation functions are shown in Figure II-33. The energy is strongly peaked at 0.05 cps. The recording system has essentially bandlimited this data so that it contains no energy above 0.15 cps.

Theoretical dispersion curves computed for the crust at TFO show that only two normal modes may be present on these long period recordings — the fundamental Rayleigh mode (M_{11}) and the first shear mode (M_{21}). Therefore, the problem is designing multichannel mode separation filters and applying them to the separation of a relatively small amplitude mode (M_{21}) in the presence of an overwhelming mode (M_{11}).

Two different array processing schemes were used for mode separation. The first makes use of frequency-velocity and amplitude relationships (one component), while the second makes additional use of the horizontal-vertical relationships (two components).

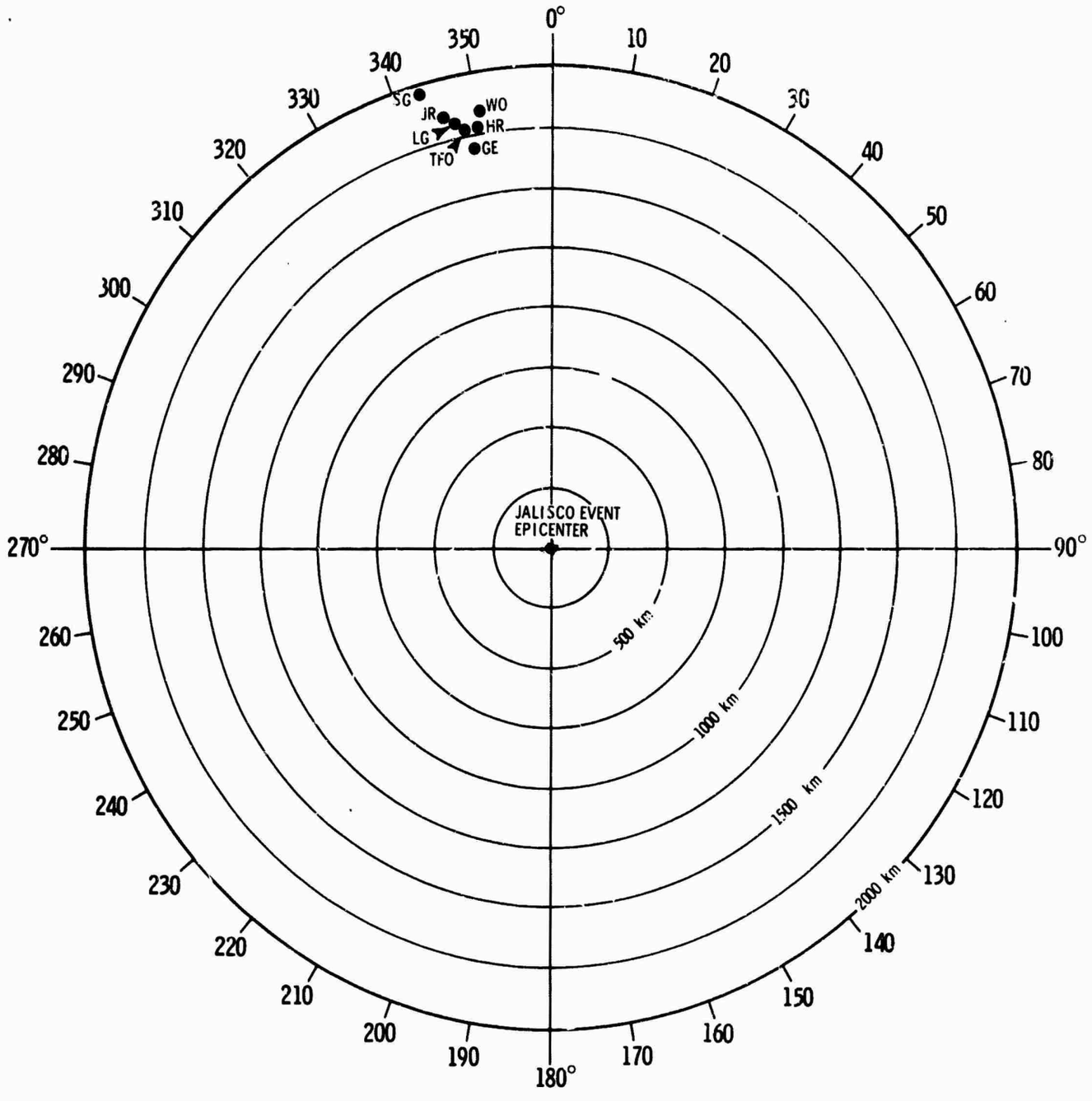

Figure II-32. Azimuthal Distribution of TFO Recording Stations from the Jalisco Event

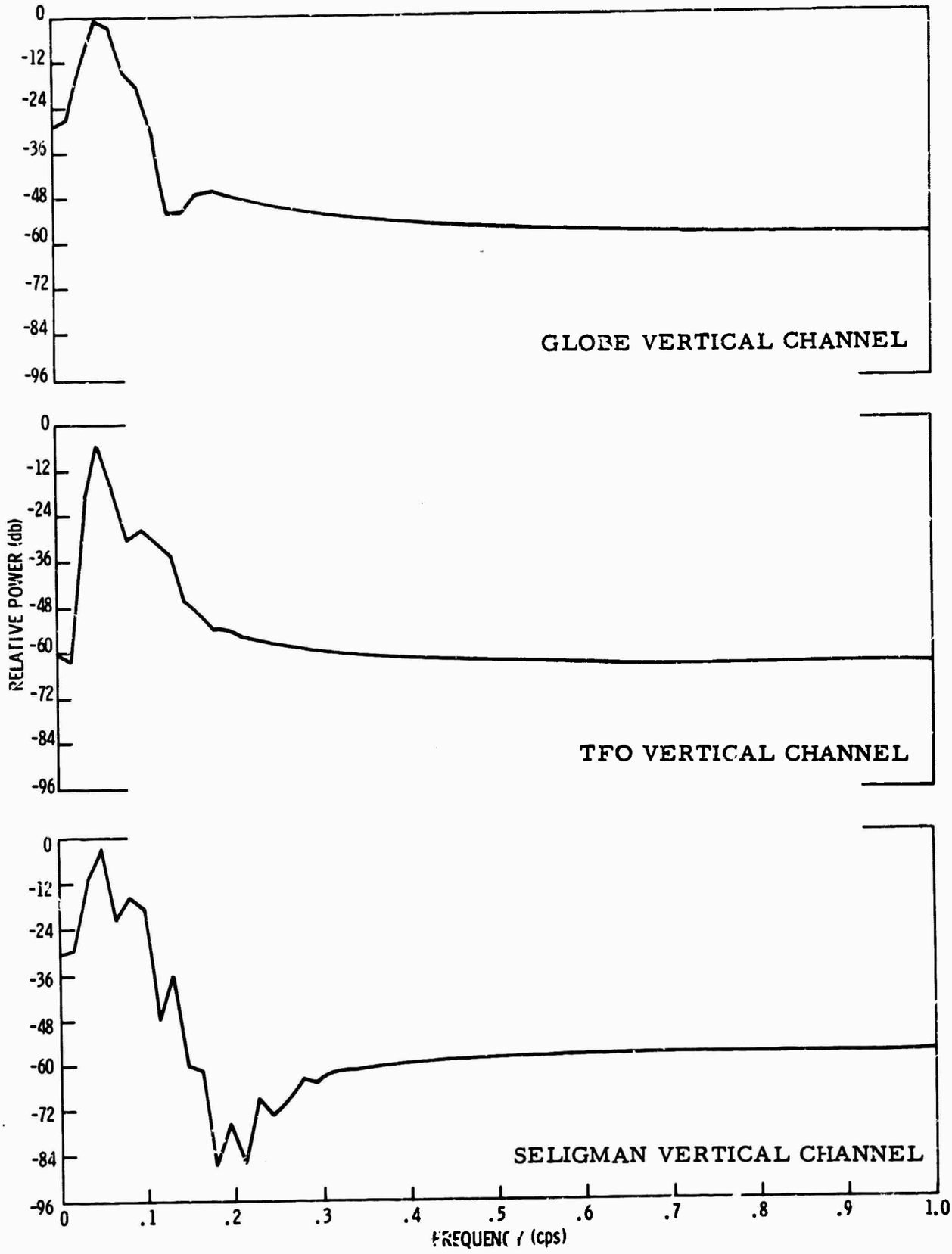

Figure II-33. Frequency Spectrum of Autocorrelations for the Jalisco Event

a. 1-Component Filter Design

In the time domain, the system of m filters, which yield the minimum mean-squared-error for a fixed filter length r, is given by the solution $y_j(t)$ of the equation

$$\left[\Phi_{ij}(\tau)\right]\left[y_j(\tau)\right] = \left[\Phi_{io}(\tau)\right]$$

where

$\left[\Phi_{ij}(\tau)\right]$ is the rm x rm matrix of cross-correlations of signal plus noise

$\left[y_j(\tau)\right]$ is the rm x 1 matrix of filter operator points

$\left[\Phi_{io}(\tau)\right]$ is the rm x 1 matrix of signal crosscorrelation between the input channels and the output channel

Specified in the filter design are the signal mode M_{21}, noise consisting of the Rayleigh mode M_{11} and two nondispersive waves propagating at 8 and 6 km/sec. The auto- and crosspower spectra were computed for the four modes using the theoretically computed dispersion and vertical excitation functions for M_{11} and M_{21}. The two nondispersive waves were specified to have a constant power level about 6 db less than the signal mode, M_{21}. These auto- and crosspower spectra were then inverse Fourier transformed to give the correlation statistics required for filter design in the time domain.

Two sets of filters were designed to operate on independent data traces to separate the signal mode at two output locations. The first filter set used Globe, Long Valley, Winslow, and Jerome data channels. The second used TFO, Heber and Seligman data channels. The seven spatial

locations were divided into 4- and 3-channel processes in order to choose the spatial locations which would maximize the aperature needed by each processor to effect mode separation at low frequencies.

Because of the large aperature (143 km for the 4-channel process and 197 km for the 3-channel process), very long filters (50-sec) are needed to span the moveout of the lowest velocity event across the process. However, shorter filters were designed by shifting the correlation functions to a reference velocity between the P and Rayleigh velocities and then designing the filters using these shifted correlations. Filters designed in this manner were applied to the shifted seismograms.

The sample interval of the seismograms is 0.5 sec. Since the seismograms contain no energy above 0.15 cps, it was possible to compute the correlation functions at a 2-sec sample interval without frequency aliasing. This reduced the number of filter points required to span the moveout.

The correlation functions used to solve the time-domain matrix equation and the 11-point filter solutions along with the array geometry of the channels used are shown in Figures II-34 and II-35 (4- and 3-channel process).

The f-k responses of these filter sets (Figures II-36 and II-37) were computed in order to determine their rejection capabilities. Each response has been normalized to the largest value of power in the f-k response. Each contour in the figures represents a range of 6-db rejection, and the theoretical dispersion characteristics of the signal and noise are shown as solid lines. In both cases, the M_{21} mode is passed and the M_{11} mode is rejected by 12 to 24 db. The filters are working hardest to reject the large amplitude Rayleigh mode. Moreover, some rejection of the two nondispersive waves has also been achieved — particularly by the 4-channel process (Figure II-36).

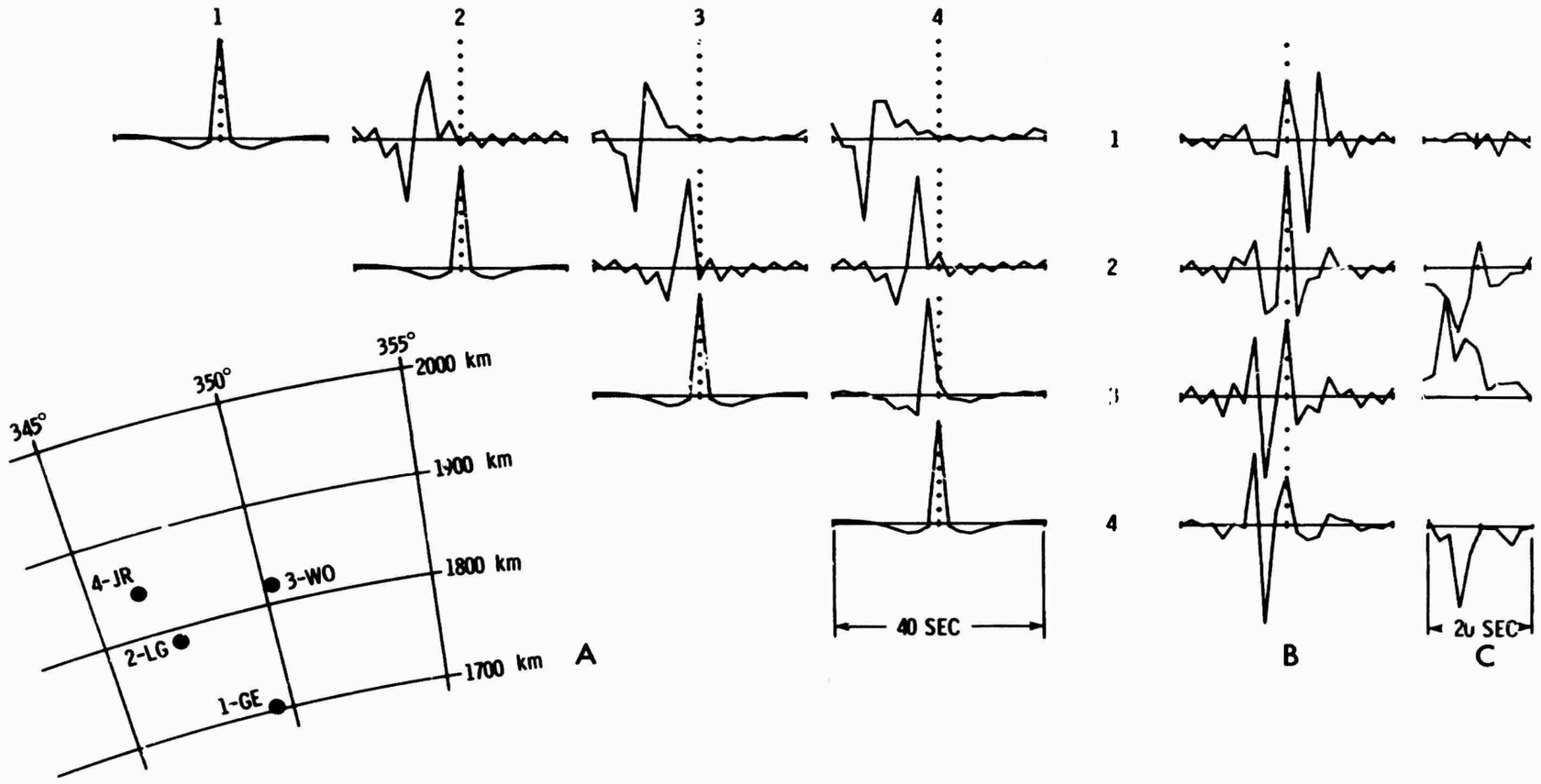

(A) Crosscorrelation functions to form the signal plus noise matrix

(B) Signal crosscorrelation functions between the input channels and the output channel to form the signal matrix

(C) The 4-channel, 11-point filters designed to separate M_{21}

Figure II-34. Theoretical Correlation Functions for 4-Channel Filter Design

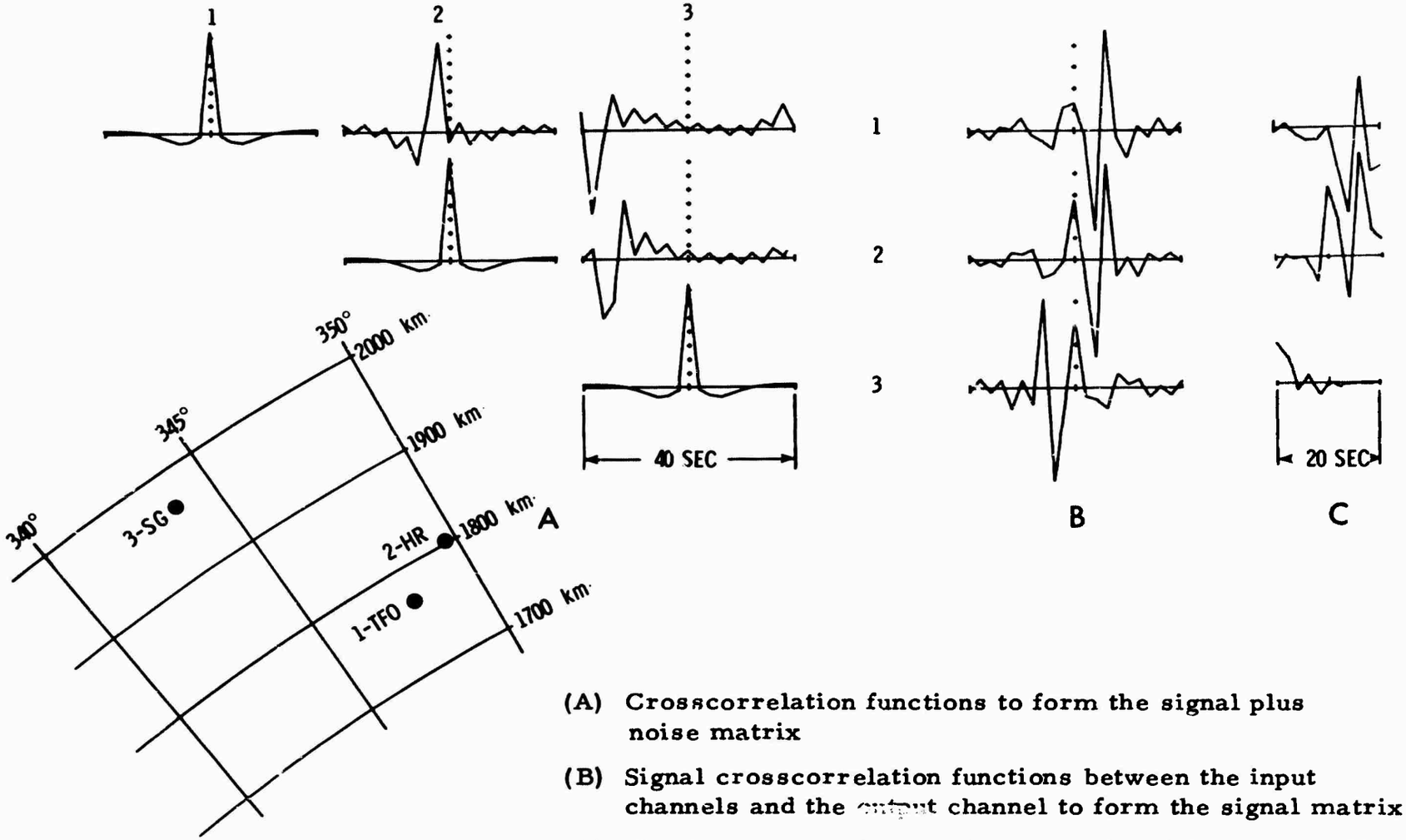

(A) Crosscorrelation functions to form the signal plus noise matrix

(B) Signal crosscorrelation functions between the input channels and the output channel to form the signal matrix

(C) The 3-channel, 11-point filters designed to separate M_{21}

Figure II-35. Theoretical Correlation Functions for 3-Channel Filter Design

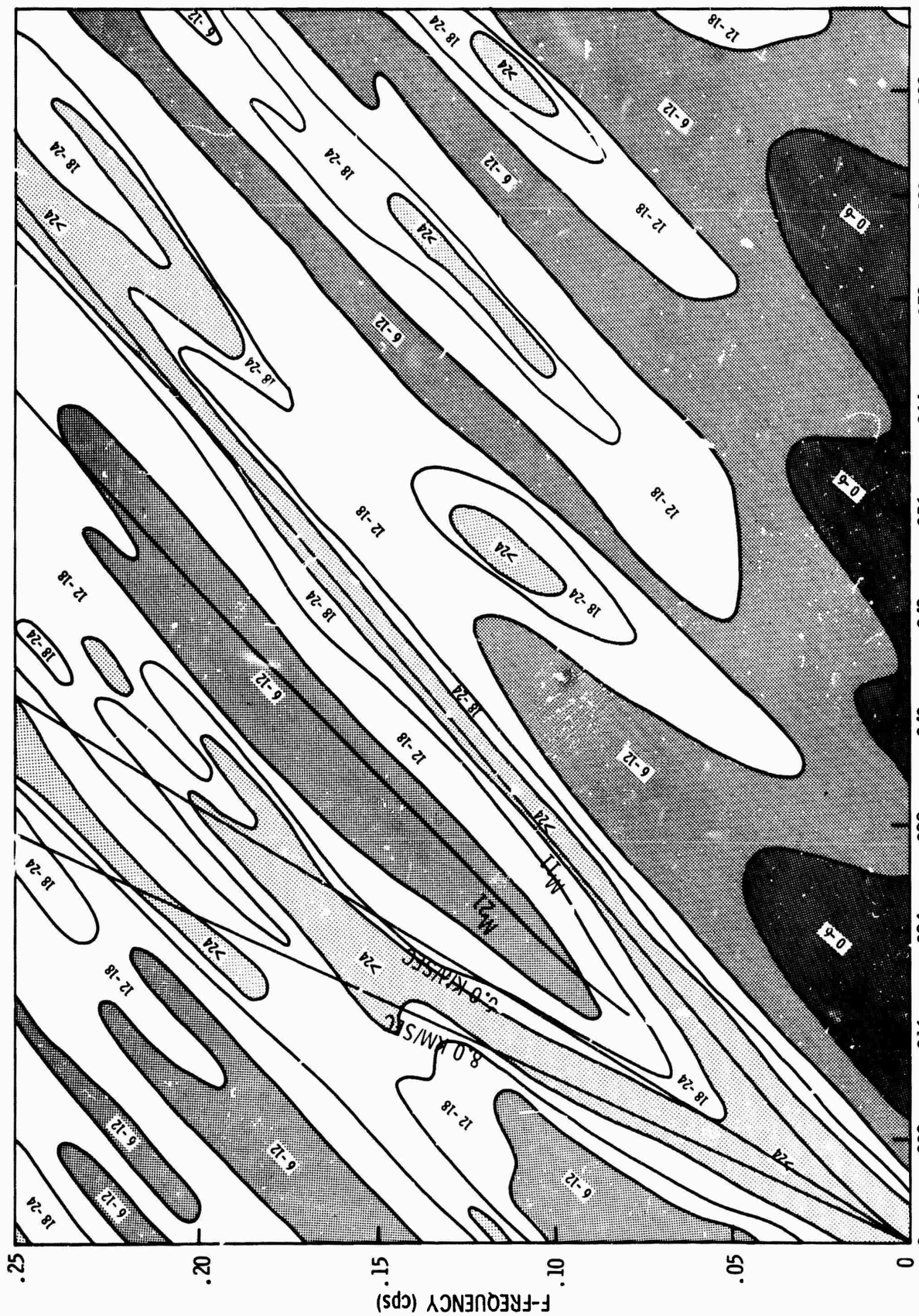

Figure II-36. f-k Response of the 4-Channel Mode-Separation Filters, M_{21} Signal

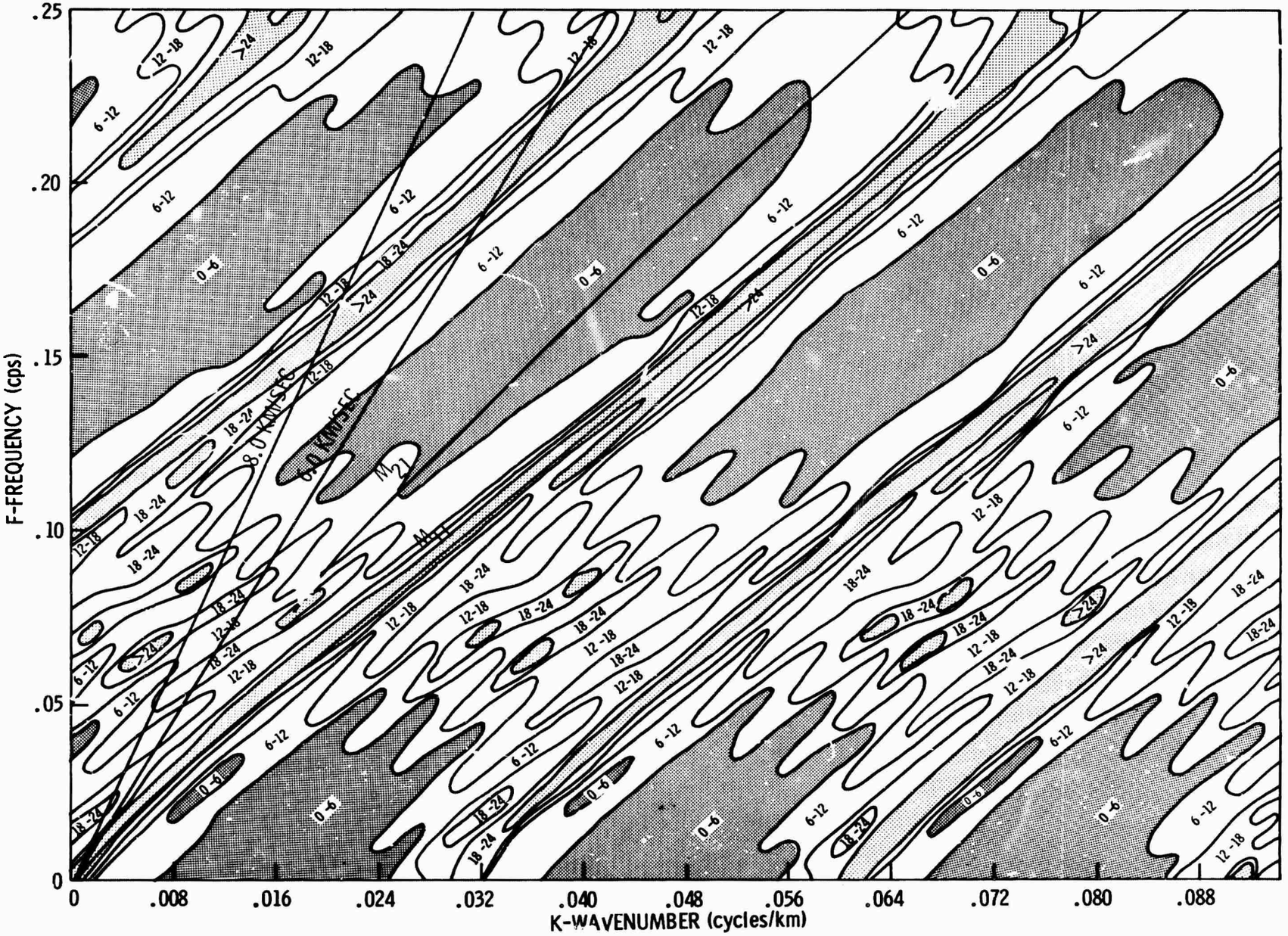

Figure II-37. f-k Response of the 3-Channel Mode-Separation Filters, M_{21} Signal

The other areas of high response (0 to 6 db) are regions where there is neither signal nor noise. In these regions, no constraints are placed on the response by the filter design.

b. Two-Component Filter Design

Another type of mode separation processor was designed to use data recorded on vertical and inline horizontal seismometers. Two sets of filters (8- and 6-channel processors) were designed using two components at each spatial location. The spatial locations used are the same as for the 1-component processors just discussed.

The filters were designed using correlation statistics computed in the same manner as for the 1-component processor. The matrix of correlations and the filter solutions for the 8- and 6-channel processors are shown in Figures II-38 and II-39, respectively. There is no dispersion between two components at a single spatial location. However, there is a $\pm 90^{\circ}$ phase shift for the normal modes between horizontal and vertical components, and their excitation amplitudes differ.

The performance of the 2-component processors is expected to exceed that of the 1-component processors. This is presuming that the horizontal and vertical instruments have the same response characteristics and that the recordings are accurately gain equalized. The later is particularly important, since the two horizontal components must be used in rotating the coordinate system to produce an inline horizontal seismogram.

c. Rotation of Components

Two horizontal components of motion (radial and transverse) are recorded at each location. The 2-component processors require one horizontal component oriented inline with the event, necessitating the rotation of the coordinate system.

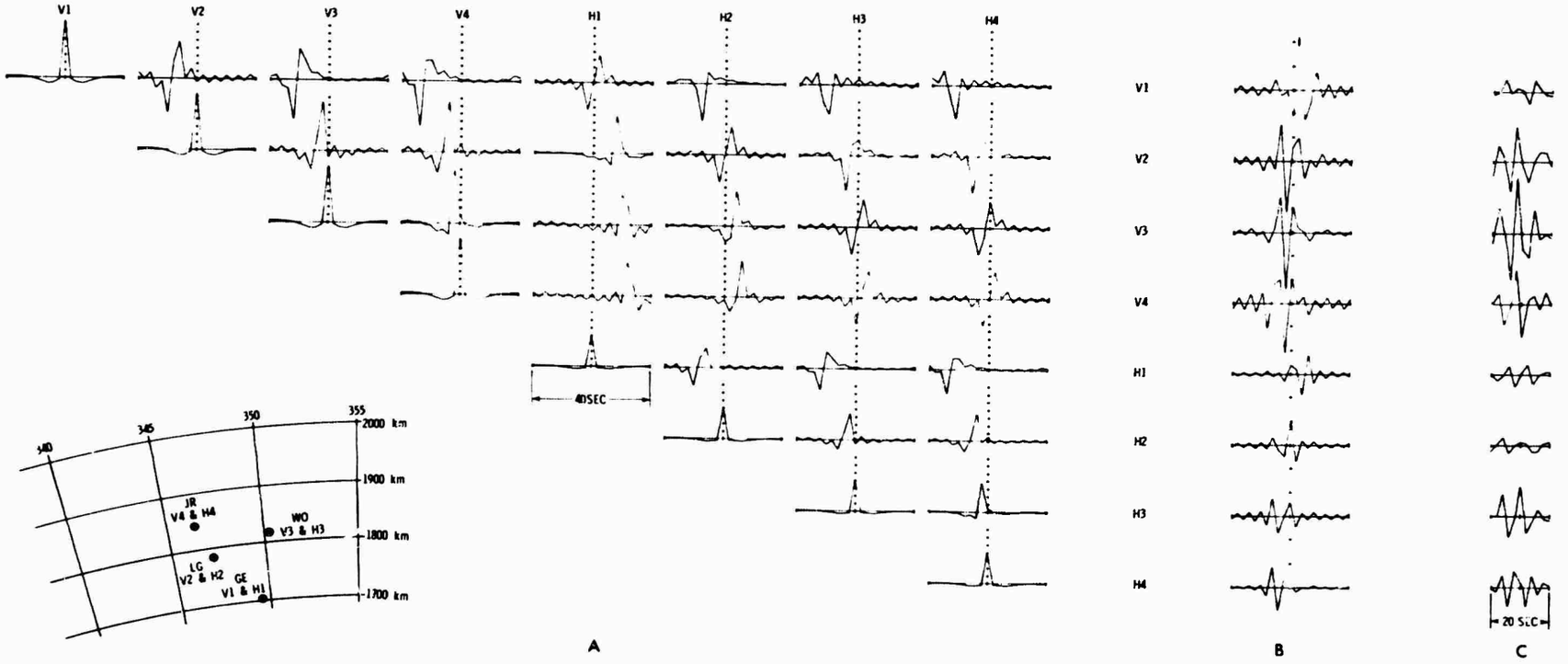

The eight channels are the verticals and horizontals at four spatial locations

(A) Crosscorrelation functions to form the signal plus noise matrix

(B) Signal crosscorrelation functions between the input channels and the output channel to form the signal matrix

(C) The 8-channel, 11-point filters designed to separate M_{21}

Figure II-38. Theoretical Correlation Functions for 8-Channel Filter Design

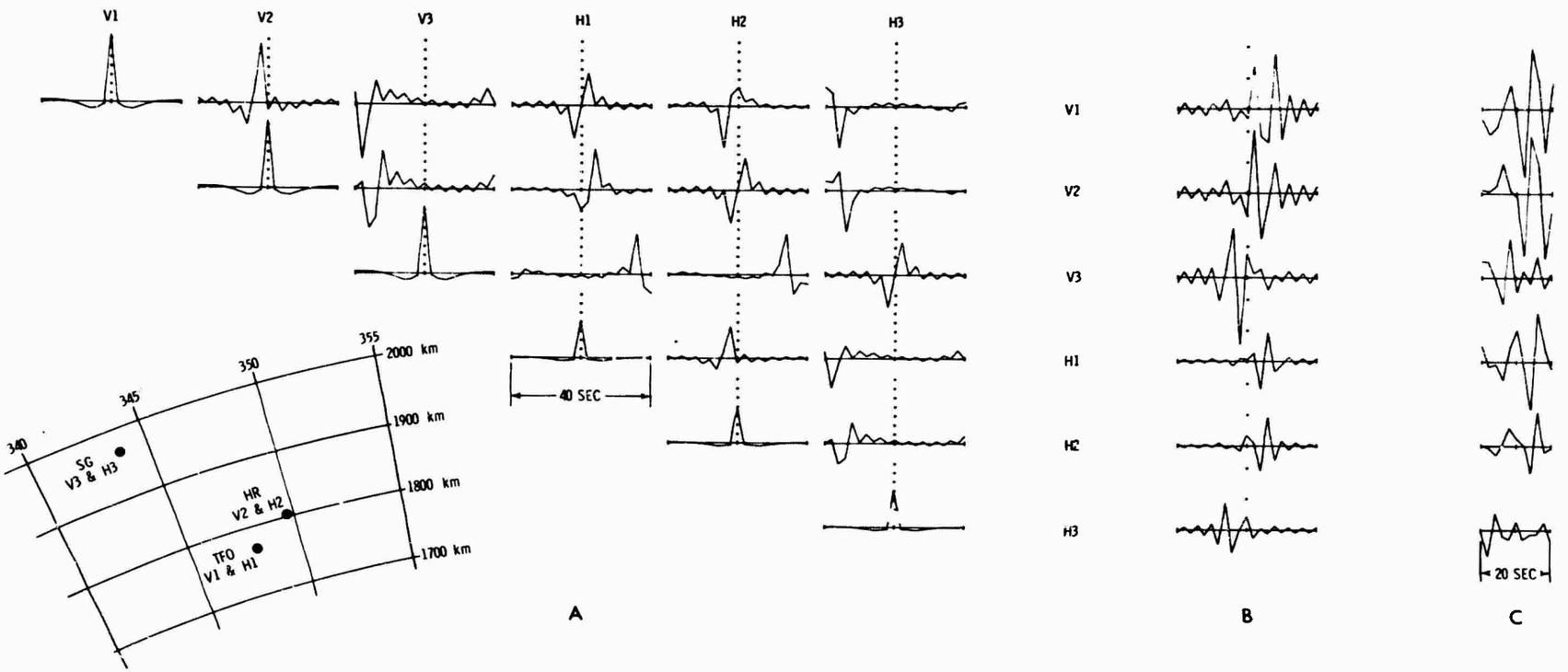

The six channels are the verticals and horizontals at three spatial locations

(A) Crosscorrelation functions to form the signal plus noise matrix

(B) Signal crosscorrelation functions between the input channels and the output channel to form the signal matrix

(C) The 6-channel, 11-point filters designed to separate M_{21}

Figure II-39. Theoretical Correlation Functions for 6-Channel Filter Design

The rotation of the cocrdinate system uses the formula

$$R'(t) = R(t) \cos \theta + T(t) \sin \theta$$

for each time t. Where

R = Amplitude of the radial component

T = Amplitude of the transverse component

θ = Angle through which the radial component must be rotated in order to be inline with the computed great circle azimuth to the source

The next step is to apply mode separation filters to the inline horizontal and vertical seismograms by the multichannel convolution and summation process.

d. Errors

The data used in this analysis have been equalized at SDL by applying scale factcrs computed from calibrating the instruments. Power spectra computed from the equalized traces show the peak power to be nearly equal, indicating adequate equalization. Also, the mean of several traces was computed and found to be very close to zero.

Random gain fluctuations appear as spatially uncorrelated noise, the wavenumber spectrum of which may be assumed constant. If random differences in receiver gains between channels occur, they may be introduced into the mode separation filter design by scaling up the auto-correlations. This will extend the applicability of the processor at the expense of degrading the filter response. In the filter design previously described, no noise has been added.

In addition, it is absolutely necessary that the channels be gain-equalized since the horizontal components must be rotated to produce an inline and a transverse trace.

Another source of error is that the horizontal and vertical instruments may have different response characteristics. If the instruments are not matched, the individual responses must be used to correct the recorded signals. No correction was made on the present data since individual instrument responses were not available.

None of the events were directly inline with either arm of the TFO extended array. The seismometer positions were, in effect, projected (by using circular arcs) onto a linear array inline with the event. This is valid for an earth model consisting of plane parallel layers. Theoretical mode separation filters then were designed using the spacings of the constructed linear inline array.

e. Application

The theoretically computed mode separation filters were applied to the experimental seismograms using the multichannel convolution and summation process. The results from the 4- and 3-channel processors show that the Rayleigh wave was not rejected as much as was predicted by the computed filter response. The large Rayleigh wave residual precludes any measurement of M_{21} dispersion which may be present. This suggests important differences between the assumed theoretical model and this experimental data.

Attempts have been made to find the cause of the large Rayleigh wave residual. Rayleigh wave dispersion estimates were computed for the Jalisco event by time-partitioning the Rayleigh wave portion of the records and computing the dispersion between pairs of stations.

The estimates are very poor in that they do not agree between various pairs of stations nor do they agree with the theoretical curves. This is surprising, since very good agreement was obtained from the Southern California event using the same methods.

Next, the Oaxaca event was time-partitioned and Rayleigh dispersion estimates were computed. The results were even worse than for the Jalisco event.

The experimental f-k characteristics for the Jalisco and Oaxaca events differ from the assumed theoretical f-k characteristic. Therefore, the Rayleigh wave will not fall in the M_{11} notch shown in the filter responses (Figures II-36 and II-37) but will fall on the sides of the notch, giving very little rejection.

Dispersion estimates from the Southern California event agree well with theory, while these from Jalisco and Oaxaca show significant differences. There are two important differences in the data. First, the Jalisco and Oaxaca events have large epicentral distances (1700 and 2600 km) compared to the Southern California event (500 km), and second, the surface waves from the Jalisco and Oaxaca events are traveling roughly S-N across the array while the direction of propagation is W-E for the Southern California event. Lateral inhomogeneity could explain some of the difference between theory and experiment; however, the exact cause is not known at present.

C. LASA CRUSTAL MODEL

1. Geophysics of Large Aperture Seismic Array

The model crust selected for the Large Aperature Seismic Array (LASA) in Montana is based on the 1959 measurements of Steinhart and Meyer (1959).[1]

A detailed profile was recorded from Acme Pond north to the Ft. Peck reservoir in eastern Montana (Figure II-40). The Carnegie Institution of Washington, D.C., recorded along several profiles oriented E-W using the same shotpoints. The geologic cross-section associated with the Eastern Montana crust is fairly simple[1] with plane-layer type formations. From the standpoint of mode theory, the ideal geology of the LASA crust offers the best experimental circumstances to date.

Several crustal models satisfying observed travel times and exhibiting the same closure times at both ends of the previously mentioned profiles were derived as best approximations to the actual thickness and velocity structure of the Montana crust. The LASA model parameters are given in Table II-10. Again, the shear velocities have been computed by means of Poisson's relation. The depth to the M discontinuity is 50.3 km; thus, dispersive effects, based on the entire crust, will become noticeable at wavelengths near 50 km. Wavelengths this long or longer correspond to frequencies below 0.1 cps for typically observed shear waves. Higher-order modes show dispersion at higher frequencies but are commonly less strongly excited.

Table II-10

PHYSICAL PARAMETERS FOR LASA CRUSTAL MODEL

Layer	Compressional Velocity, α (km/sec)	Shear Velocity, β (km/sec)	Layer Thickness (km)
1	2.60	1.50	0.3
2	3.70	1.85	3.0
3	6.08	3.51	20.0
4	6.97	4.02	17.0
5	7.58	4.38	10.0
Half-space	8.07	4.66	∞

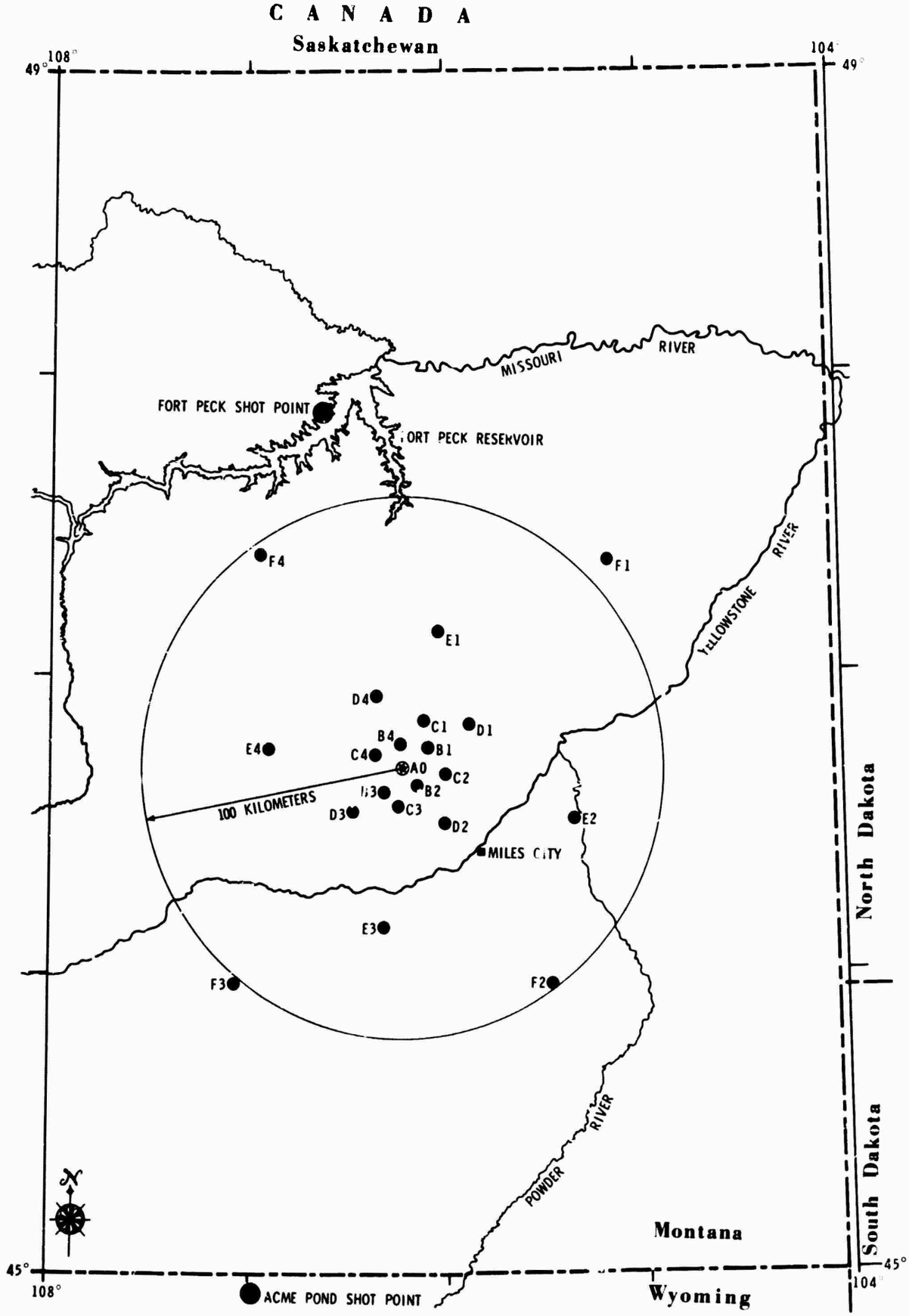

Figure II-40. Large Aperture Seismic Array in Eastern Montana

At this time, long-period data are not available for the LASA site. However, short-period recordings covering the band from 0.5 to 2.0 sec have been obtained. Dispersive phenomena at these short periods can best be studied by considering only the uppermost layers in the model of Table II-10 because these layers exercise the greatest control over the dispersion at high frequencies. Consequently, modal dispersion and excitation for the simple 3-layer model of Table II-11 were computed.

Table II-11

PHYSICAL PARAMETERS FOR
HIGH FREQUENCY LASA CRUSTAL MODEL

Layer	Compressional Velocity, α (km/sec)	Shear Velocity, β (km/sec)	Layer Thickness (km)
1	2.6	1.5	0.3
2	3.7	1.85	3.0
Half-space	6.08	3.51	∞

2. Mode Calculations for LASA Crust

The preliminary LASA calculations were made with a $\Delta f = 0.04950495$ cps based on a sample time of 0.2 sec and a time window 20.2 sec long. (This gives a folding frequency of 2.5 cps.)

Nine normal modes were found between 0.0 and 2.5 cps, and plots of their phase velocity vs frequency are displayed in Figure II-41. The M_{11} shear mode velocity decreases rapidly from 0.0 to 0.35 cps, approaching the 1.5 km/sec shear velocity of the top layer at 2.5 cps. The next two modes, M_{21} and M_{12}, do not disperse as rapidly; their limiting velocity at 2.5 cps is close to 1.85 km/sec, the shear velocity of the second layer. The modes above M_{22} have not closely approached any layer velocity at 2.5 cps.

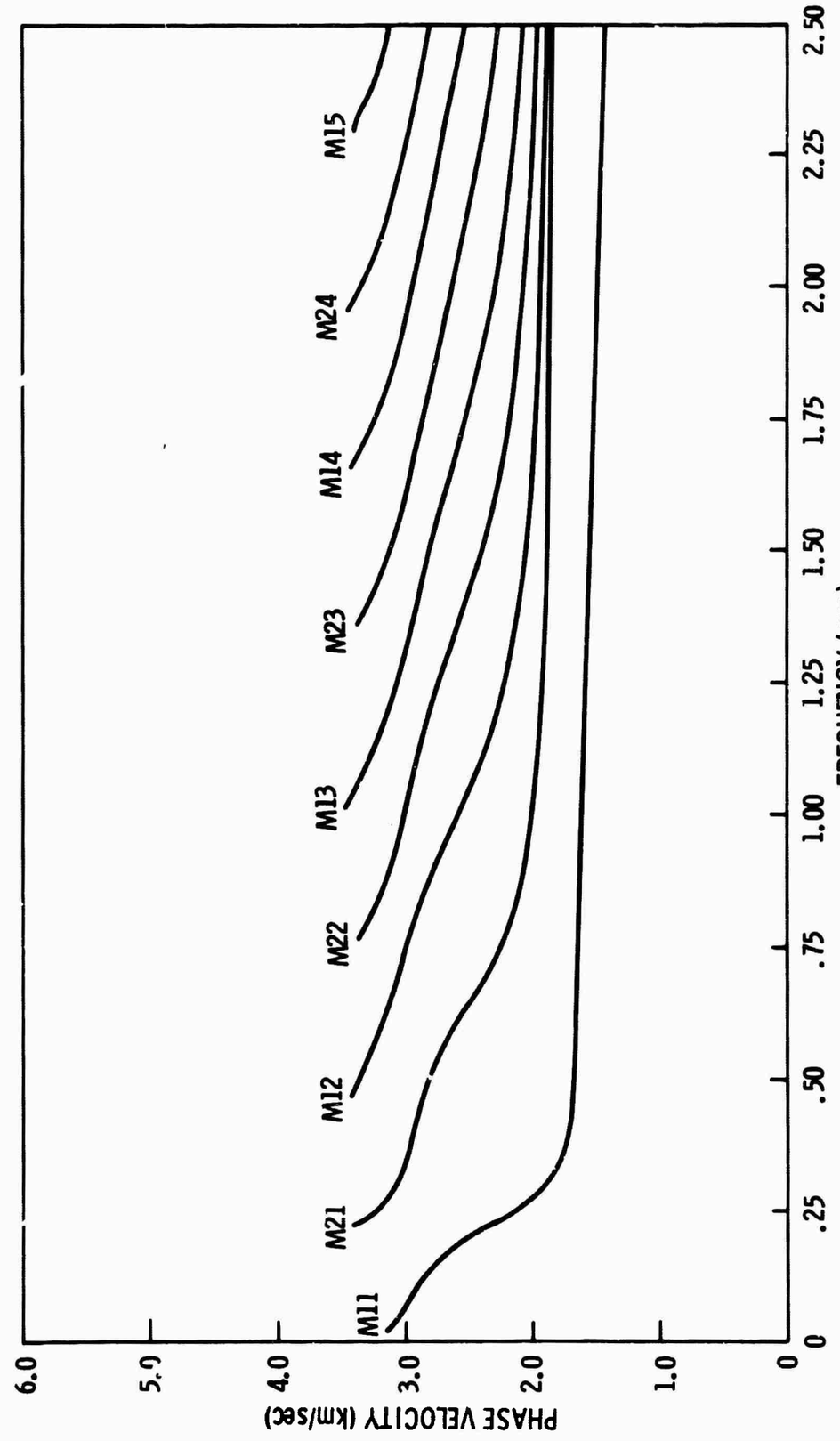

Figure II-41. Phase Velocity vs Frequency for M_{11} through M_{15} at LASA

Normal mode excitation amplitudes are shown in Figures II-42 through II-45. There is an unusual rise in M_{11} excitation amplitude above 1.5 cps. This mode's power across almost the entire frequency band insures its dominance in any field measurements.

The horizontal amplitude exceeds the vertical amplitudes for the first four modes near their cutoff frequencies. This atypical result is especially noticable for the two modes M_{12} and M_{22}.

Calculations for the LASA crust are proceeding, and an attempt to design mode separation filters and apply them to high frequency LASA data is planned.

3. Short-Period LASA Events

LASA field recordings of two events have been obtained from the Seismic Data Laboratory. Figure II-40 shows the configuration of the 21 subarrays in Montana. Each subarray consists of 25 short-period vertical Hall-Sears seismometers.

One event has been demultiplexed into subarrays and copied onto TIAC. Variable-area seismograms from three of the subarrays are shown in Figure II-46. Table II-12 describes associated PDE information for this event, which is approximately 700 km epicentral distance from LASA.

Table II-12

ASSOCIATED PDE INFORMATION
FOR COLORADO EVENT

Location	Colorado
Date	5 January 1966
Origin Time	00:37:17.8
Latitude	39.8° N
Longitude	104.7° W
Magnitude	4.6
Depth	5 km

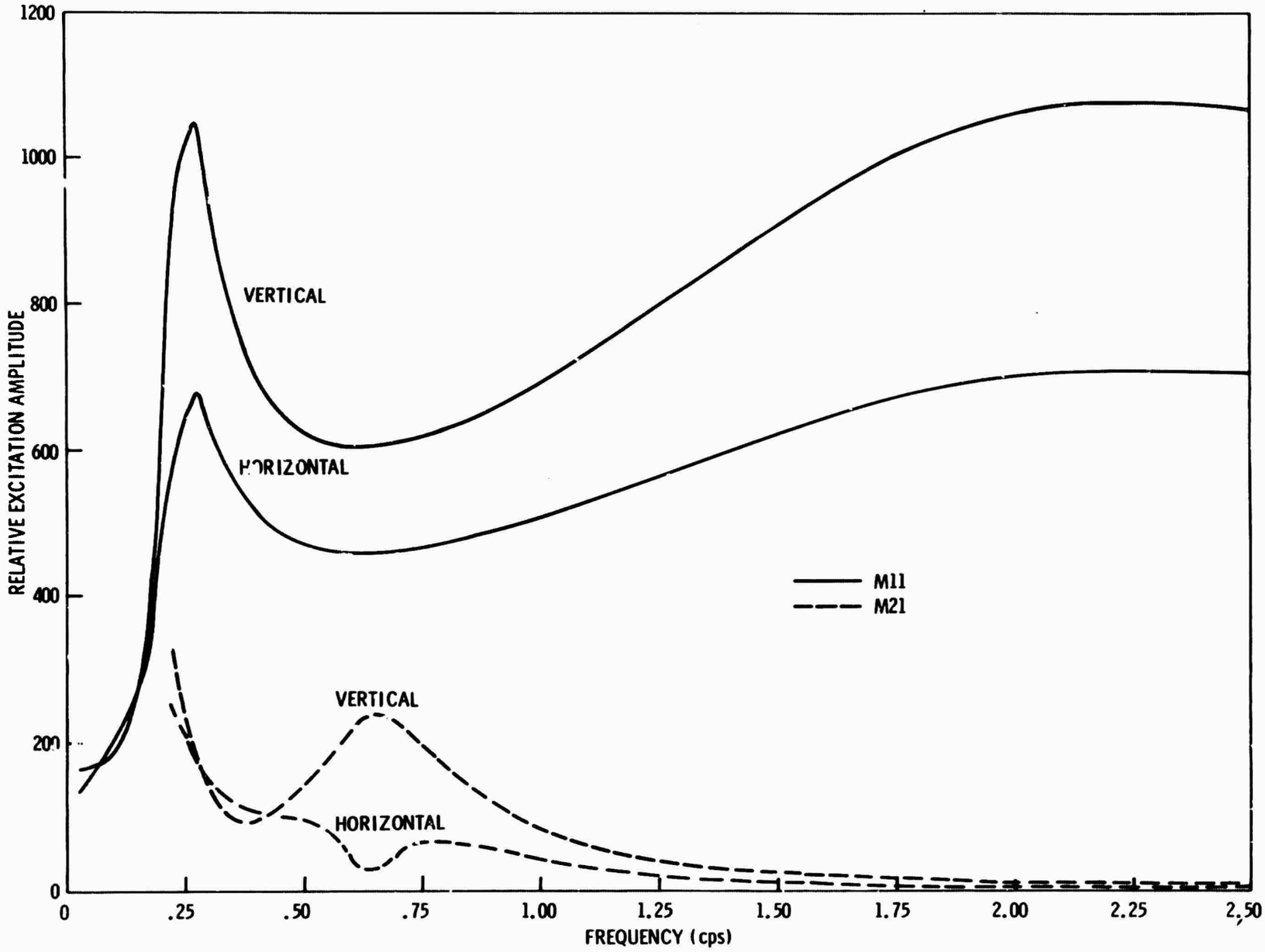

Figure II-42. Horizontal and Vertical Excitation Functions for Normal Modes M_{11} and M_{21} at LASA

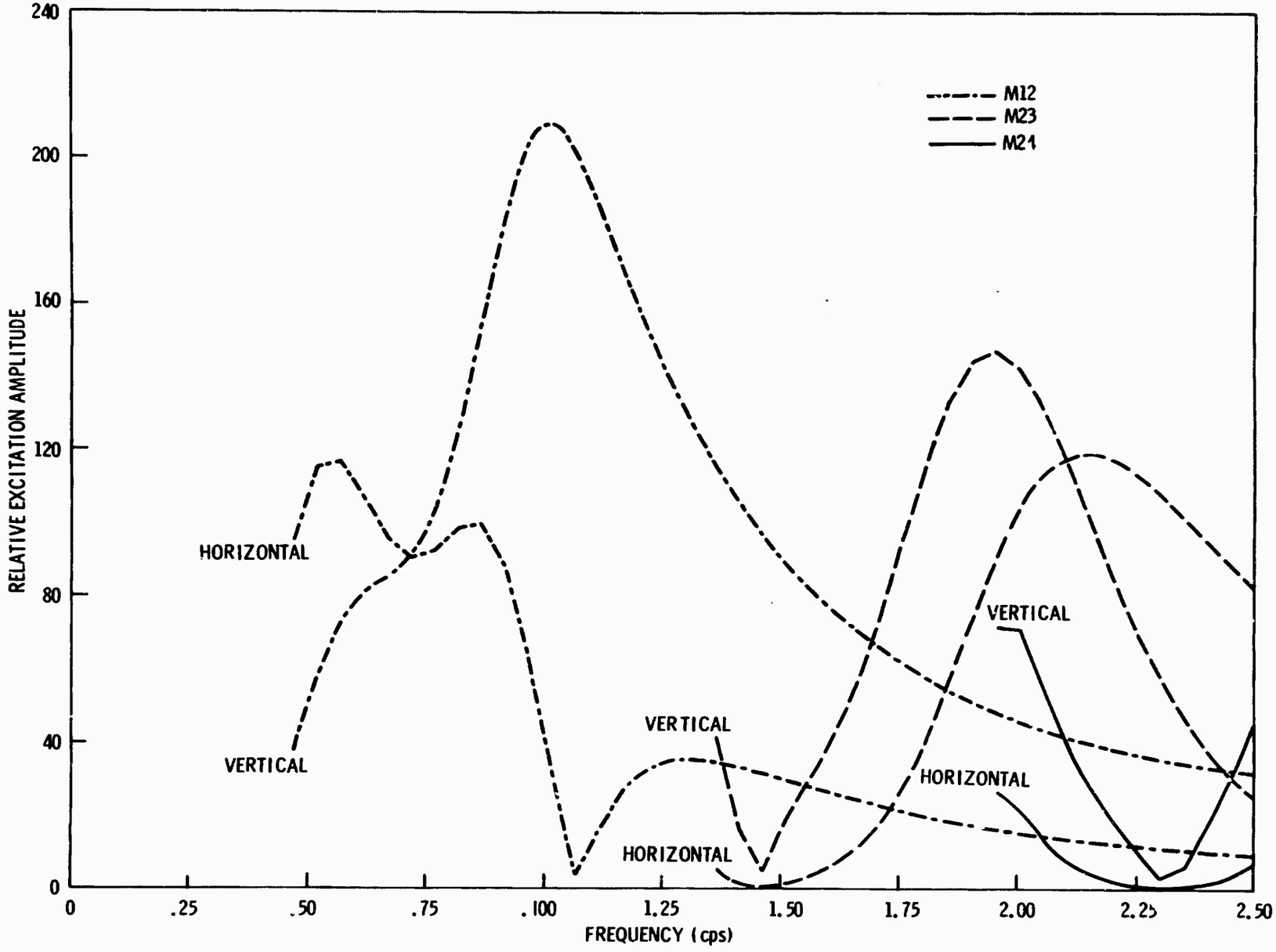

Figure II-43. Horizontal and Vertical Excitation Functions for Normal Modes M_{12}, M_{23} and M_{24} at LASA

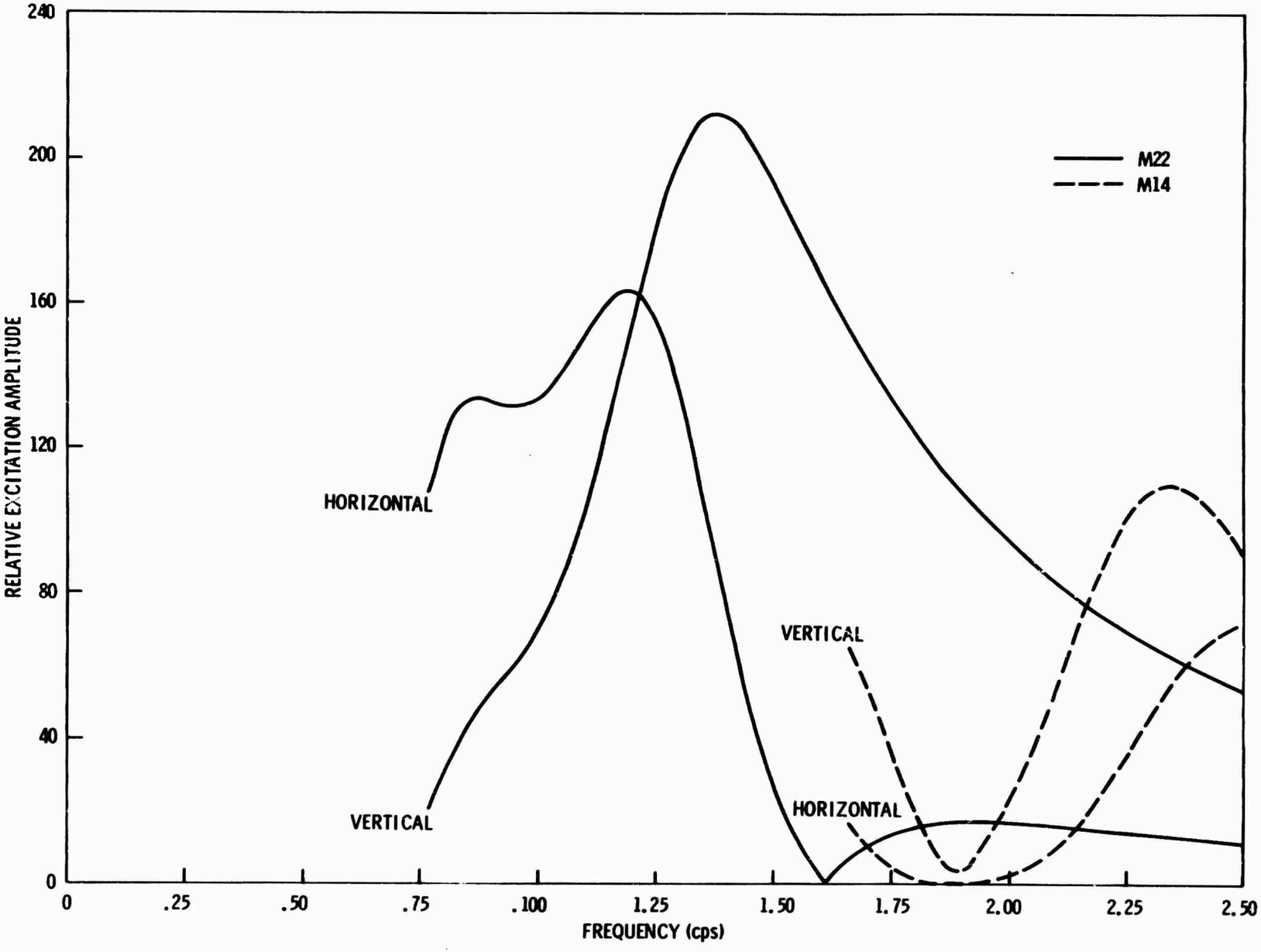

Figure II-44. Horizontal and Vertical Excitation Functions for Normal Modes M_{14} and M_{22} at LASA

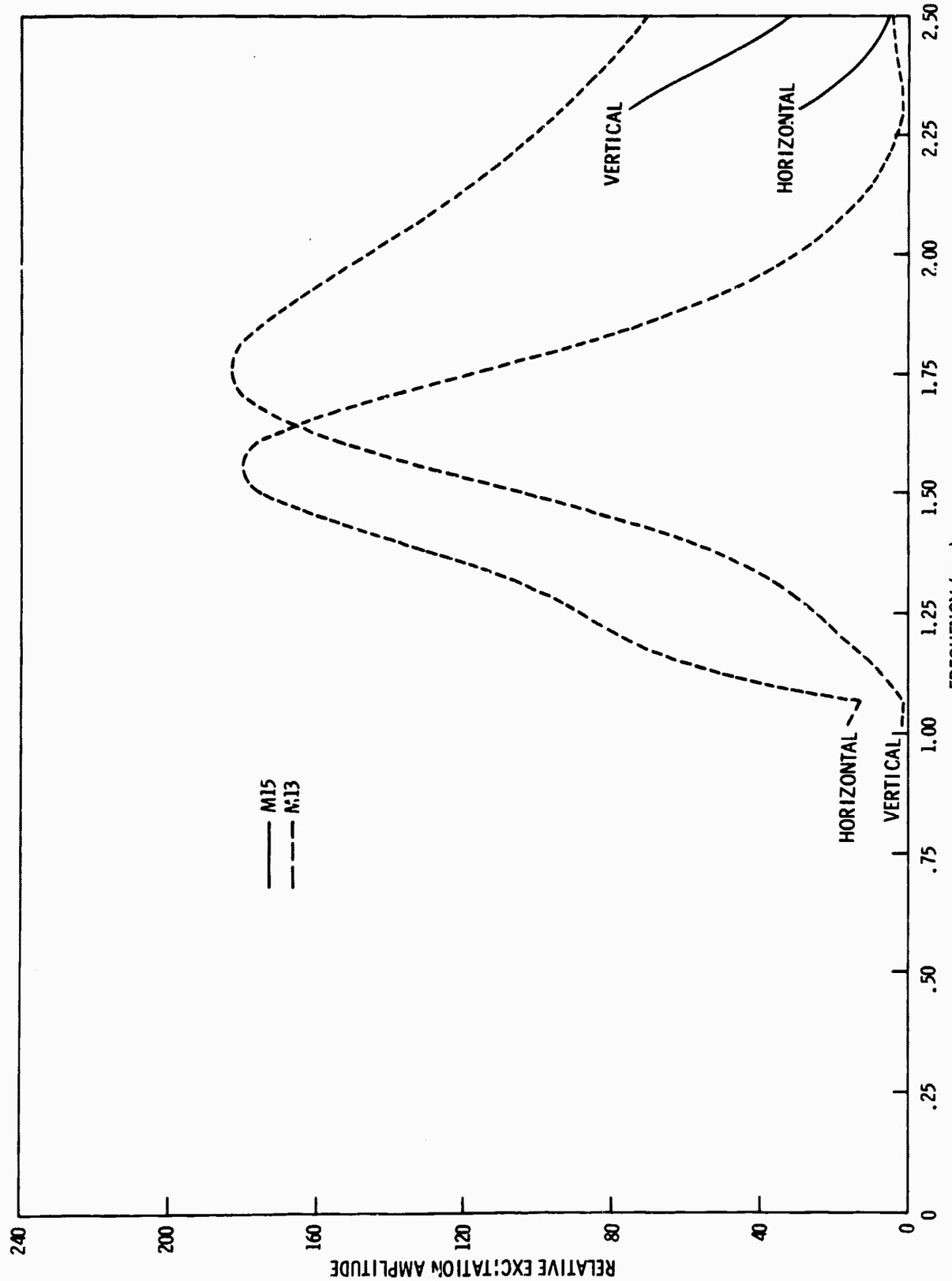

Figure II-45. Horizontal and Vertical Excitation Functions for Normal Modes M_{13} and M_{15} at LASA

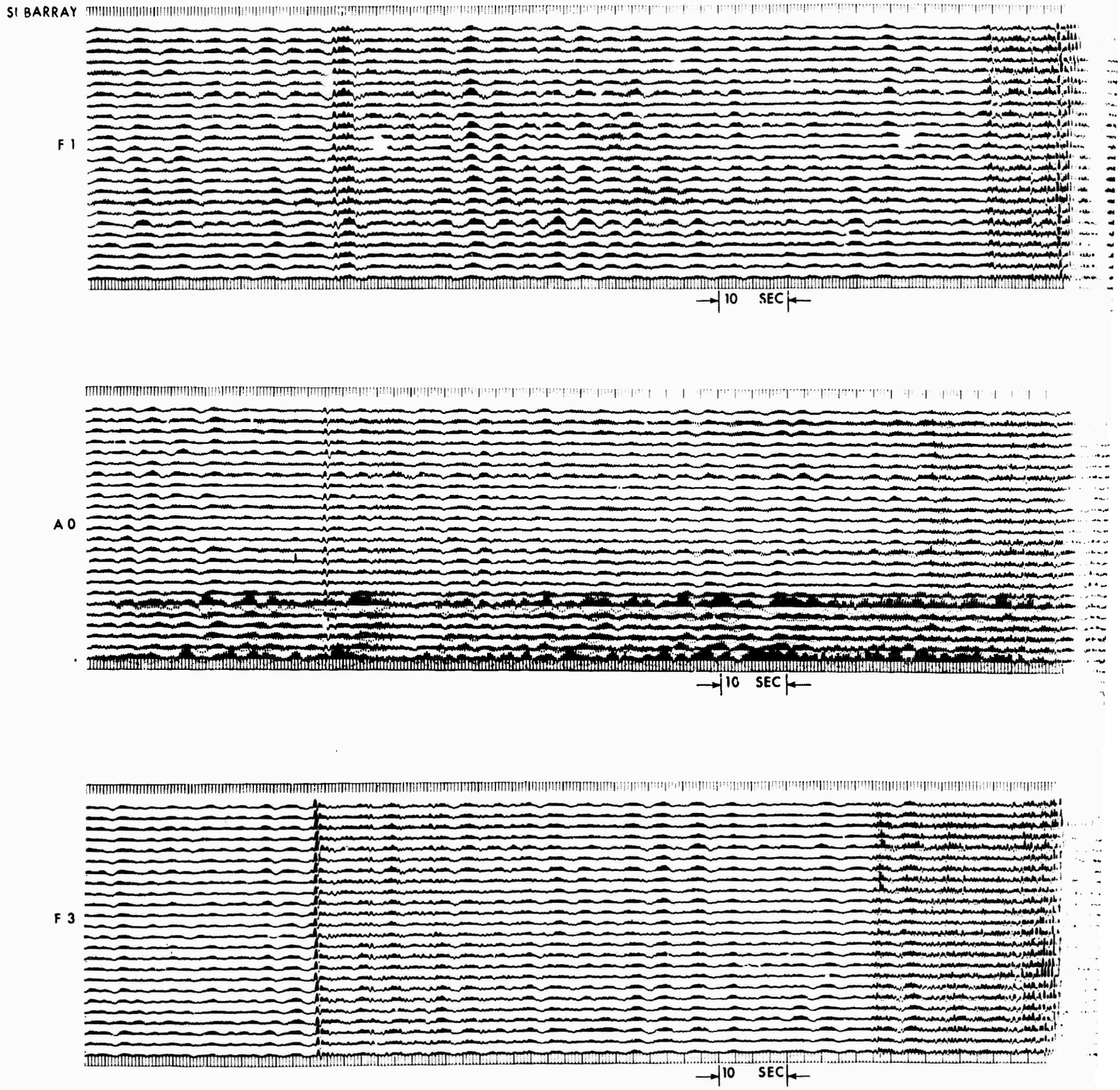

A

B

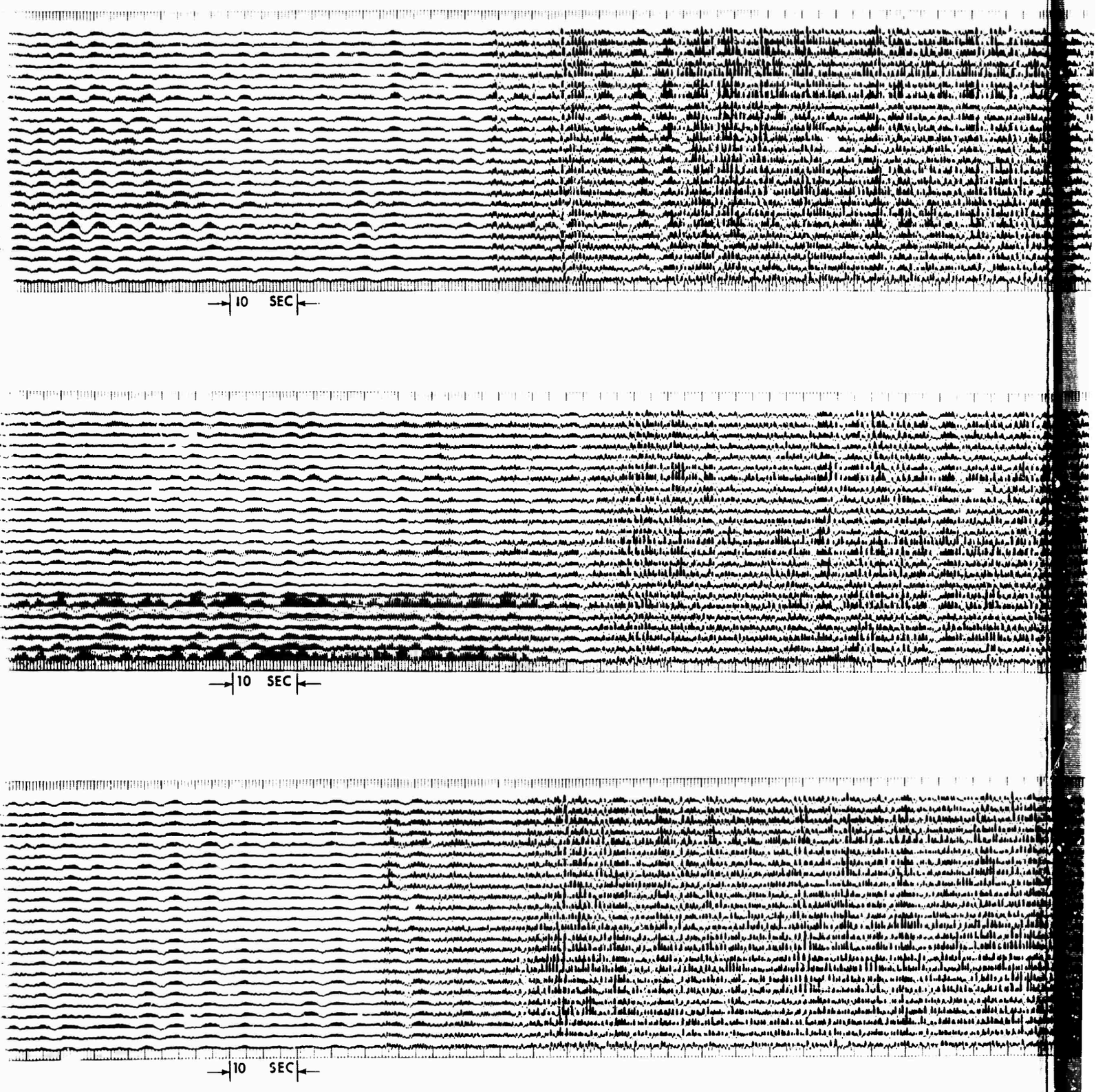

Figure II-46. Seismogram Record
LASA Subarrays

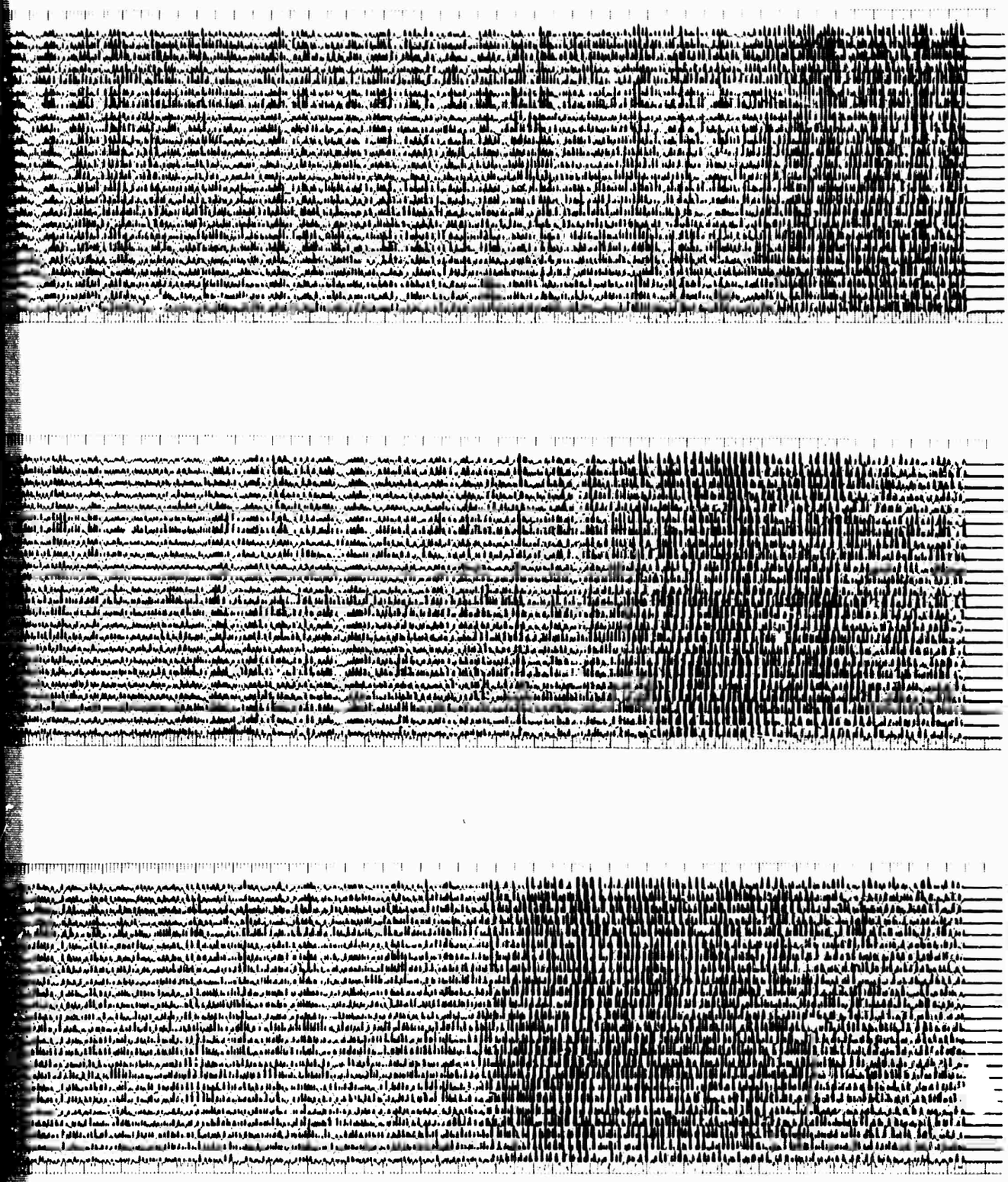

Figure II-46. Seismogram Recordings of the Colorado Event at Three LASA Subarrays

A preliminary examination of the LASA recordings shows a well defined P-wave of short duration, a shear mode region and the first part of the surface waves. The edit of the event at SDL was not sufficiently long in time to encompass the entire event. The signal energy lies primarily between 1.0 and 3.0 cps. Surface wave propagation in this frequency range will be controlled primarily by the upper 3 or 4 km of the crust at LASA. Therefore, information about the sedimentary layers can be obtained from these recordings by array processing.

Long period data which is currently being recorded at LASA will be obtained for mode separation processing as it becomes available.

SECTION III
SCATTERING STUDIES

A. DESCRIPTION OF ANALOG MODEL

An analog model, designated H-6, was used to perform scattering studies. This model consists of a single brass layer overlying a steel "half-space." The brass layer is 30 mm thick at one end and 50 mm thick at the opposite end. This change in thickness takes place over a horizontal distance of 60 mm. The brass and steel are 1/16 in. in width. A drawing of the model, along with its elastic parameters, is shown in Figure III-1. If one millimeter is scaled to one kilometer, the lateral inhomogeneity is representative of a transition from continental to oceanic crust.

A 400-kc barium titanate crystal, 1 mm in dia and glued to the surface of the model, serves as the source transducer. The receiving transducer (1 mm x 3 mm) is also a barium titanate crystal. Polarization of the transmitter is such that it operates in a compressional mode, while the receiver responds in a transverse mode. A square pulse of about 3-μsec duration and 1000-volts amplitude is applied across the source crystal. The receiver may be rotated 90° in order to measure horizontal and vertical components of lateral motion. The signals are passed through amplifiers, filters and a voltage-to-frequency converter and then digitized. The output is punched on paper tape for computer processing.

B. SCATTERING DUE TO LATERAL INHOMOGENEITY

With the source located on the thin end of the model (Figure III-1), recordings were made at 1-cm intervals along the surface of the model. High and low gain recordings of horizontal and vertical amplitudes

		BRASS	STEEL
P	velocity	3.91 mm/μ sec	5.24 mm/μ sec
S	velocity	2.09 mm/μ sec	3.10 mm/μ sec
R	velocity	1.97 mm/μ sec	2.97 mm/μ sec

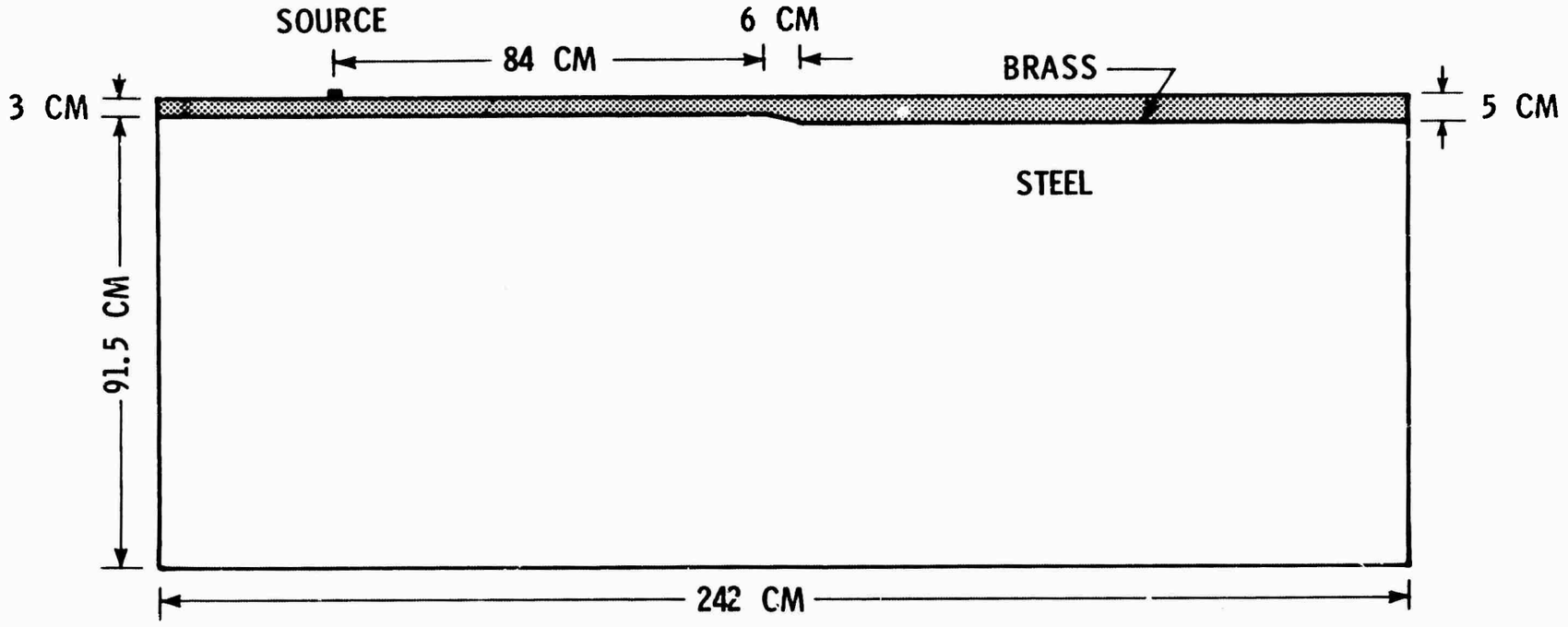

Figure III-1. Diagram of Model H-6

were made to insure optimum recognition of the weak as well as the strong signatures. The low gain vertical and horizontal recordings are shown in Figures III-2 and III-3, respectively, while the high gain vertical and horizontal recordings are shown in Figures III-4 and III-5.

Travel-time curves, shown in Figure III-6, have been calculated for the case where the source is located on the surface at the thin (30 mm brass) end of the model. Measured values are plotted as small dots on the theoretical travel-time curves. They were obtained by timing the "first break" and secondary arrivals on the high-gain records. Even though the wavelengths of the first arrival are of the order of the layer thickness and thus lend themselves to a modal interpretation, there is good agreement between the ray theory predictions and experiment (Figure III-6).

An inspection of the recordings from Model H-6 (Figure III-4) shows a well developed leaking mode propagating in the thin end. In order to identify the mode, two independent sets of input traces were Pie Slice* processed to pass only the high velocity leaking mode energy propagating between 4.0 and 6.7 mm/μsec and to reject energy propagating at velocities outside this band. A single-channel spatial prediction filter was then computed from auto- and crosscorrelations of the Pie Sliced output traces, and dispersion was determined from the phase of the prediction filter. The dispersion estimates agree with the theoretical curves for PL_{22} propagating in the thin end of the model. Power spectra show the energy to be highly peaked around 70 kc.

Since mode conversion is expected to occur in going from the thin to the thick end, a similar analysis was performed on the seismograms from the thick end. However, no consistent dispersion estimates could be obtained.

*A GSI Service Mark

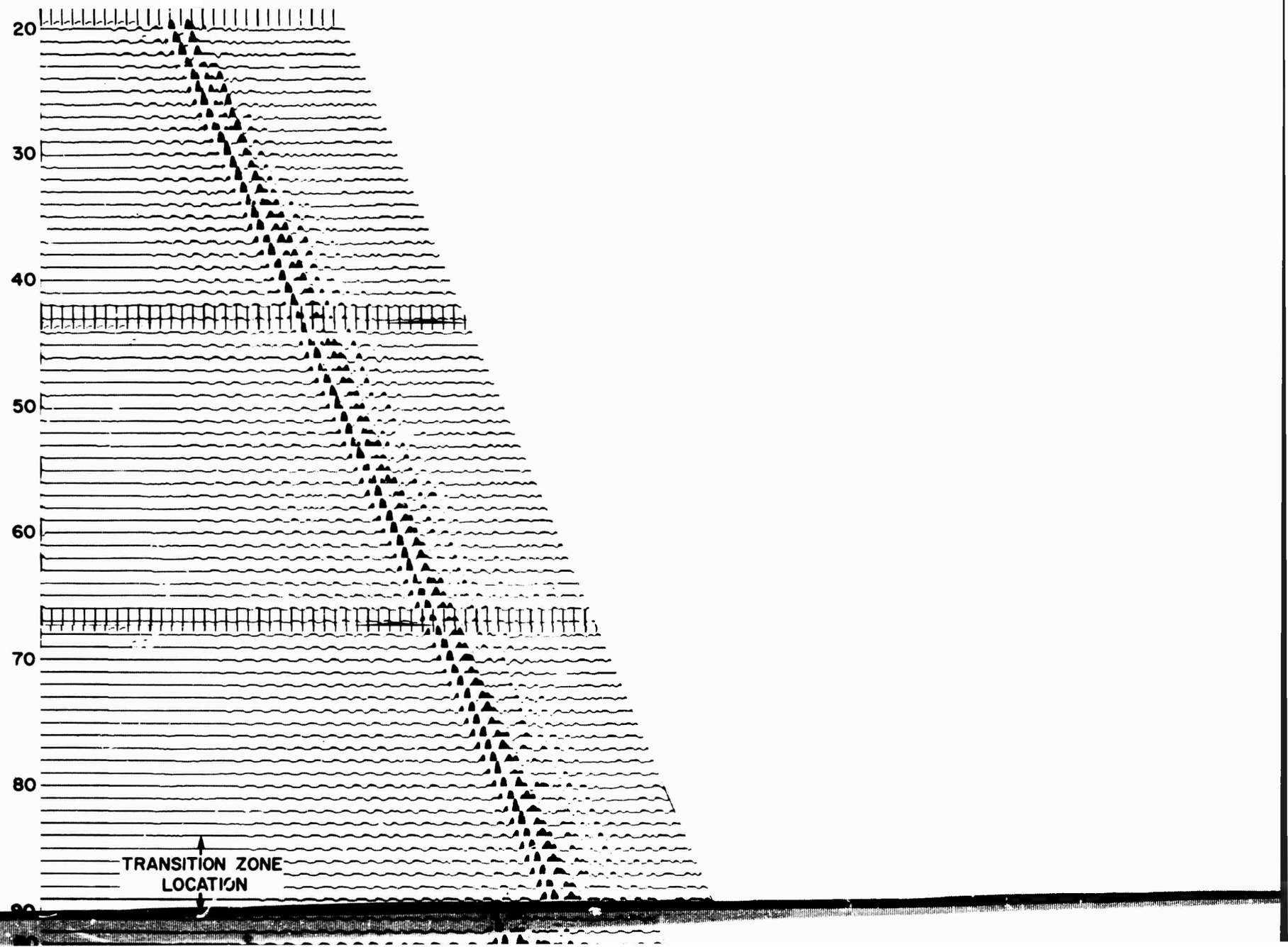
20
30
40
50
60
70
80
TRANSITION ZONE
LOCATION

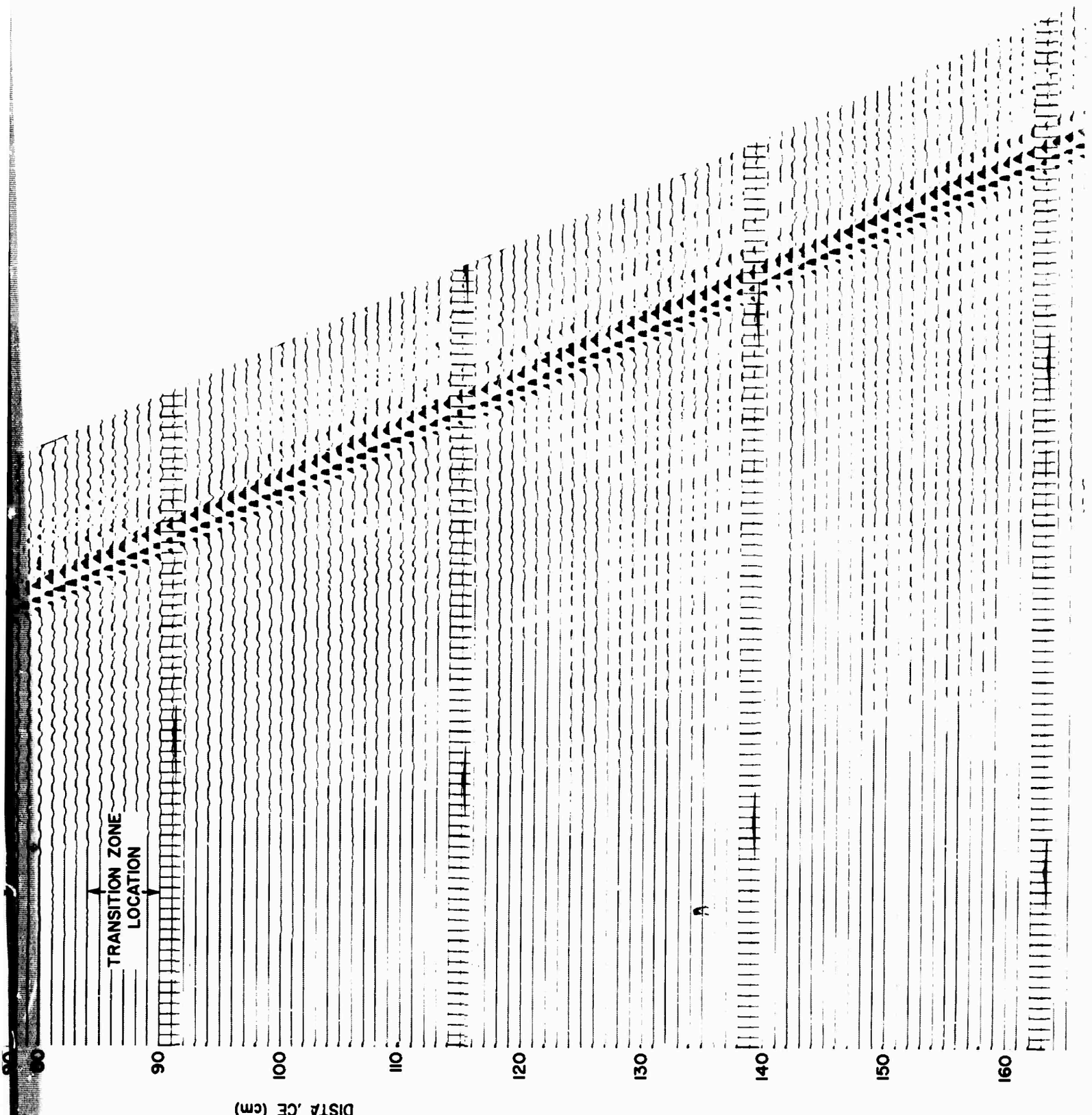

Figure III-2. Low-Gain Vertical Recordings Obtained
Model H-6 with the Source Locate

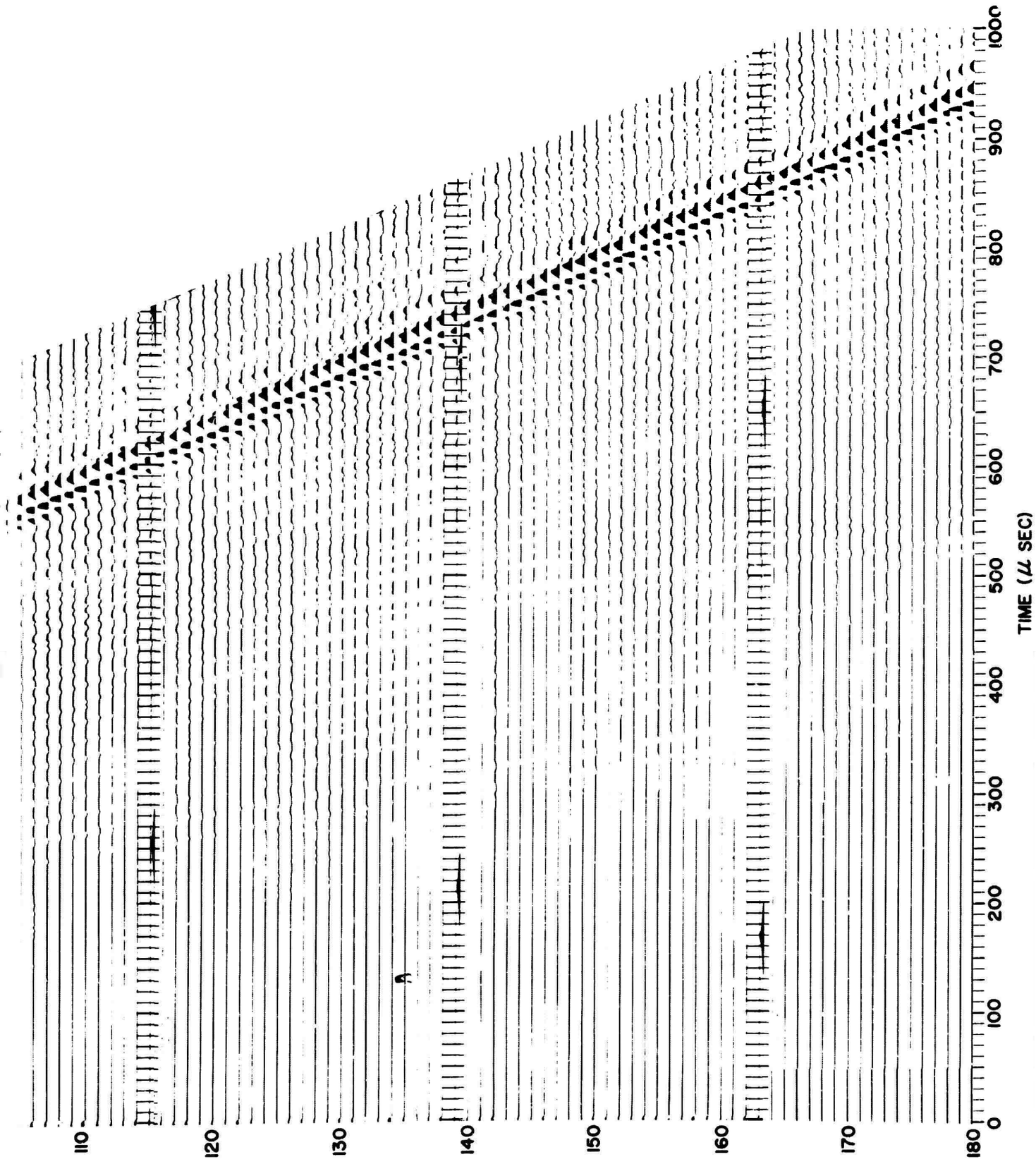

Figure III-2. Low-Gain Vertical Recordings Obtained from Model H-6 with the Source Located on the Thin End

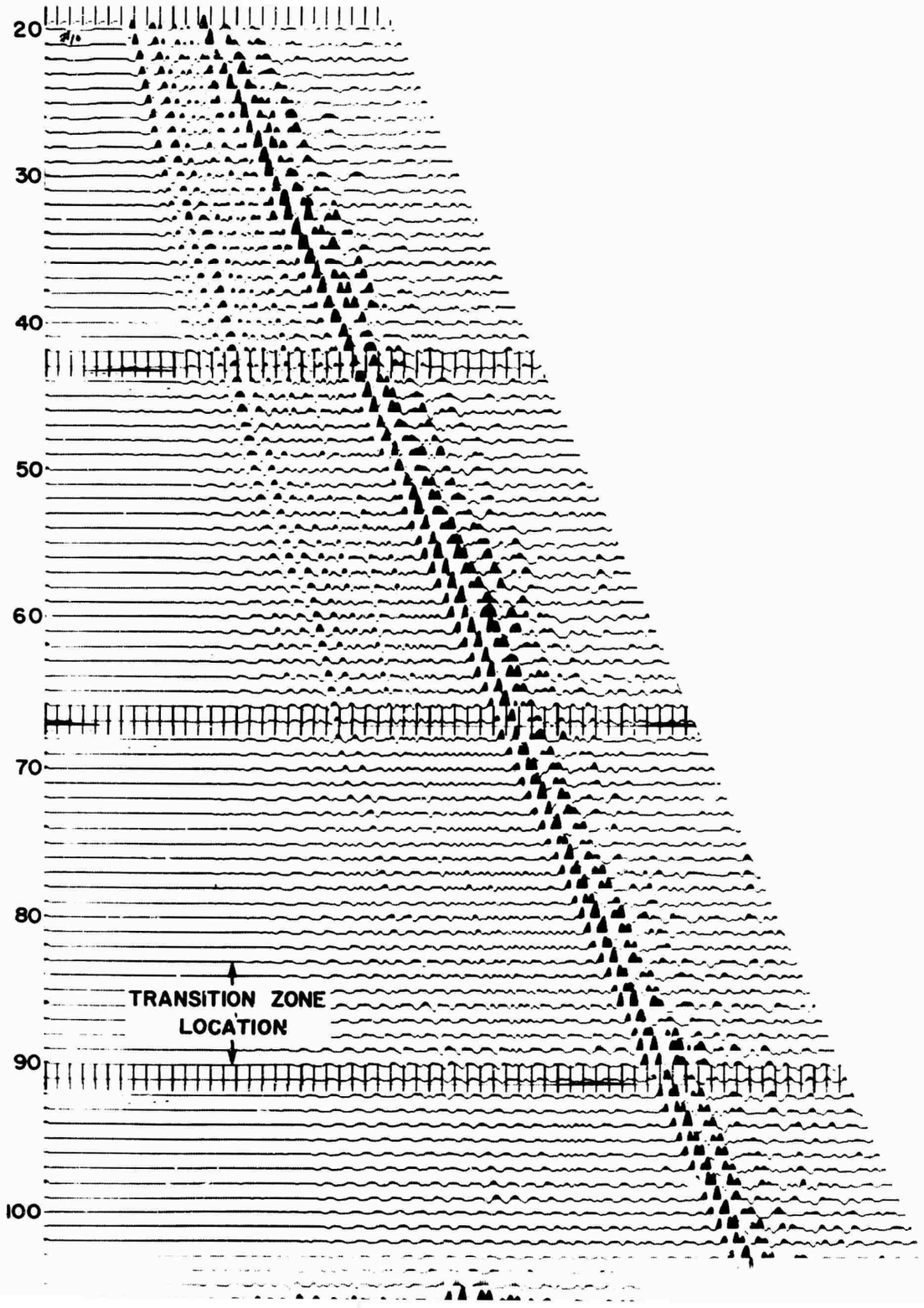
20
30
40
50
60
70
80
TRANSITION ZONE
LOCATION
90
100

Figure III-3. Low-Gain Horizontal Rec
with the Source Located o

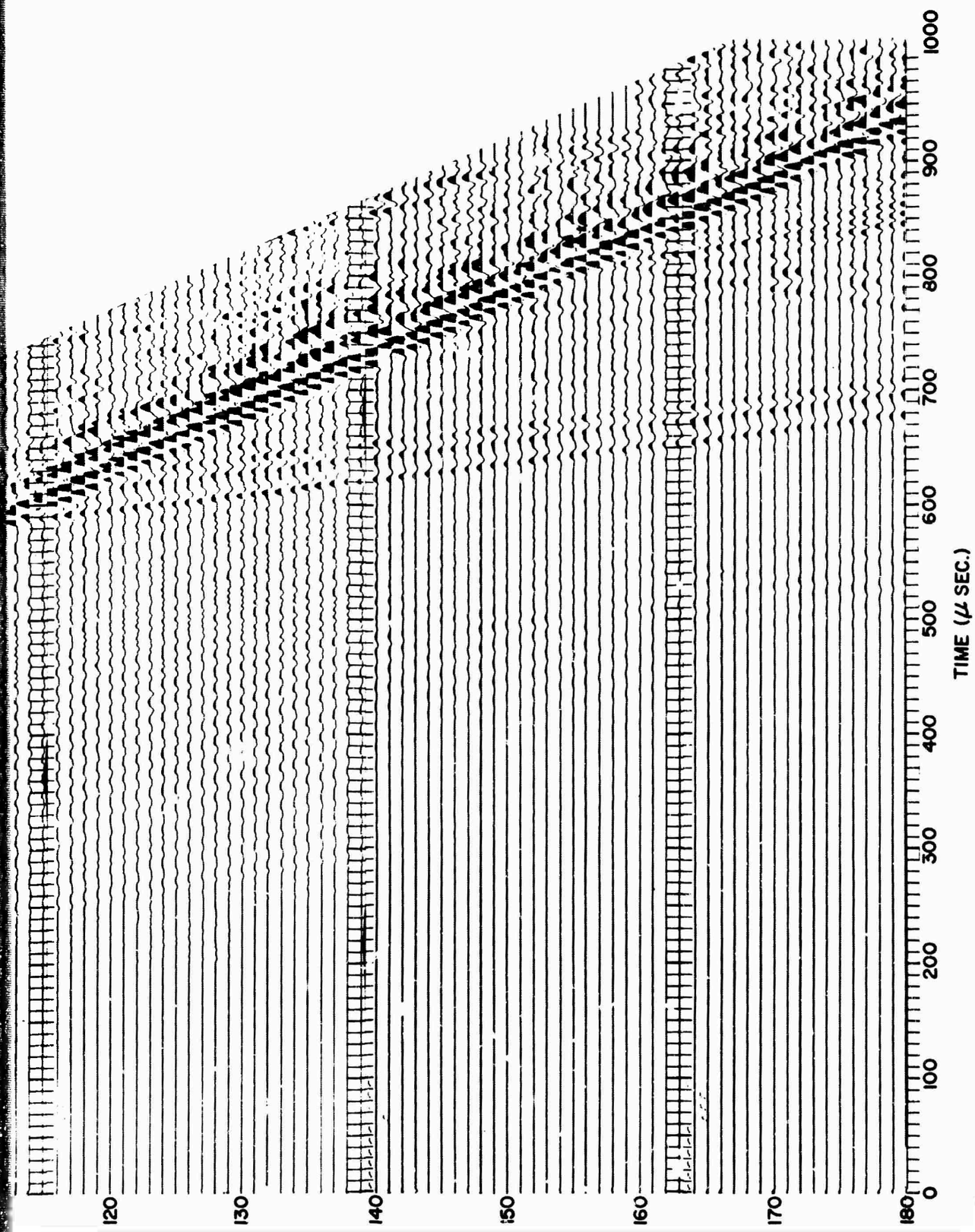

Figure III-3. Low-Gain Horizontal Recordings Obtained from Model H-6 with the Source Located on the Thin End

A

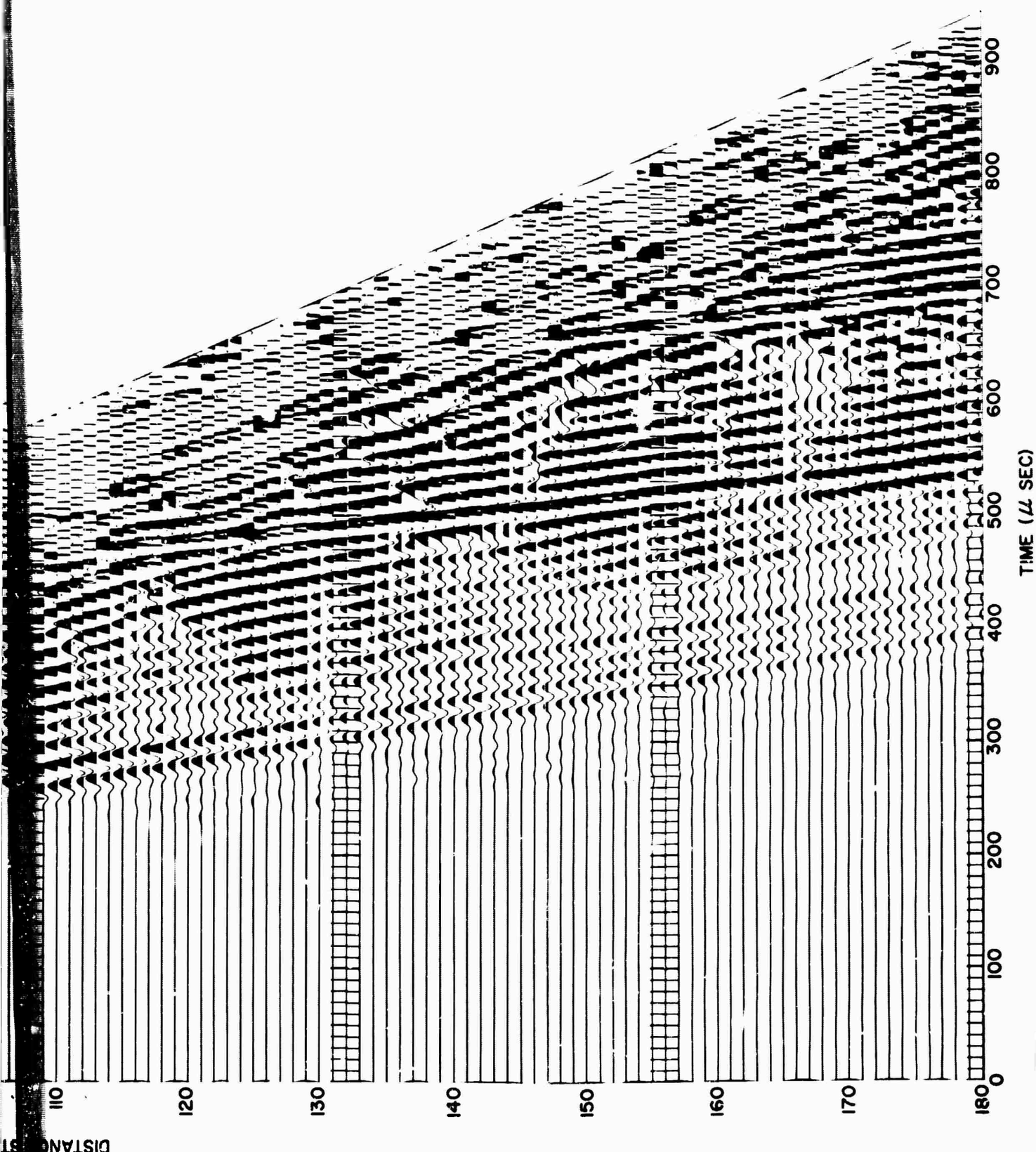

Figure III-4. High-Gain Vertical Recordings Obtained from Model H-6 with the Source Located on the Thin End

TRANSITION ZONE
LOCATION
40
50
60
70
80
90
100
110
STANCE (cm)

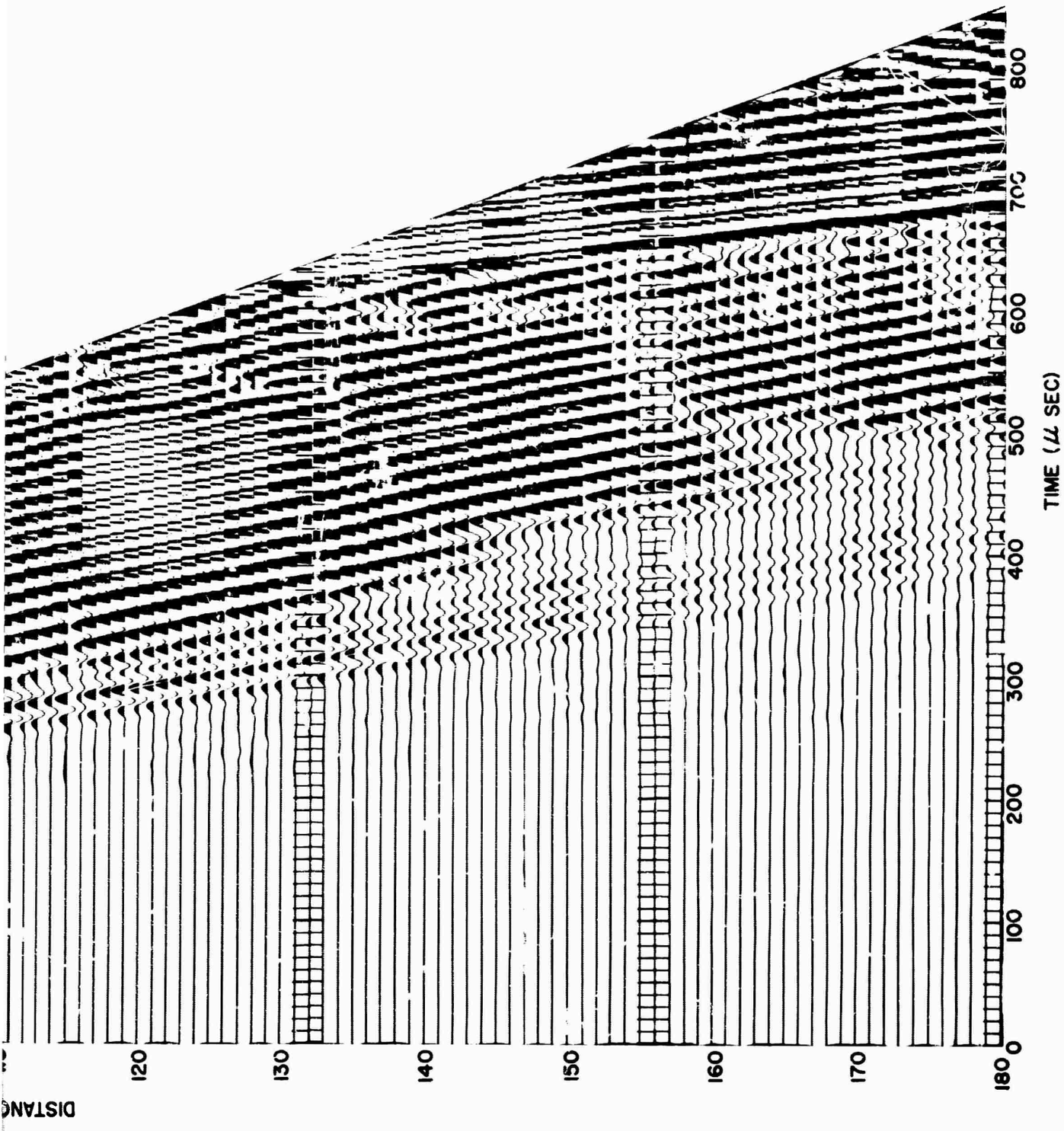

Figure III-5. High-Gain Horizontal Recordings Obtained from Model H-6 with the Source Located on the Thin End

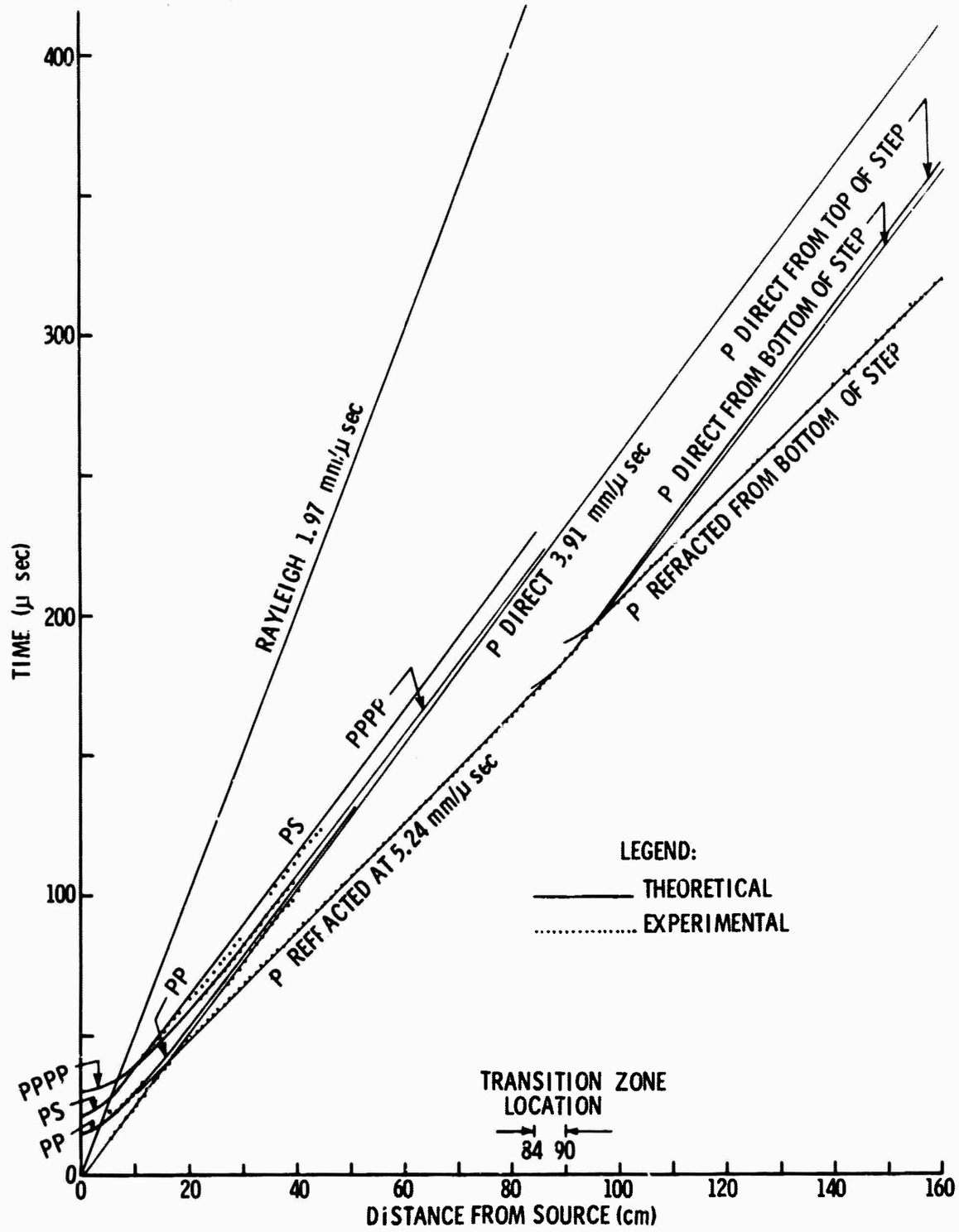

Figure III-6. Travel Time Curves for Model H-6

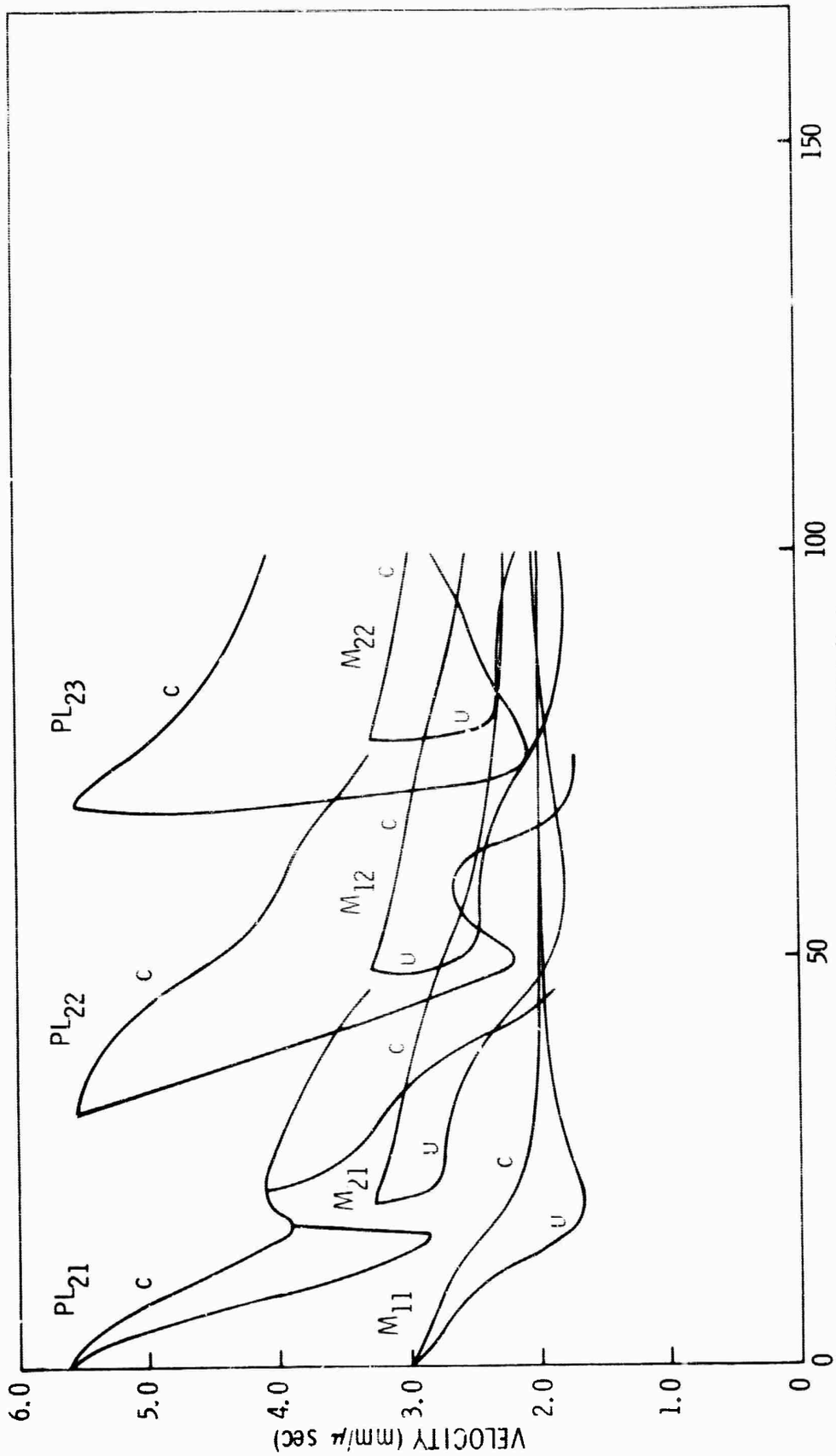

Figure III-7. Dispersion Curves for the Dominant Normal and Leaky Modes for Model H-6 (Thick End)

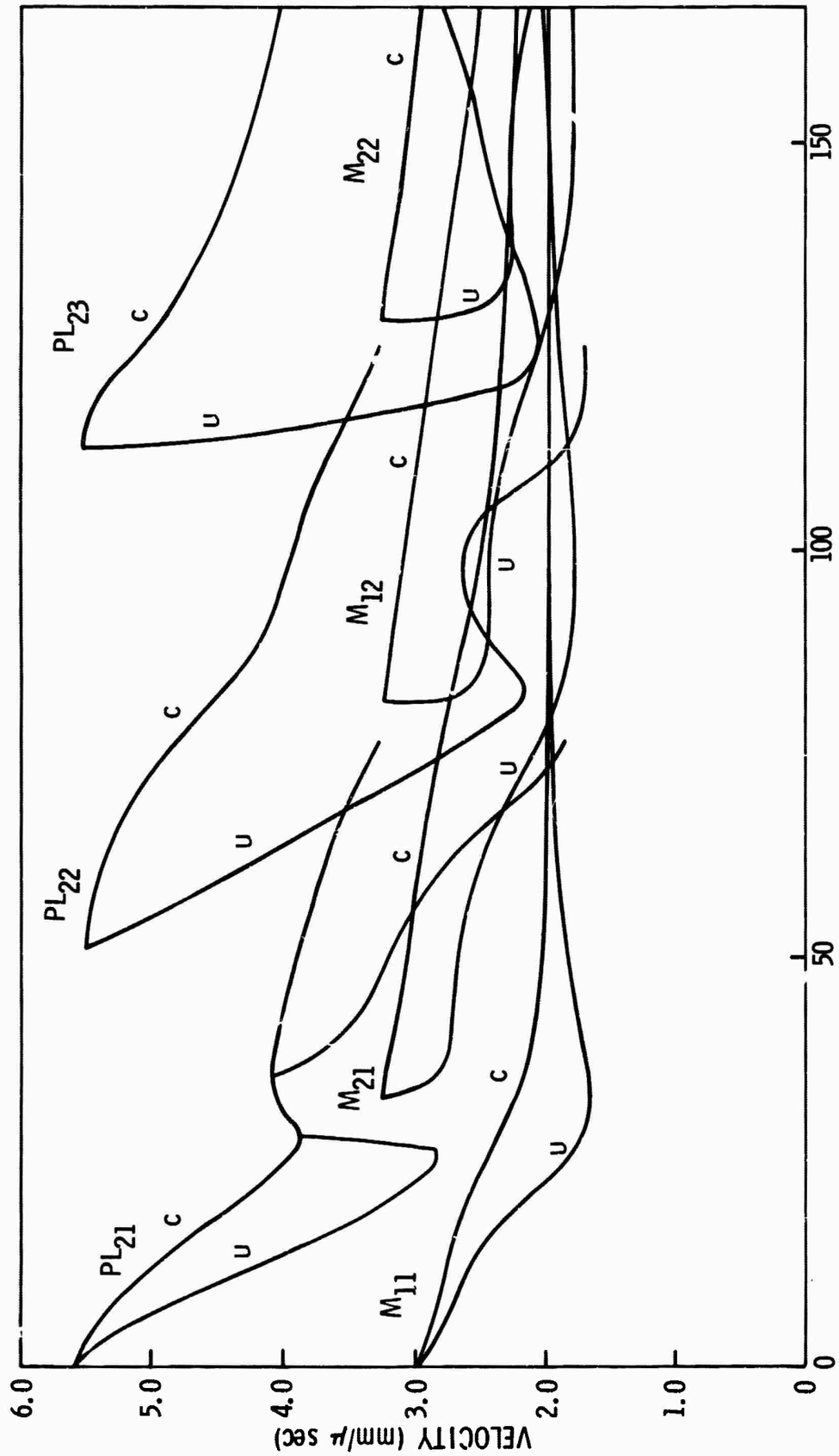

Figure III-8. Dispersion Curves for the Dominant Normal and Leaky Modes for Model H-6 (Thin End)

theoretical dispersion curves (Figures III-7 and III-8) show that if M_{21} on the thin end scattered into M_{21} on the thick end, a decrease in phase velocity at each corresponding frequency would result. Frequency-wavenumber analysis was used in an attempt to measure this velocity change.

Nineteen traces from the thin end of the model were used to obtain correlations which were double Fourier transformed to give the f-k spectra shown in Figure III-9.[8] The theoretical dispersion characteristics for M_{11} and M_{21} on the thin end are shown on the plot as solid lines. The Rayleigh mode is the dominant event on the recordings, and its dispersion characteristic is well defined in the f-k plot. The 6- to 12-db contour at 60 kc and 0.2 wavenumber is probably a manifestation of M_{21}. The theoretical and experimental curves should not agree exactly, since the velocities used to compute the theoretical curves differ slightly from the actual model velocities.

Next, the f-k spectra shown in Figure III-10 were computed using 19 traces from the thick end of the model. As before, the Rayleigh mode characteristic is well defined. The theoretical dispersion characteristics for M_{21} and M_{12} on the thick end are shown on the plot as solid lines. One obvious difference between the two f-k spectra is the more complicated appearance of the spectra for the thick end. The 6- to 12-db contour at 60 kc and 0.2 wavenumber, which was observed on the thin end, has changed appreciably in location. There now are two 6- to 12-db contours present at 60 kc, and they agree well with M_{21} and M_{12} characteristics for the thick end.

These results are consistent with mode-to-mode scattering. However, it is known that crosscorrelation between modes complicates

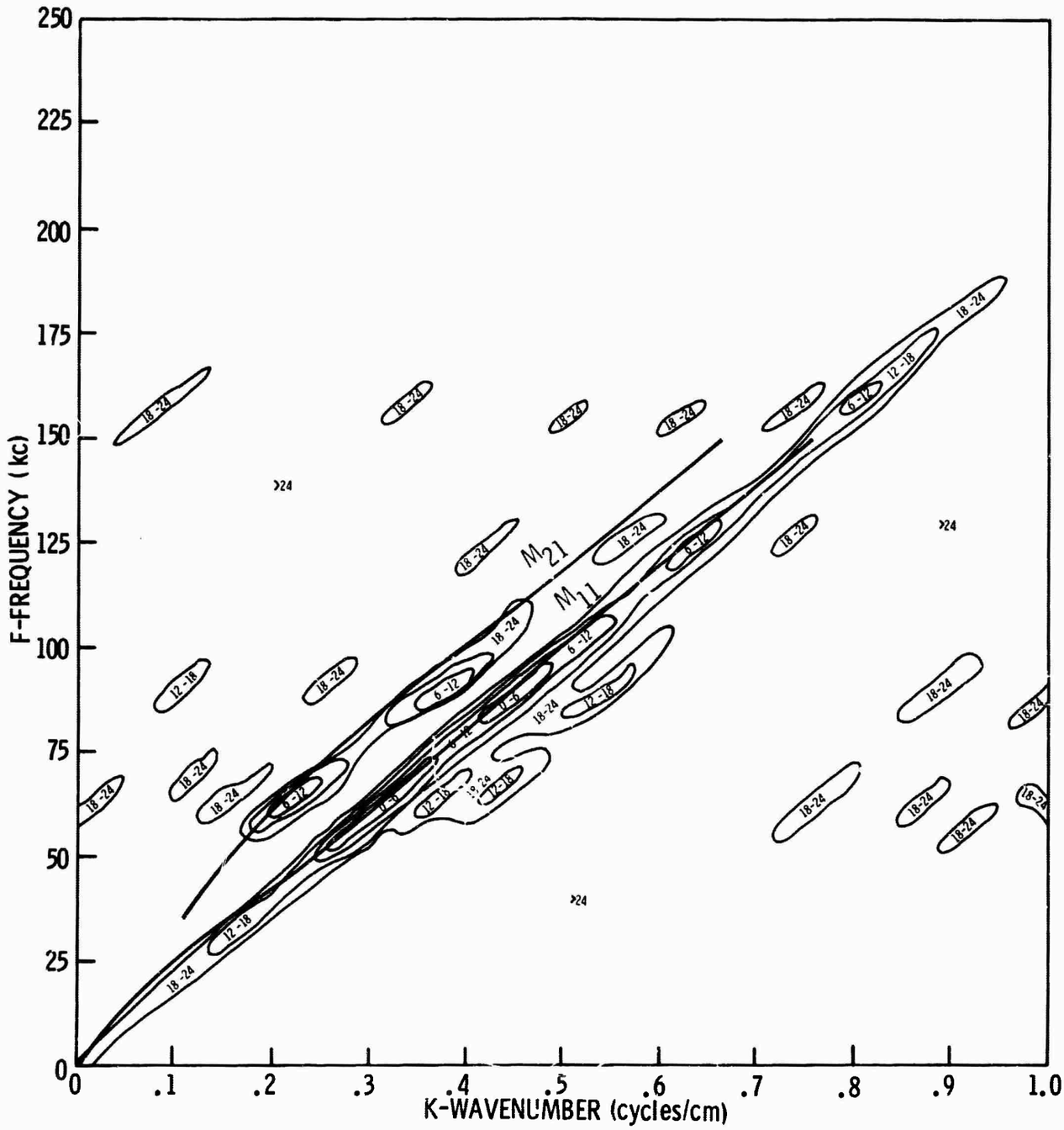

Figure III-9. Spectral Estimate of Model H-6 Data Using a 19-Element Array on the Thin End of the Model

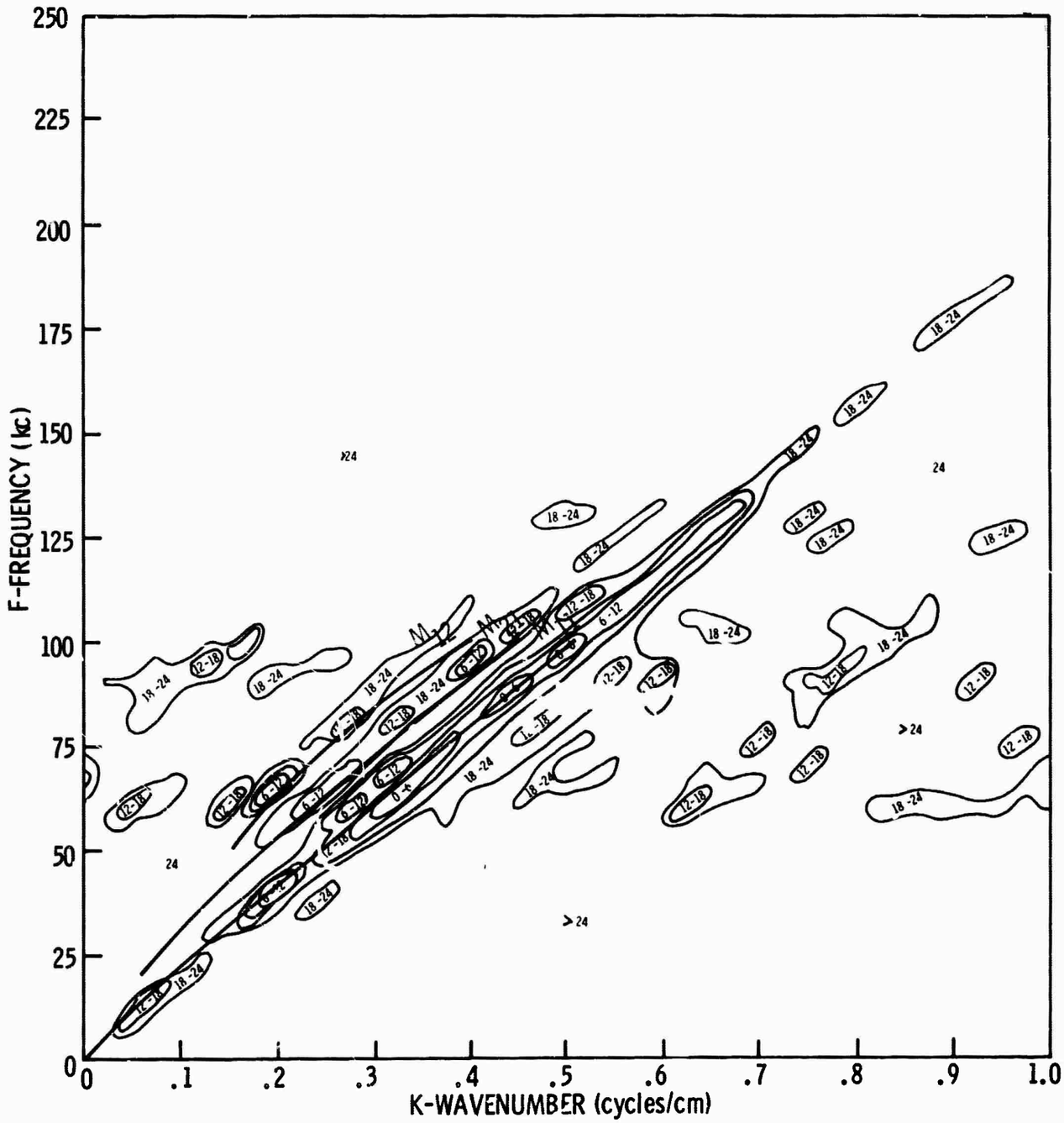

Figure III-10. Spectral Estimate of Model H-6 Data Using a 19-Element Array on the Thick End of the Model

the fine structure of the frequency-wavenumber estimate (particularly when one mode, such as the Rayleigh, is 12 to 18 db stronger than the next higher mode). Therefore, if accurate dispersion characteristics are to be measured, mode separation processors must be designed and applied.

C. SCATTERING FROM SMALL SURFACE IRREGULARITIES

In order to simulate the effect of incident seismic waves interacting with a small surface irregularity, brass scatterers were glued to the surface of the analog model. One of the scatterers was triangular shaped with a base length of 10 mm and a height of 3 mm. The other one had approximately the same dimensions but was Gaussian shaped. Figure III-11 shows a side view of these two scatterers. Henceforth, they will be referred to as scatterer 1 and 2, respectively.

(A)
SCATTERER 1

(B)
SCATTERER 2

Figure III-11. Surface Scatterers

Each scatterer was centered on the surface of the thin end of Model H-6, 40 cm from the source (Figure III-12). In effect, the analog model was a single layer over a half-space with a surface irregularity. Using this arrangement, the receiver was moved along the surface, and recordings were made at 1-cm intervals at a distance from the source which ranged from 10 to 59 cm.

The vertical output traces of the received signal using no surface scatterers are shown in Figure III-13. The dominate feature of these traces is the incident Rayleigh mode.

Figure III-14 shows recordings over the same profile when scatterer 1 is in position. A pulse reflected from the scattering center is observed propagating back toward the source at Rayleigh velocity (1.97 mm/μsec). Recordings with scatterer 2 in place are shown in Figure III-15. A similar reflected pulse is observed.

The traces were Pie Sliced[9] for a velocity of -2.0 mm/μsec to pass the reflected pulse only. The Pie Slice output distances were 15.5, 24.5, 33.5, 46.5 and 53.5 cm from the source. These results are shown in Figures III-16 and III-17, respectively. Similarly, the traces were Pie Sliced at 2.0 mm/μsec in order to pass the incident Rayleigh wave.

Power spectra of the +2.0 mm/μsec Pie Sliced output (incident Rayleigh) and the -2.0 mm/μsec Pie Sliced output (reflected Rayleigh) were calculated for distances of 15.5, 24.5 and 33.5 cm from the source. The two spectra at each of the above three distances are shown in Figures III-18, III-19 and III-20, respectively, for scatterer 1. The relatively low power level at low frequencies for the reflected wave observed

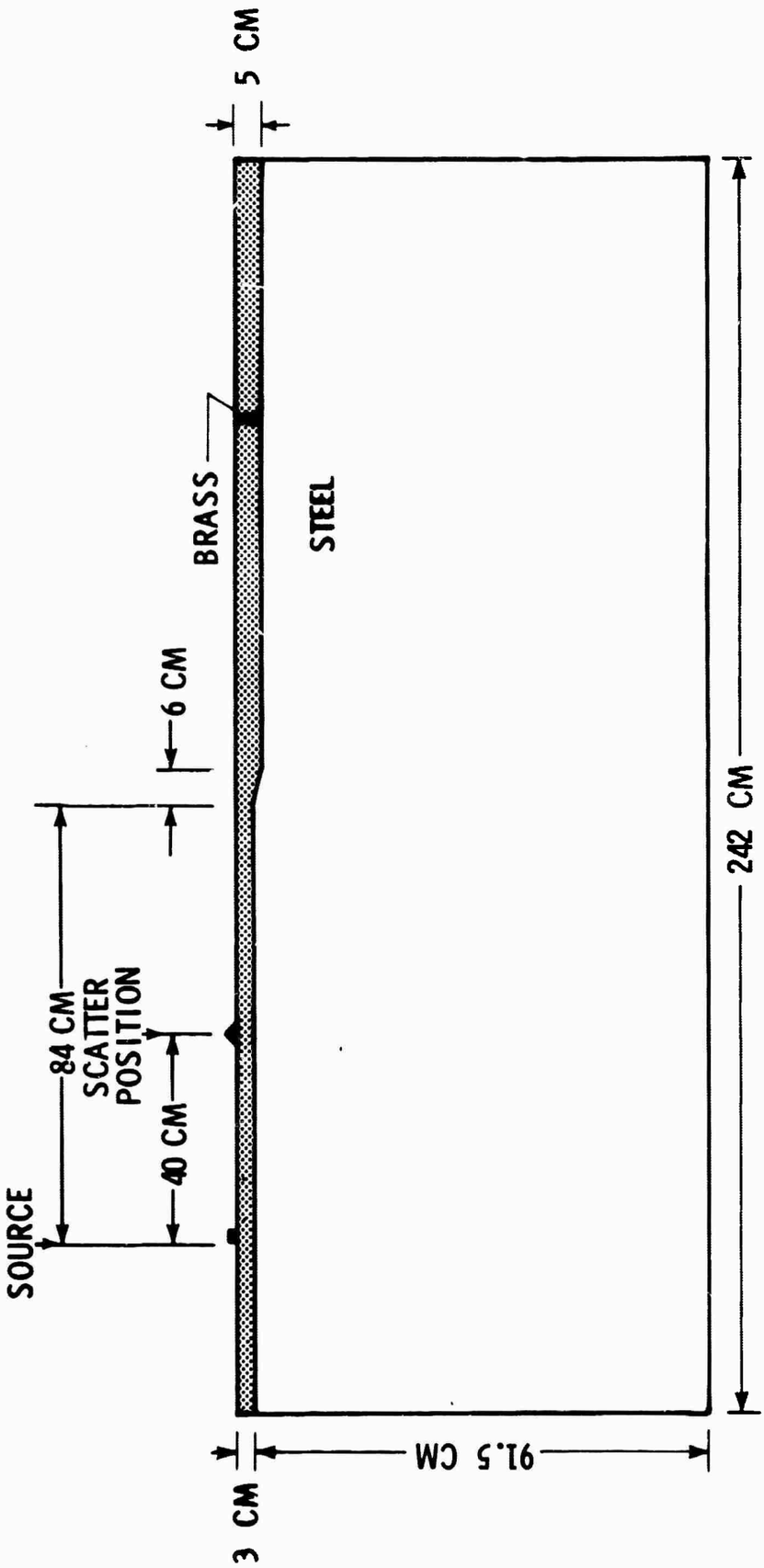

Figure III-12. Diagram of Model H-6 with Surface Scatterer

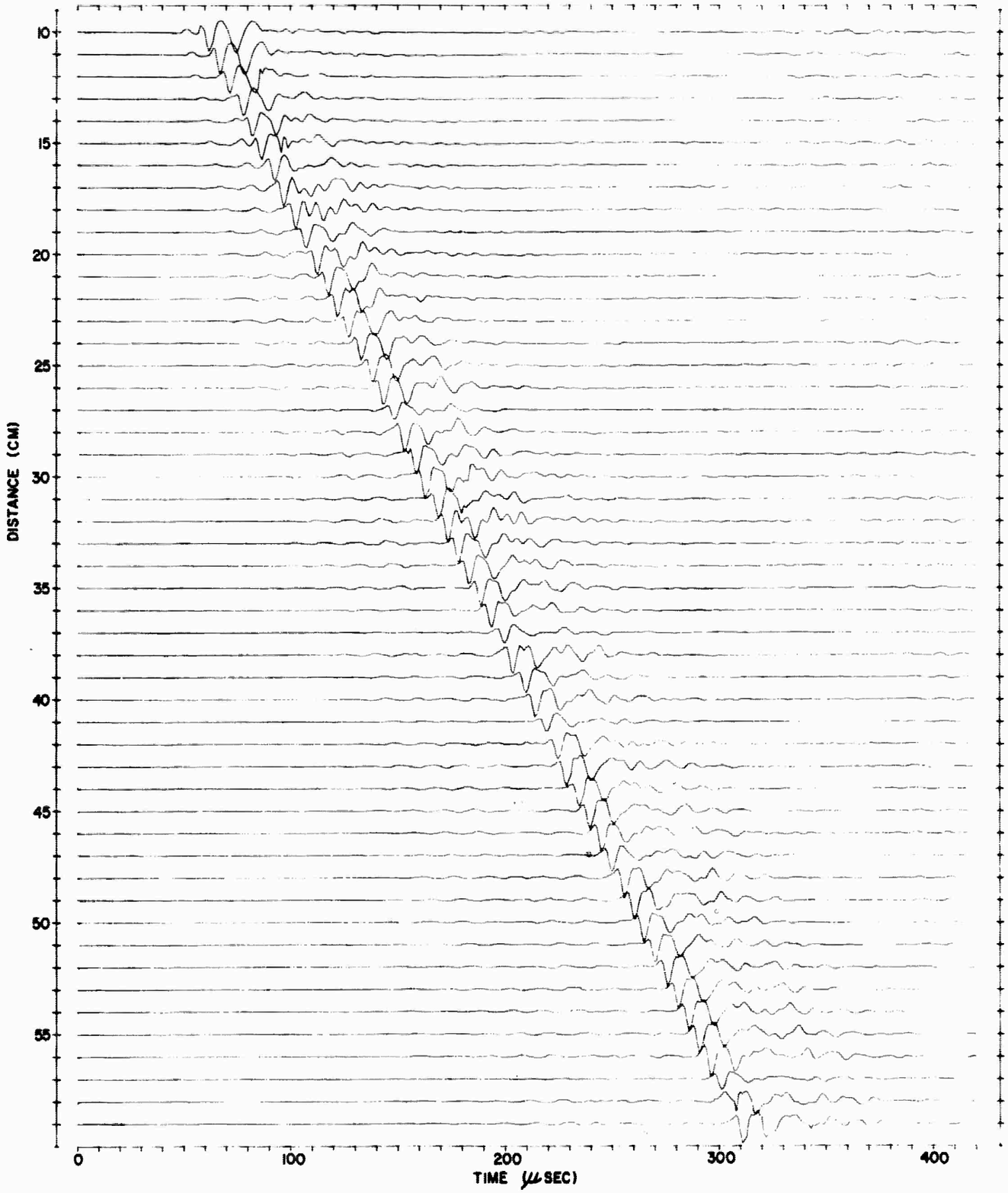

Figure III-13. Low Gain Vertical Recordings for Model H-6 (Distance from the source ranges from 10 to 59 cm)

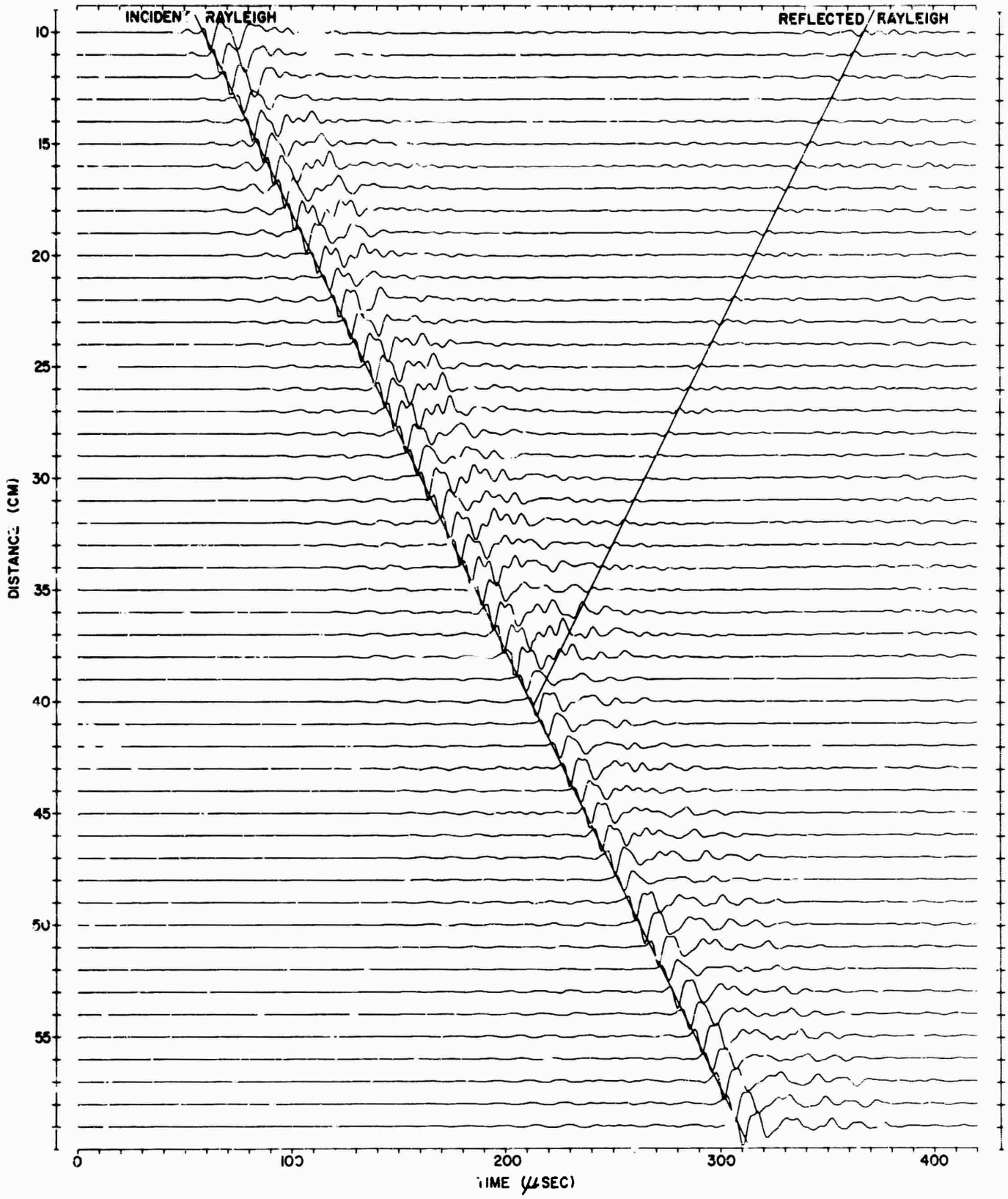

Figure III-14. Low Gain Vertical Recordings for Model H-6 with Scatterer 1 (Distance from the source ranges from 10 to 59 cm)

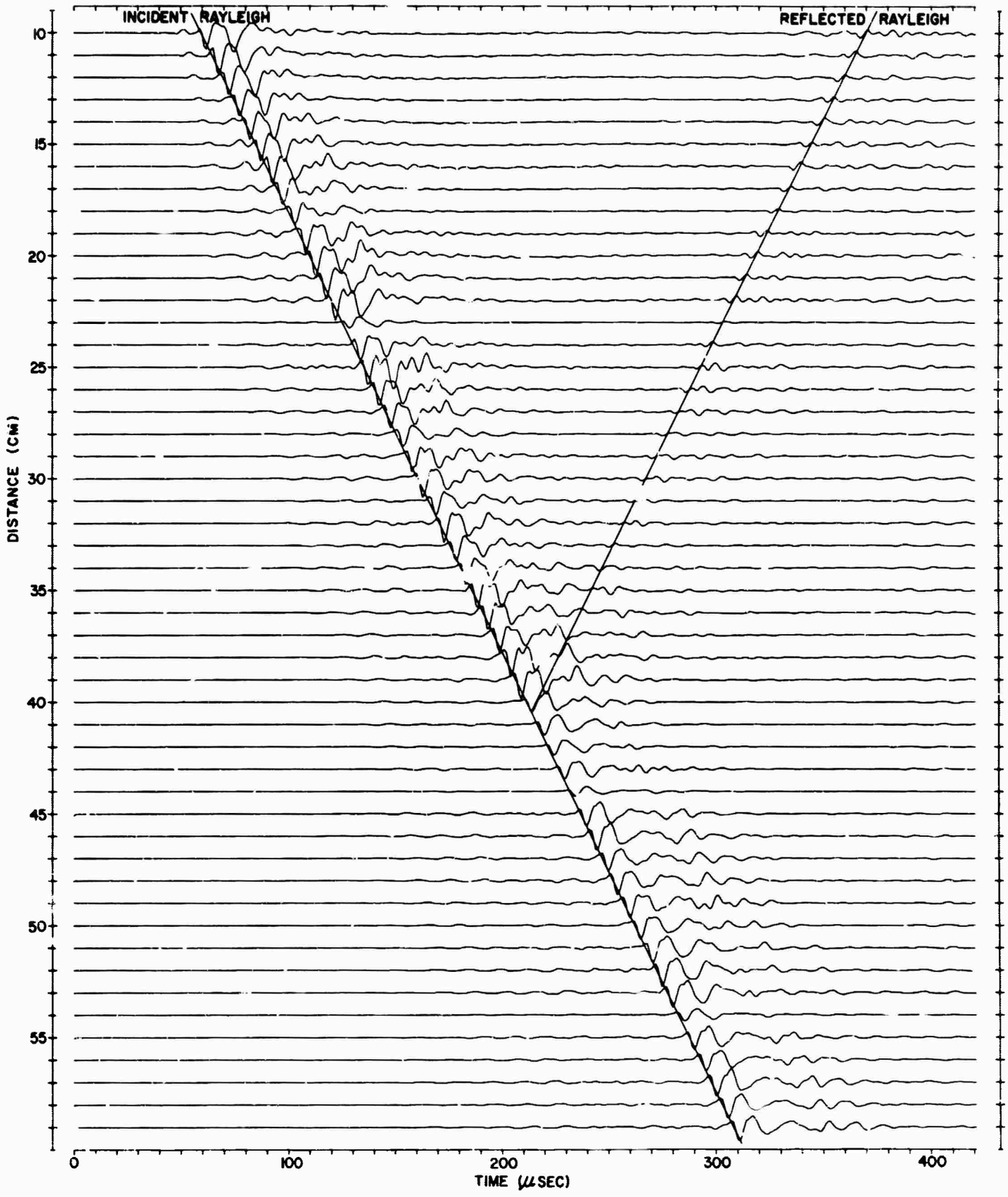

Figure III-15. Low Gain Vertical Recordings for Model H-6 with Scatterer 2 (Distance from the source ranges from 10 to 59 cm)

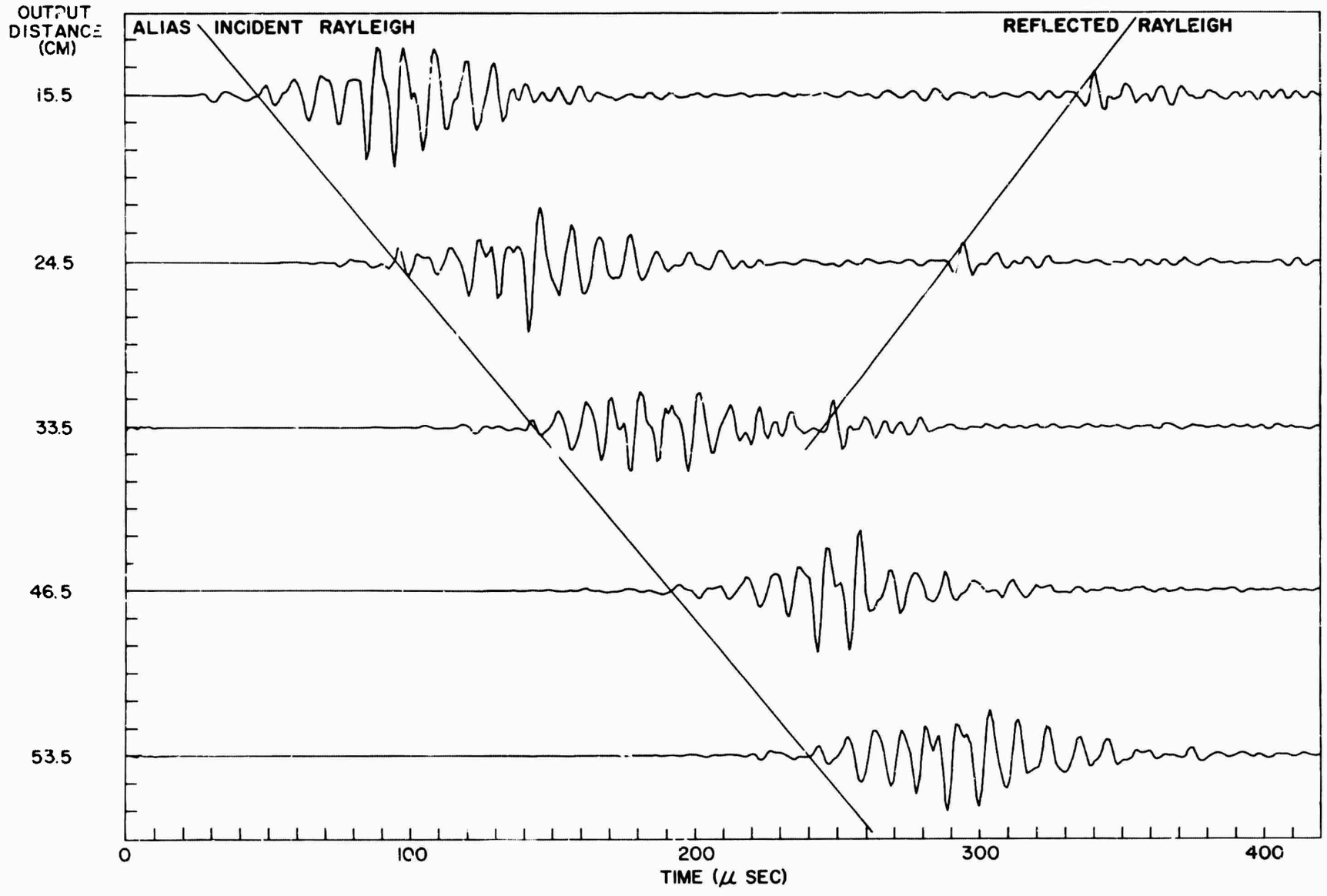

Figure III-16. Pie Sliced Output for Scatterer 1 at a Velocity of -2.0 km/μsec (Output distances are 15.5, 24.5, 33.5, 46.5, and 53.5 cm)

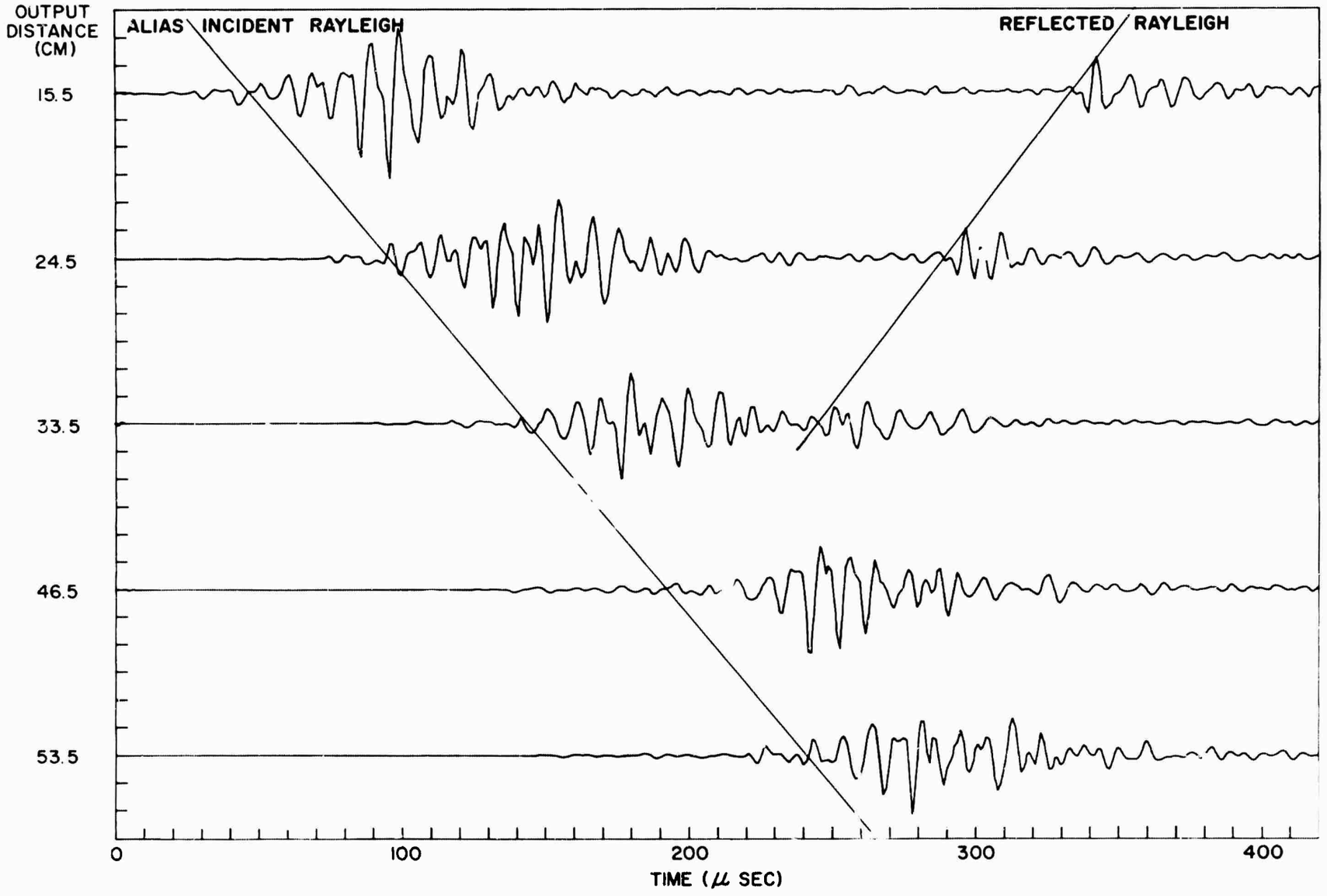

Figure III-17. Pie Sliced Output for Scatterer 2 at a Velocity of -2.0 km/μsec (Output distances are 15.5, 24.5, 33.5, 46.5, and 53.5 cm)

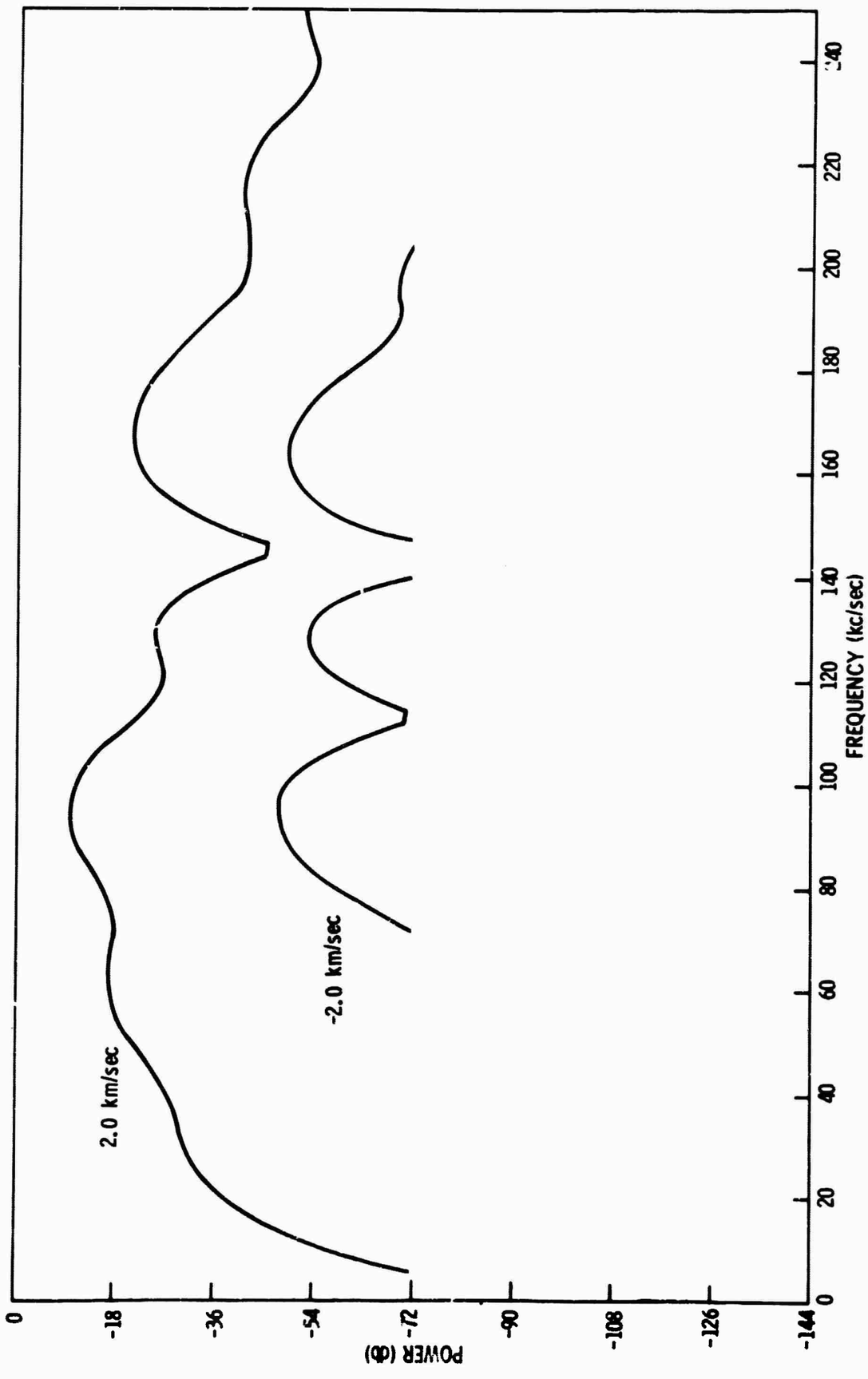

Figure III-18. Relative Vertical Power Spectra of Incident Rayleigh Mode and Scattered Energy at 15.5 cm from Source Using Scatterer 1

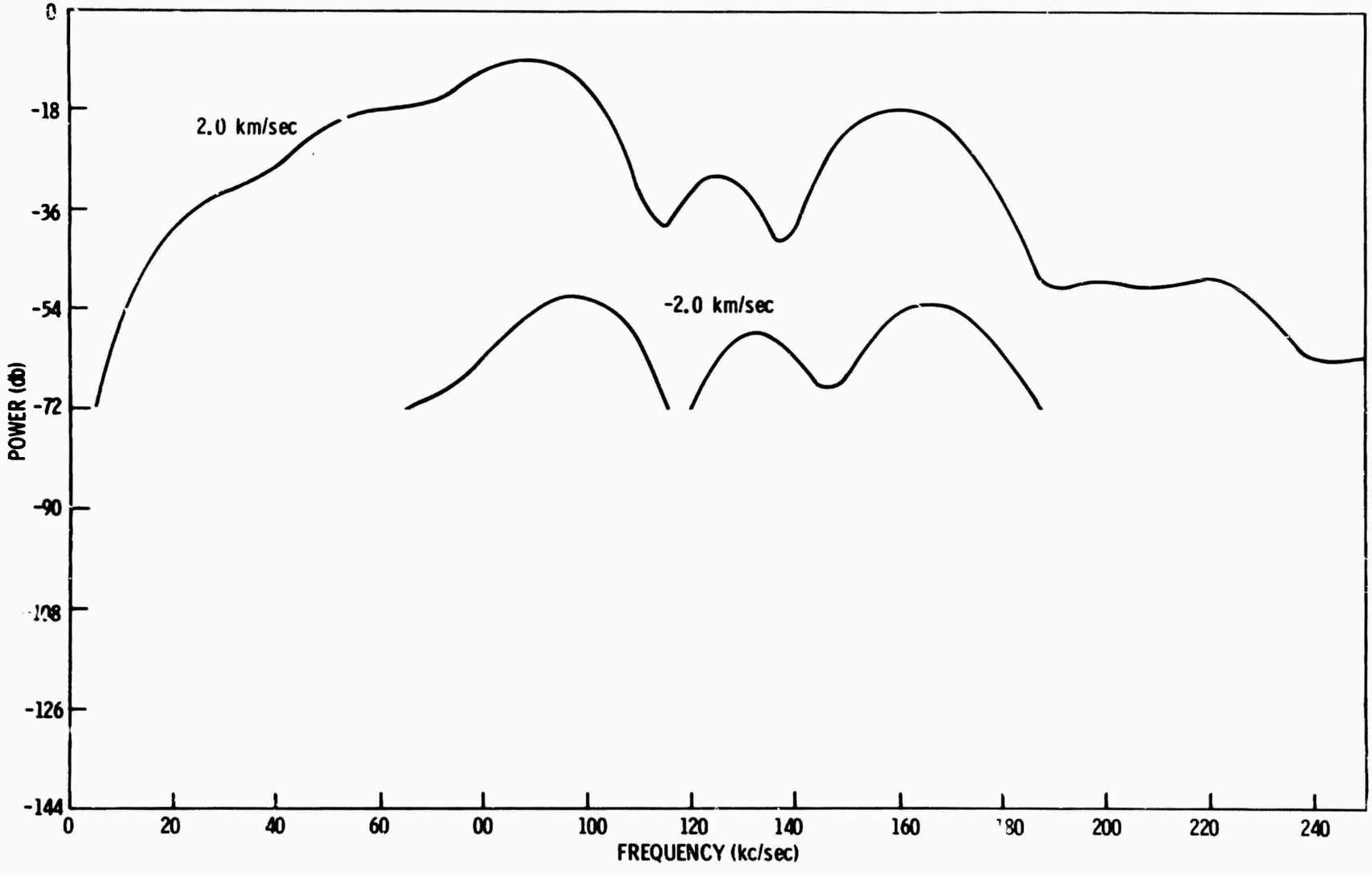

Figure III-19. Relative Vertical Power Spectra of Incident Rayleigh Mode and Scattered Energy at 24.5 cm from the Source Using Scatterer 1

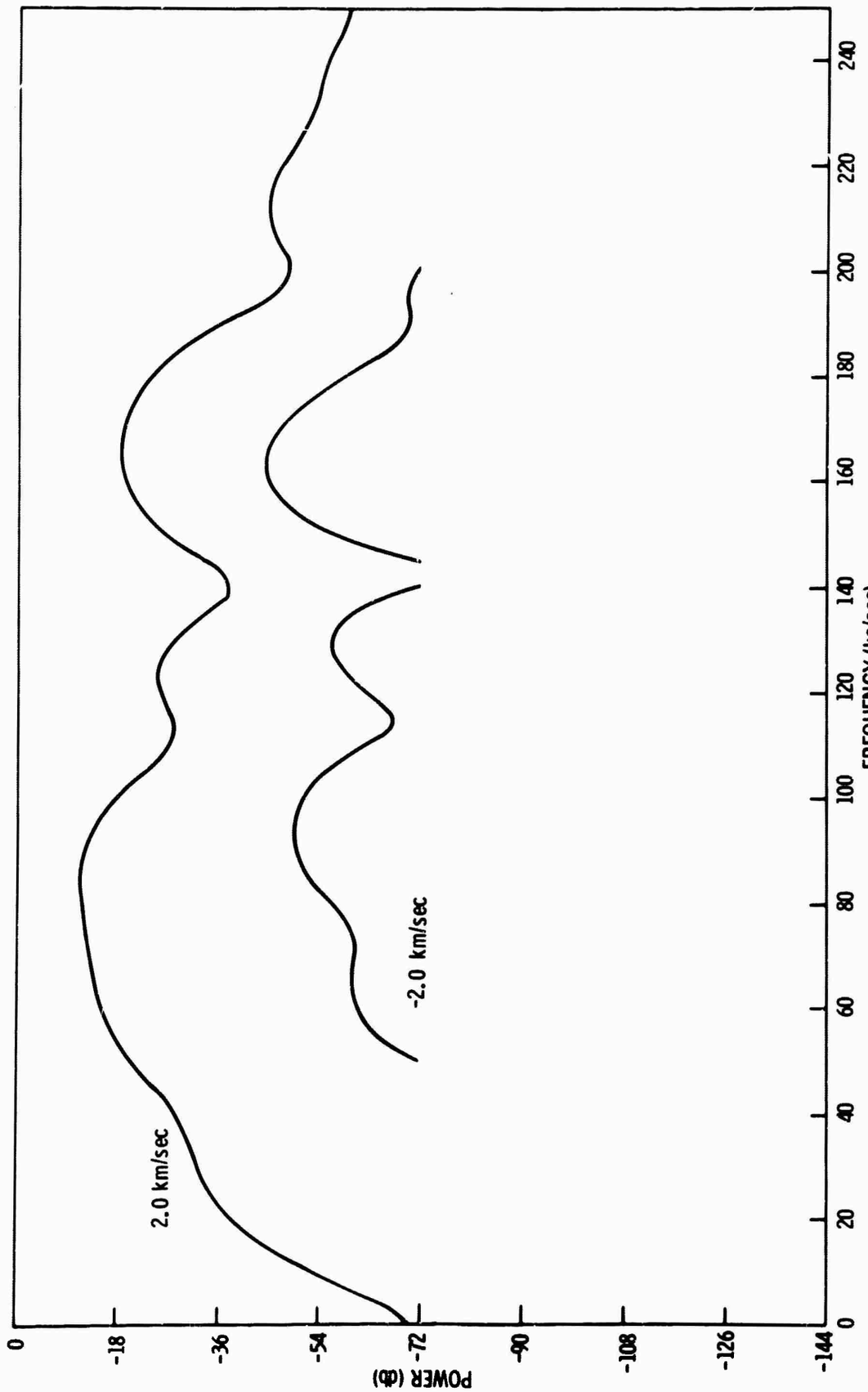

Figure III-20. Relative Vertical Power Spectra of Incident Rayleigh Mode and Scattered Energy at 33.5 cm from the Source Using Scatterer 1

in these figures indicates that wave lengths much larger than the dimensions of the scatterer are not strongly influenced by the surface irregularity. Power spectra for the transmitted Rayleigh wave at distances of 46.5 and 53.5 cm are shown in Figure III-21 for scatterer 1. Similar results for scatterer 2 are shown in Figures III-22 through III-25. In Figures III-18 through III-25, and value below -72 db would have no physical meaning since it falls outside the dynamic range of the digitizer used to record the output time traces.

Transfer functions that change the incident Rayleigh mode into the scattered energy were computed for both scatterers at output distances of 15.5, 24.5 and 33.5 cm. The amplitudes of the transfer functions are plotted in Figure III-26. These results are compatible with previous conclusions.

Theoretically, a time trace taken from the model with no scatterer present may be subtracted from a trace taken with the scatterer in place, leaving only reflected energy. However, due to the receiver crystal coupling and slight placement differences, this is not the case experimentally and, therefore, the waveforms differ slightly. When the traces are subtracted in the above manner, residual incident energy remains because of the slight difference in waveform.

In order to achieve the desired subtraction, crossequalization filters were designed which remove experimentally induced discrepancies in the waveforms of the incident Rayleigh energy.

An 11-point prediction filter was designed using correlations constructed over a time gate of 400 points. The short length filter was used so that it would design primarily on the incident Rayleigh energy and

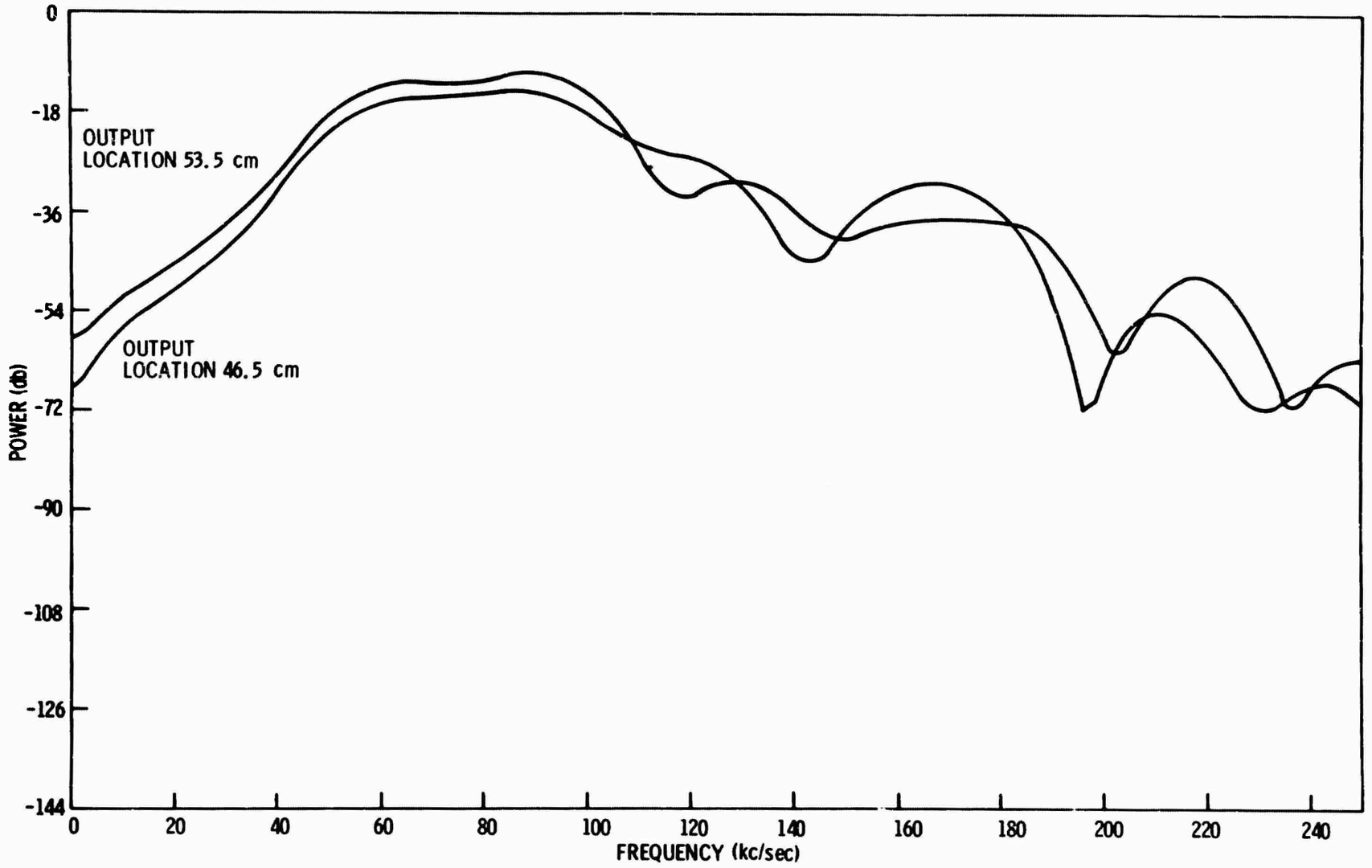

Figure III-21. Relative Vertical Power Spectra of Incident Rayleigh Mode at Distances of 46.5 and 53.5 cm from the Source Using Scatterer 1

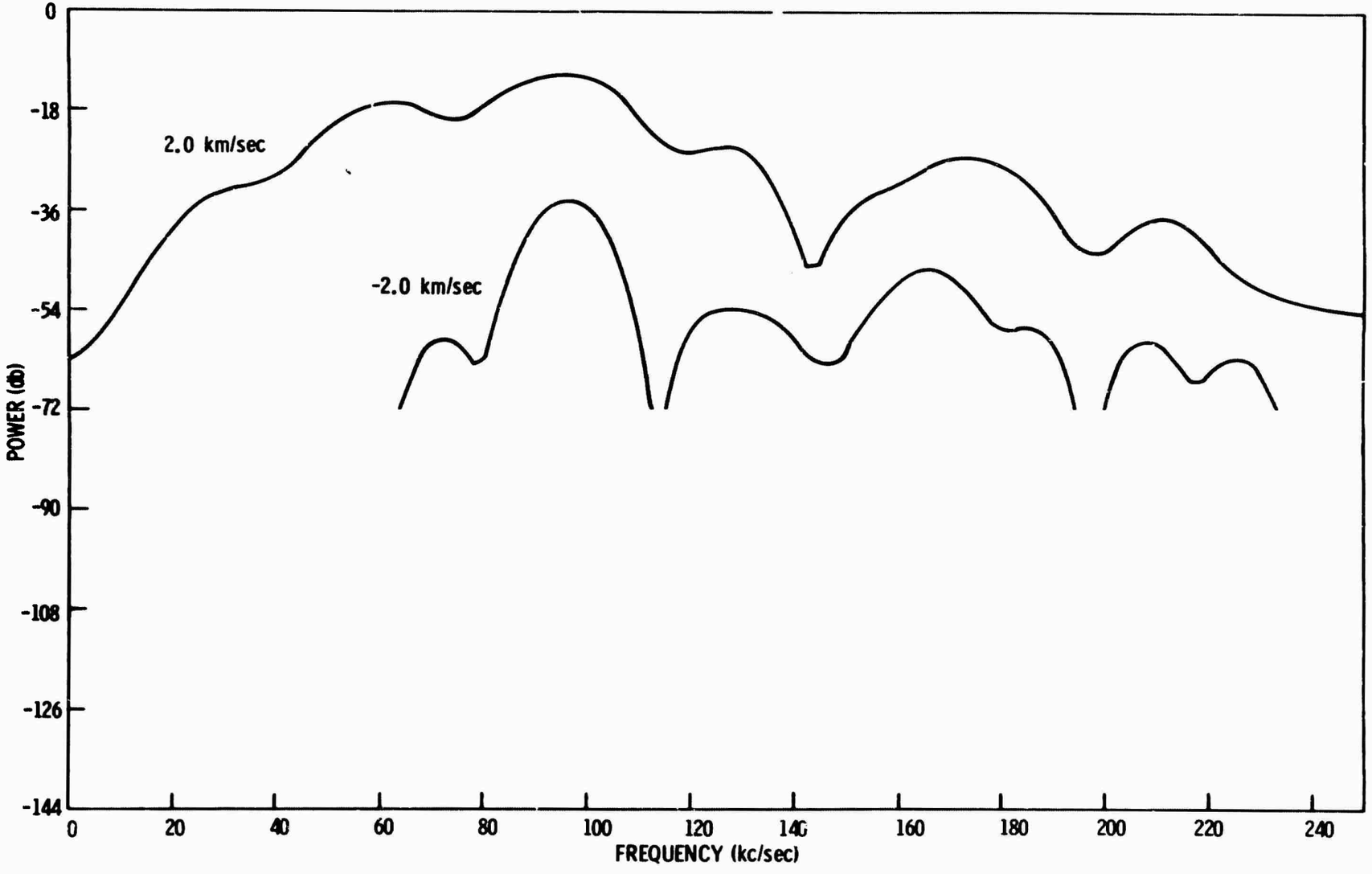

Figure III-22. Relative Vertical Power Spectra of Incident Rayleigh Mode and Scattered Energy at 15.5 cm from Source Using Scatterer 2

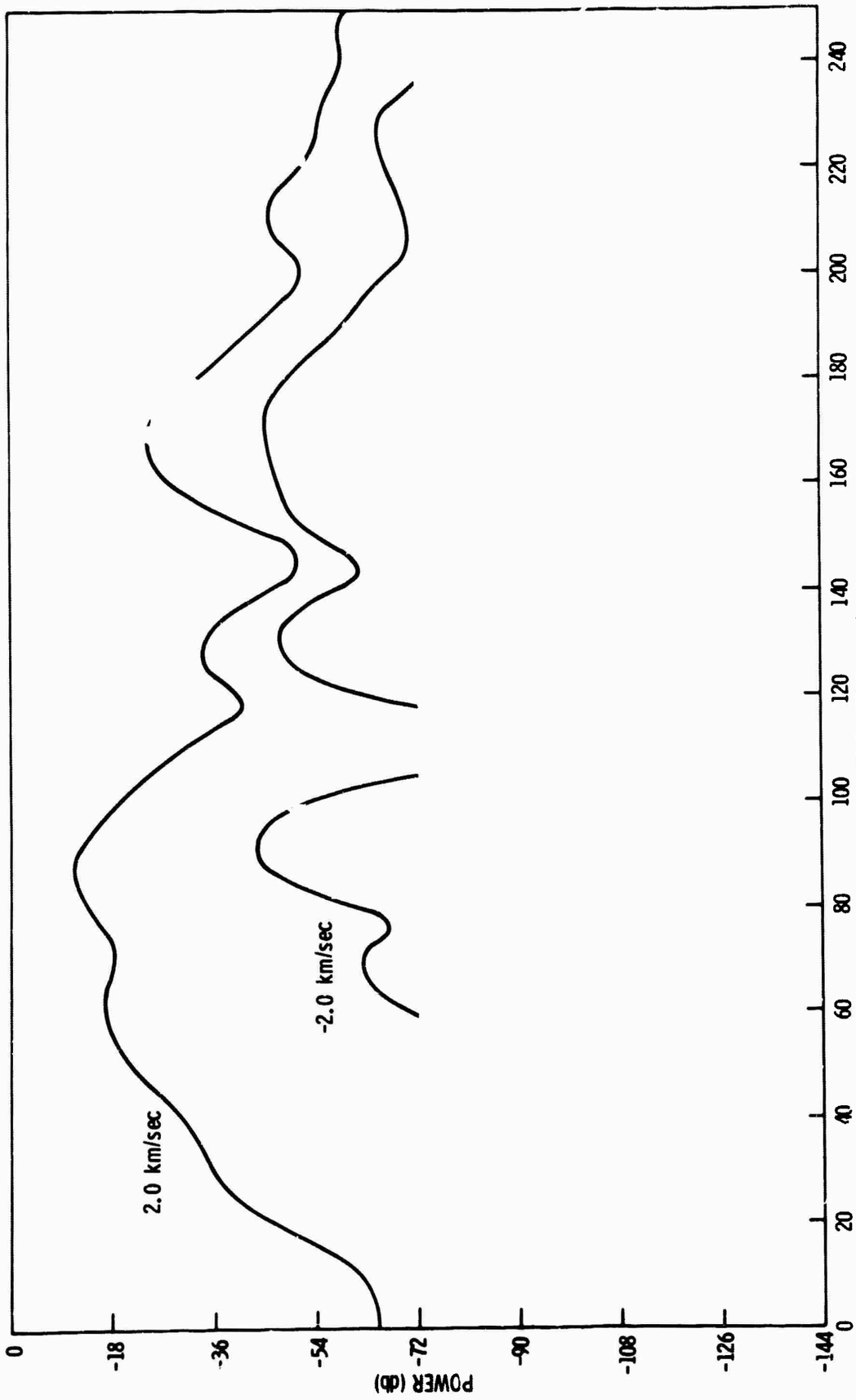

Figure III-23. Relative Vertical Power Spectra of Incident Rayleigh Mode and Scattered Energy at 24.5 cm from Source Using Scatterer 2

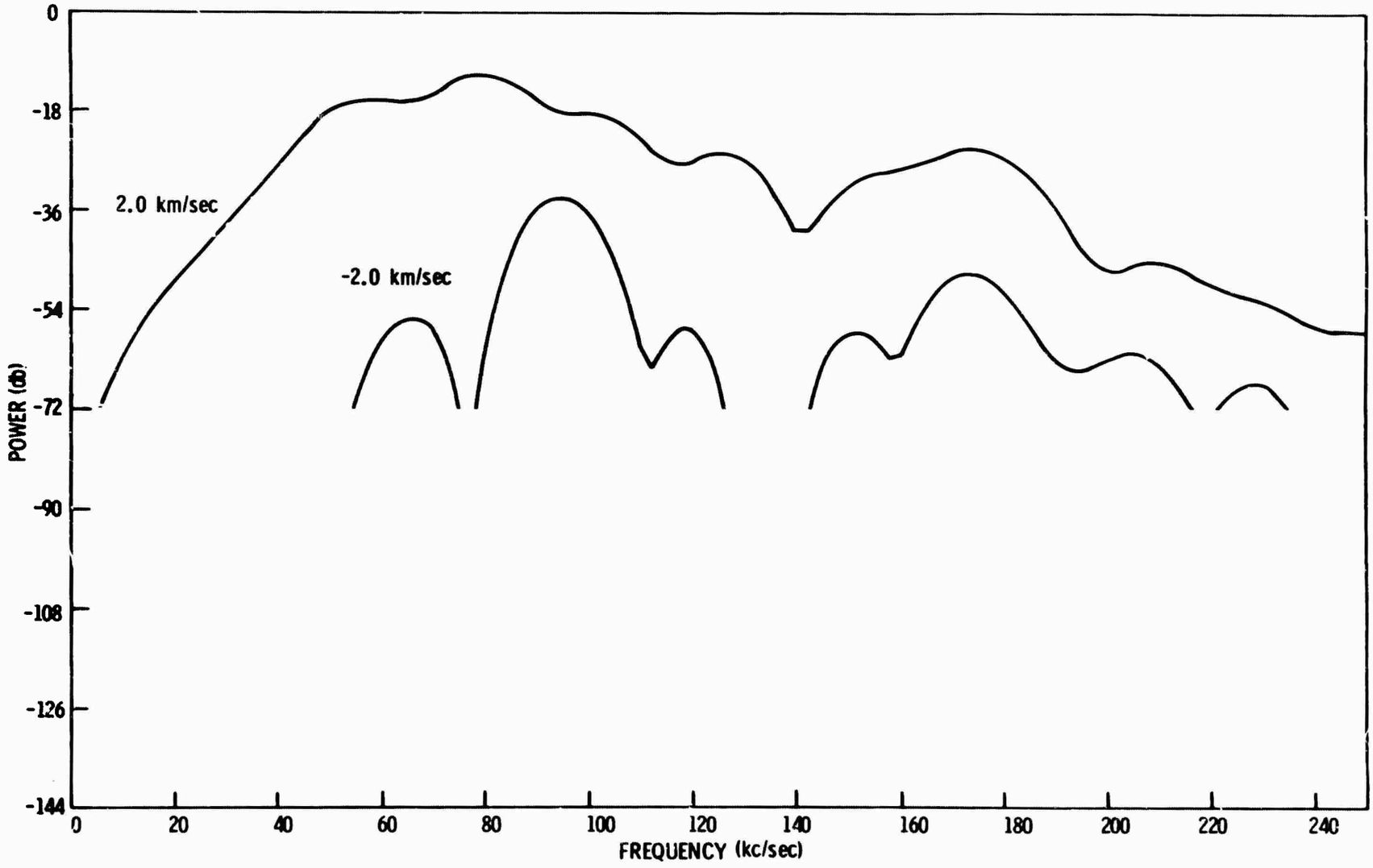

Figure III-24. Relative Vertical Power Spectra of Incident Rayleigh Mode and Scattered Energy at 33.5 cm from Source Using Scatterer 2

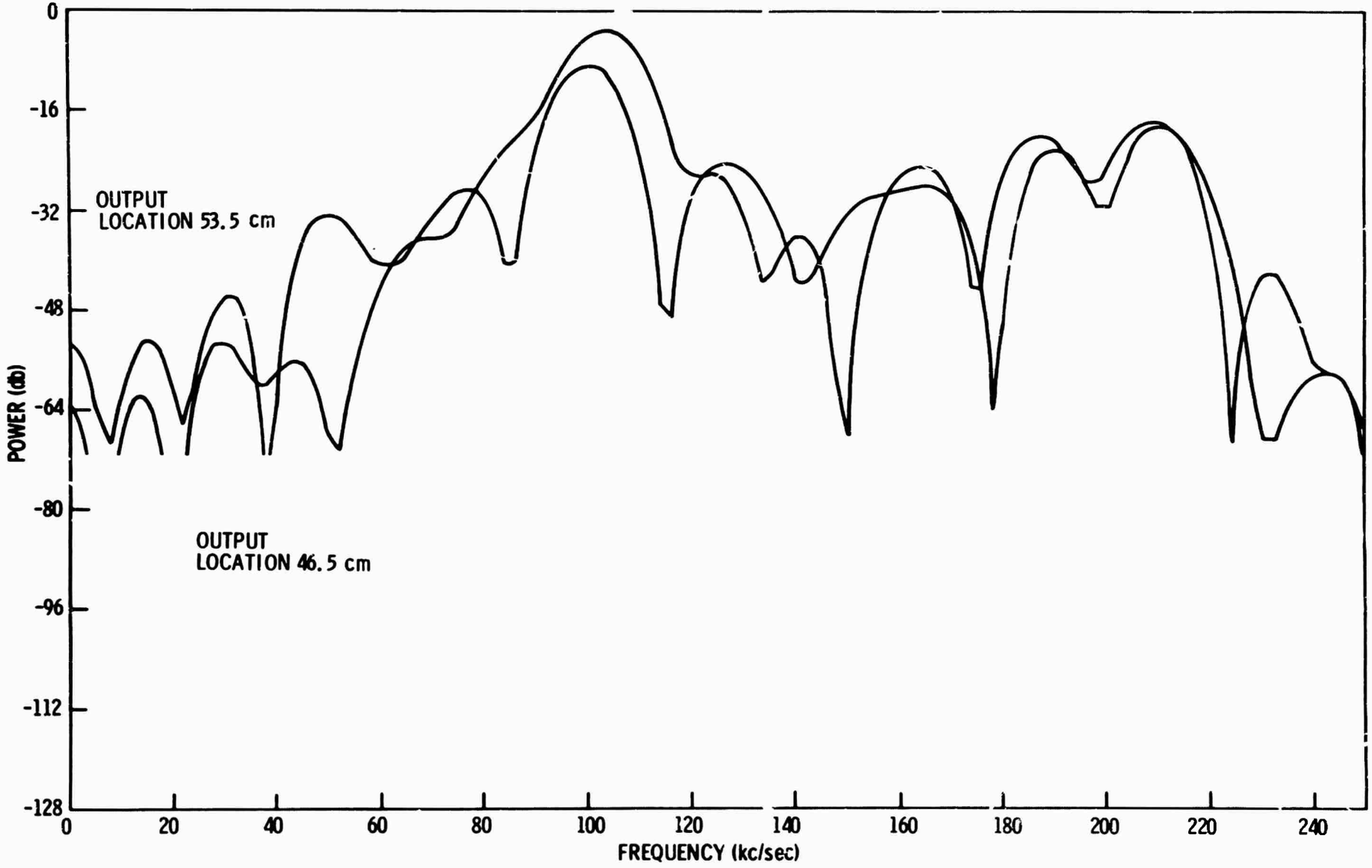

Figure III-25. Relative Vertical Power Spectra of Incident Rayleigh Mode at Distances at 46.5 and 53.5 cm from Source Using Scatterer 2

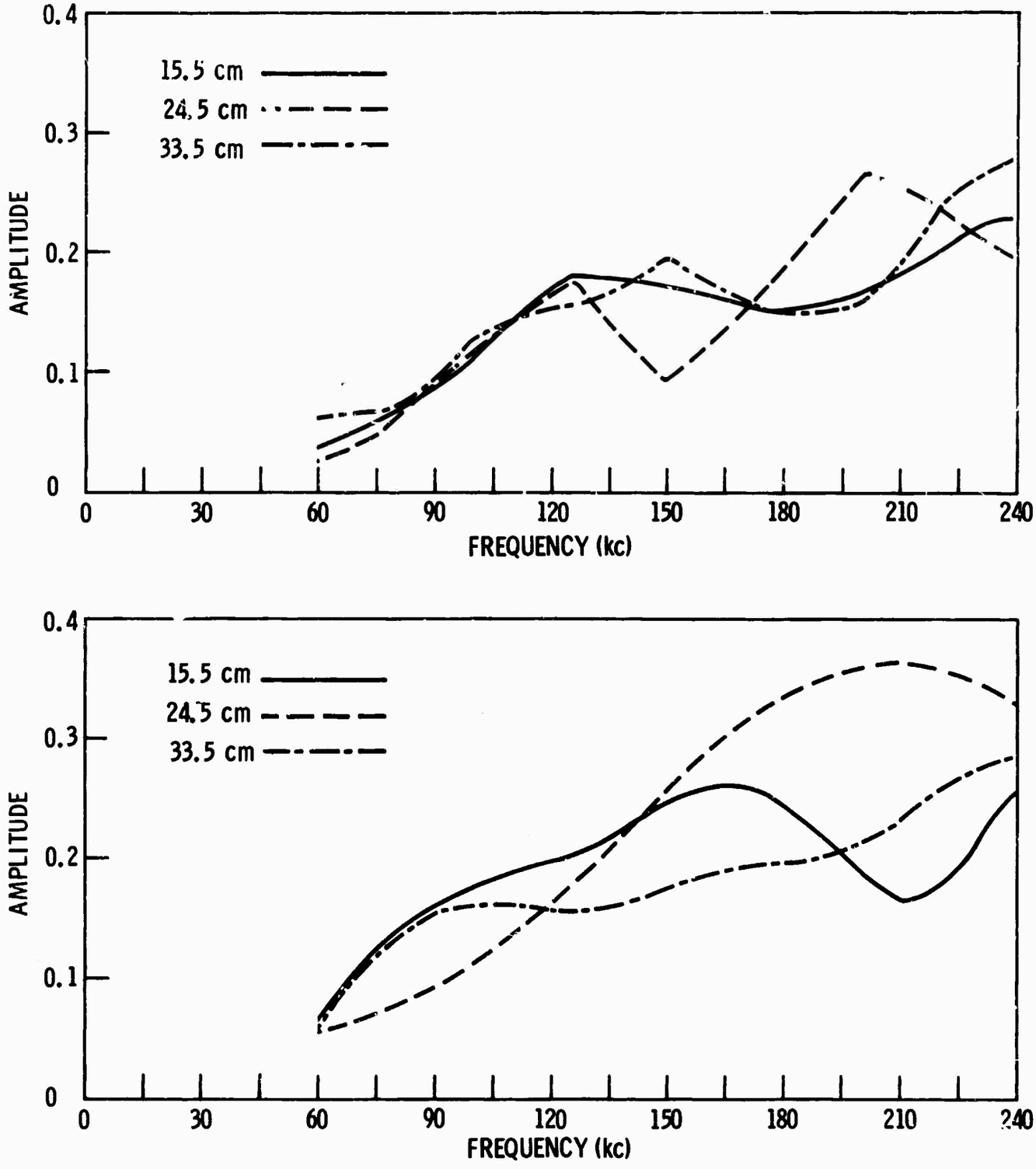

Figure III-26. Amplitude of Transfer Function for Distances of 15.5, 24.5 and 33.5 cm for Scattered 1 (above) and Scatterer 2 (below)

not try to fit the backward reflected energy. The filters were applied to the trace with no scatterer present.

The convolved trace was then subtracted from the trace recorded with the scatterer present. This was done for corresponding traces at each output distance from 10 to 40 cm. The convolved output traces are shown in Figures III-27 and III-28, respectively, for scatterers 1 and 2. The results after subtracting the convolved traces from corresponding time traces are shown in Figures III-29 through III-32.

Results vary from location to location. If the 11-point filter had worked perfectly, the result after crossequalization and subtracting would have been only scattered energy. The residual incident Rayleigh energy is due to the inability of the filter to do a perfect job. This results partially from the fact that the two traces at the same output location are not sufficiently similar in shape.

The scattered signal is enhanced by applying the Pie Slice operator for a velocity of -2.0 mm/μsec to the results of the crossequalization and subtraction process (Figures III-29 through III-32). The net effect of the processing up to this point has been to reduce the incident Rayleigh mode by 12 to 18 db for both scatterers.

The Pie Sliced outputs for both scatterers are shown in Figures III-33 through III-36. Each result is shown at the same level as the original input traces, as well as at a 12-db higher gain. It is difficult to observe any reflected energy other than the -2.0 mm/μsec energy. Some of the +2.0 mm/μsec energy remaining is aliased energy. Cross-equalization and subtraction left a smaller residual energy for scatterer 2.

Future plans for scattering studies with Model H-6 will include recording data with the source on the surface of the 5cm end, as well as on the bottom of the model, and development of a theoretical scattering program.

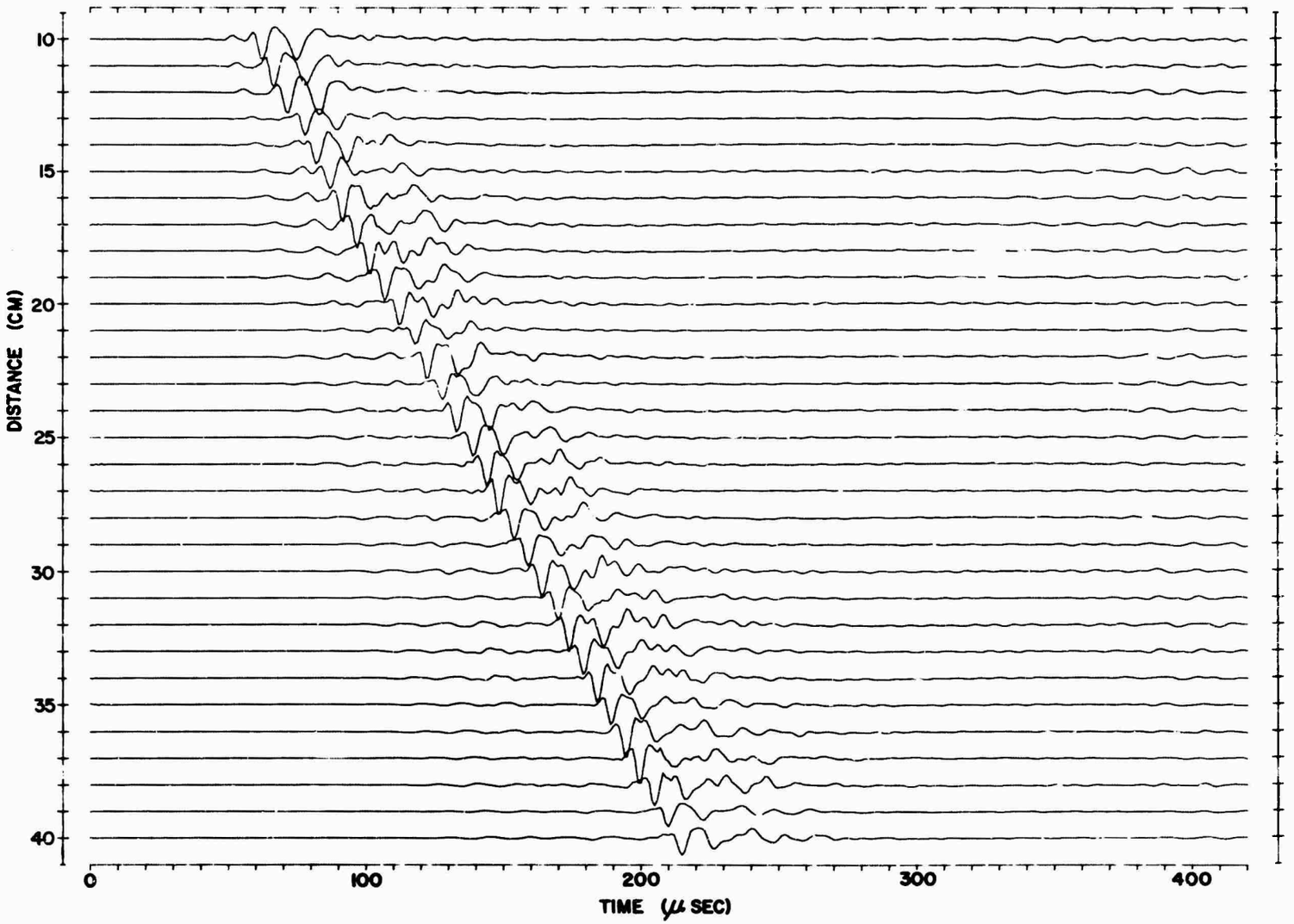

Figure III-27. Vertical Recordings Convolved with 11-Point Filter for Scatterer 1 (Output distance is from 10 to 40 cm)

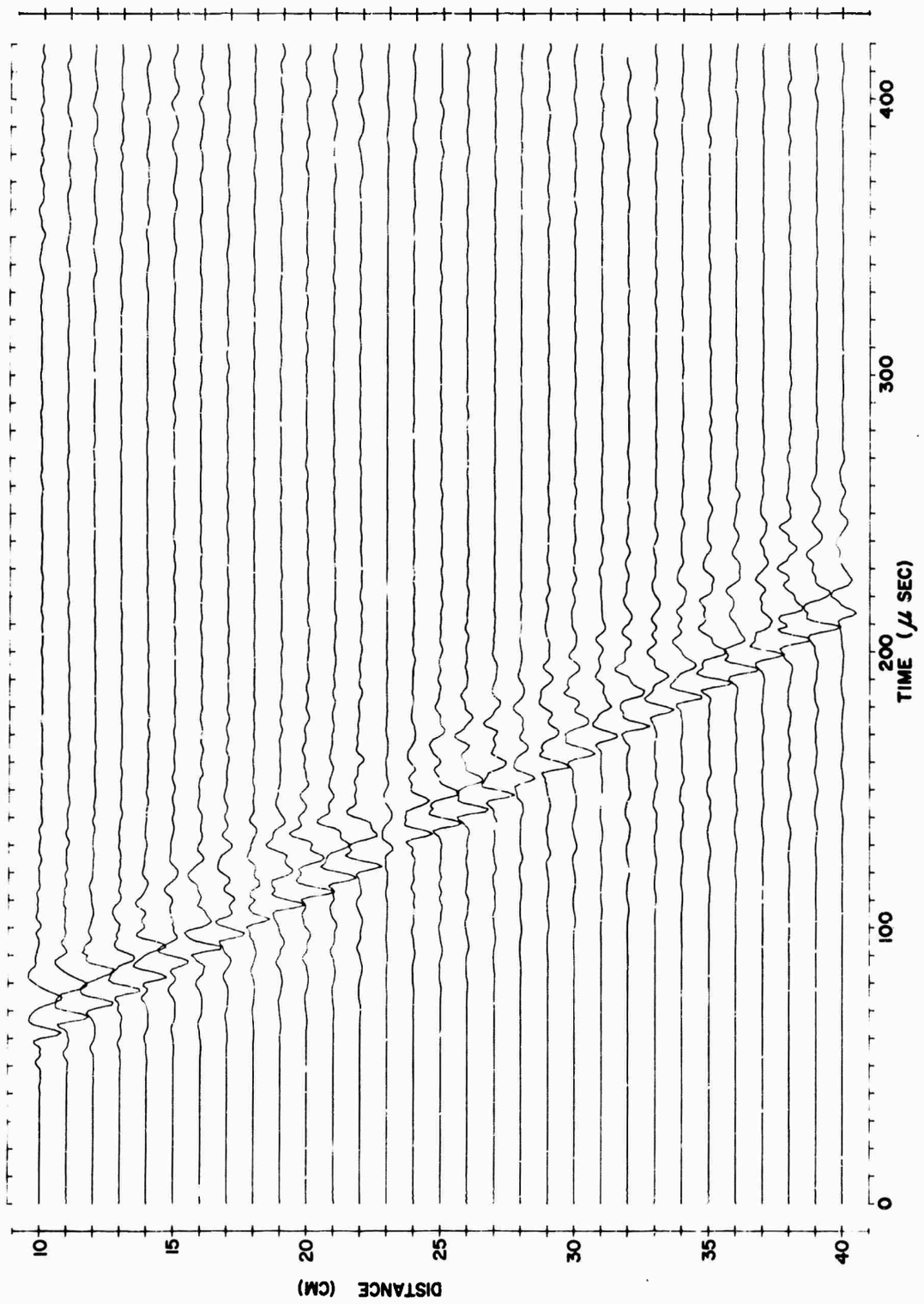

Figure III-28. Vertical Recordings Convolved with 11-Point Filter for Scattered 2 (Output distance is from 10 to 40 cm)

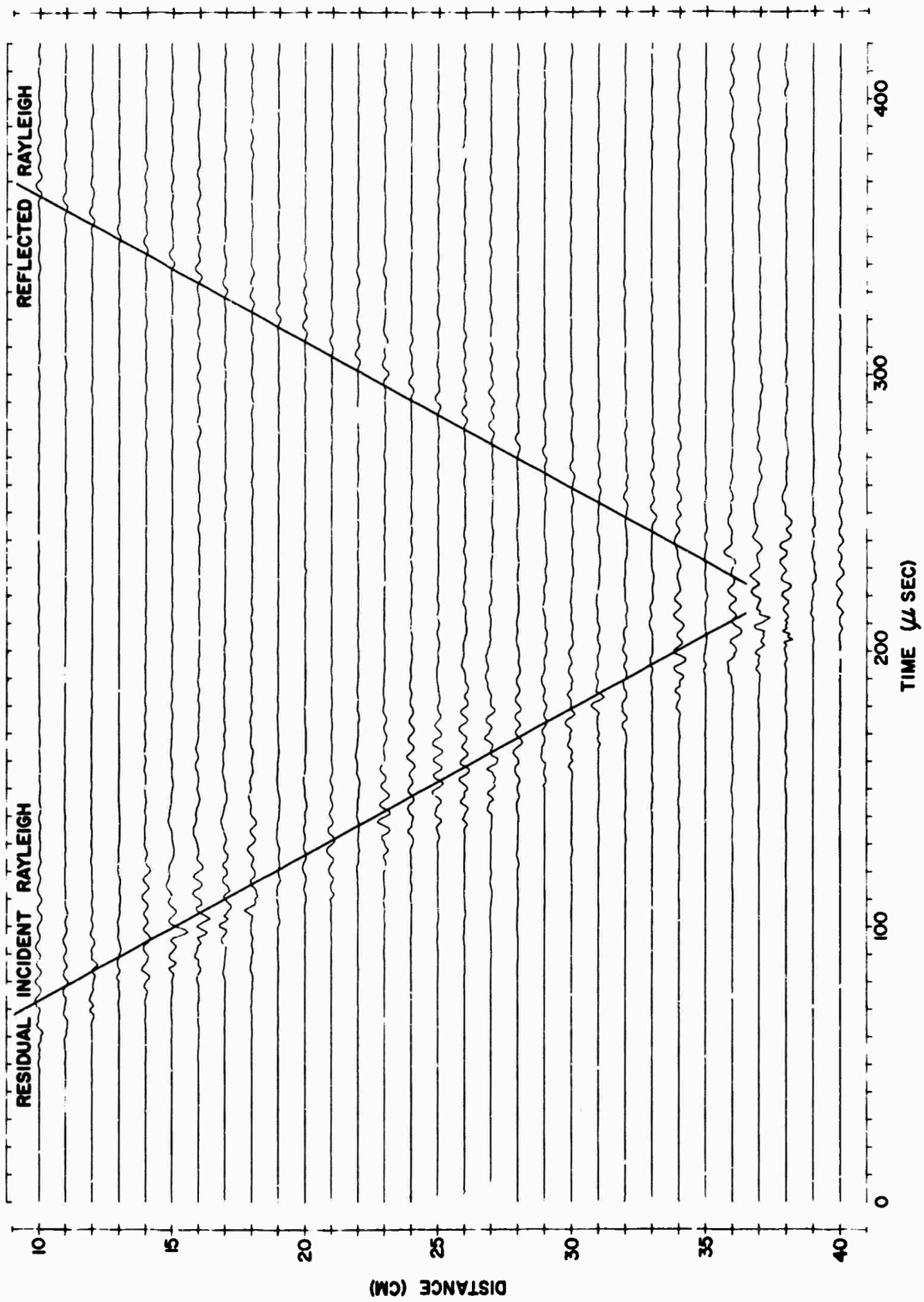

Figure III-29. Crossequalization and Subtraction Results for Scatterer 1 (Output distance is from 10 to 40 cm, zero gain)

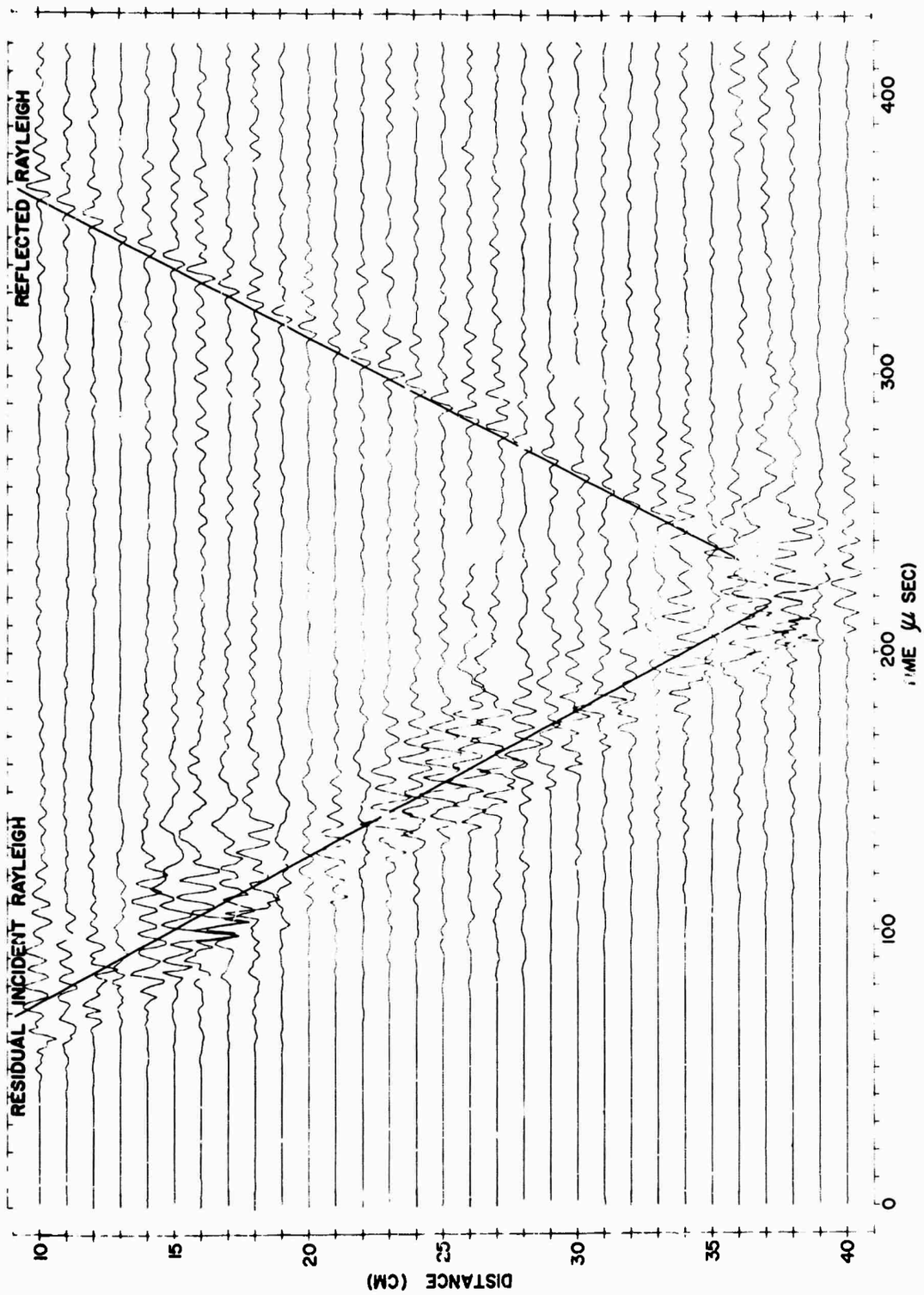

Figure III-30. Crossequalization and Subtraction Results for Scatterer 1 (Output distance is from 10 to 40 cm, 12 dB gain)

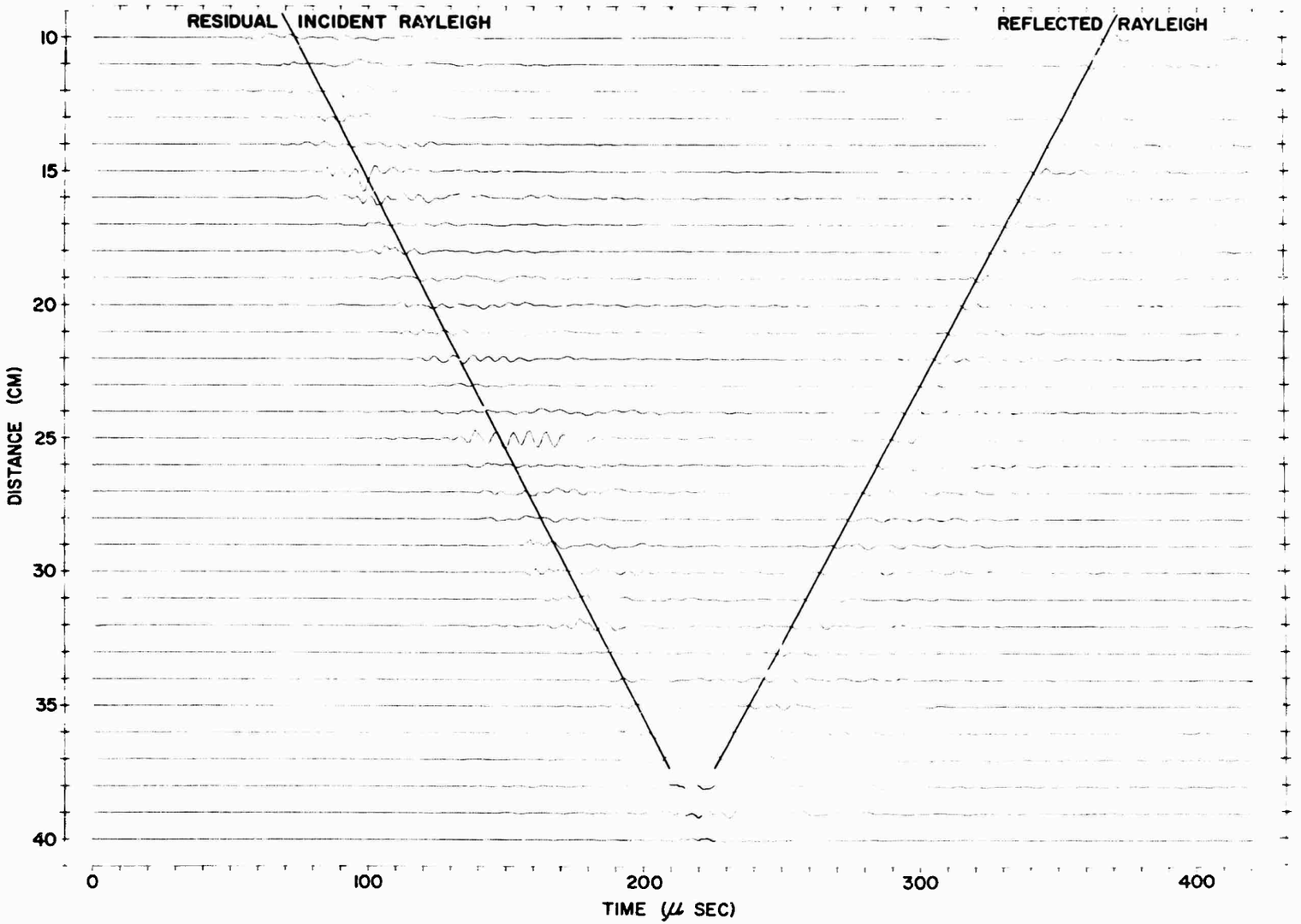

Figure III-31. Crossequalization and Subtraction Results for Scatterer 2 (Output distance is from 10 to 40 cm, zero gain)

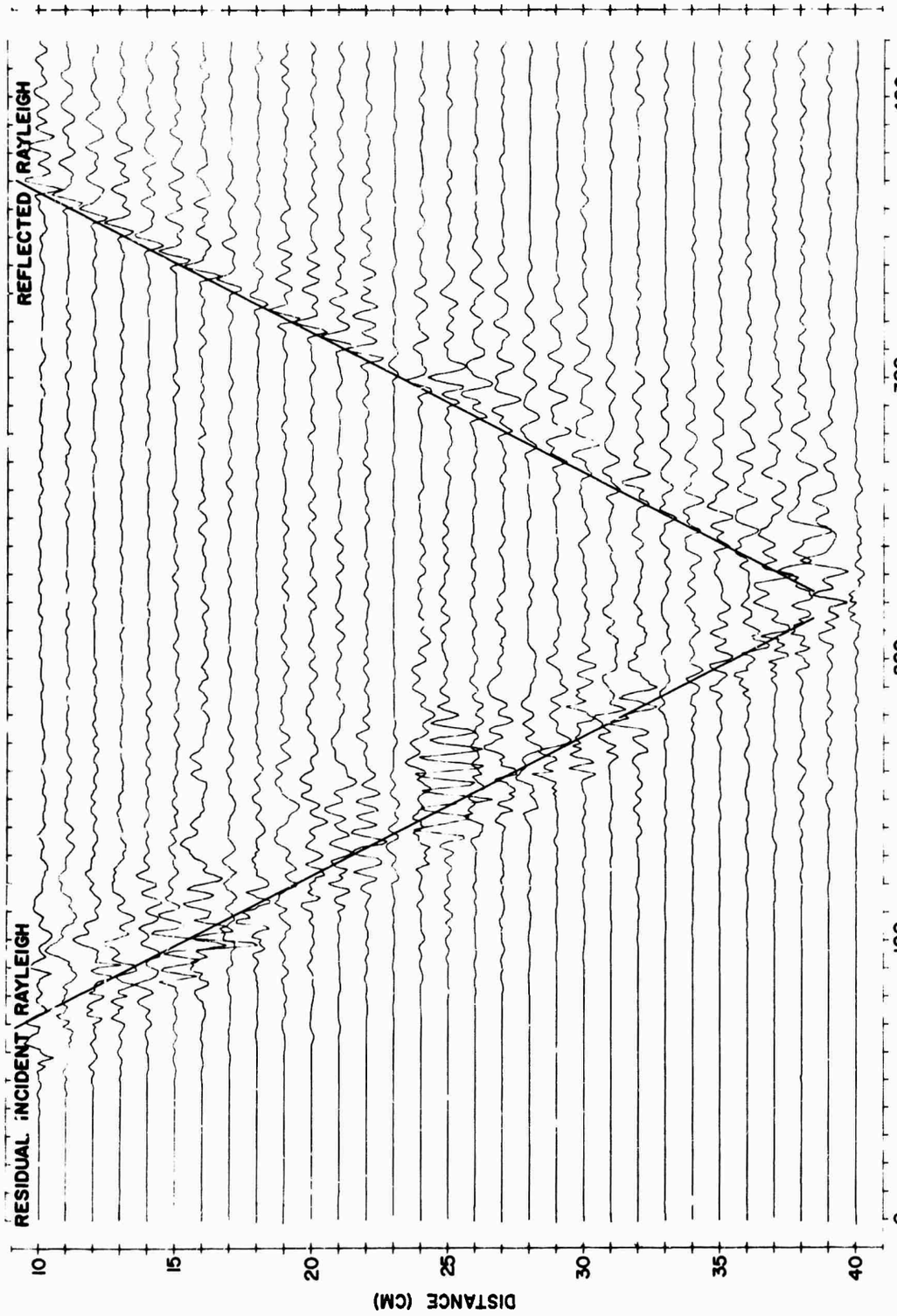

Figure III-32. Crossequalization and Subtraction Results for Scatterer 2 (Output distance is from 15.5 to 33.5 cm, zero gain)

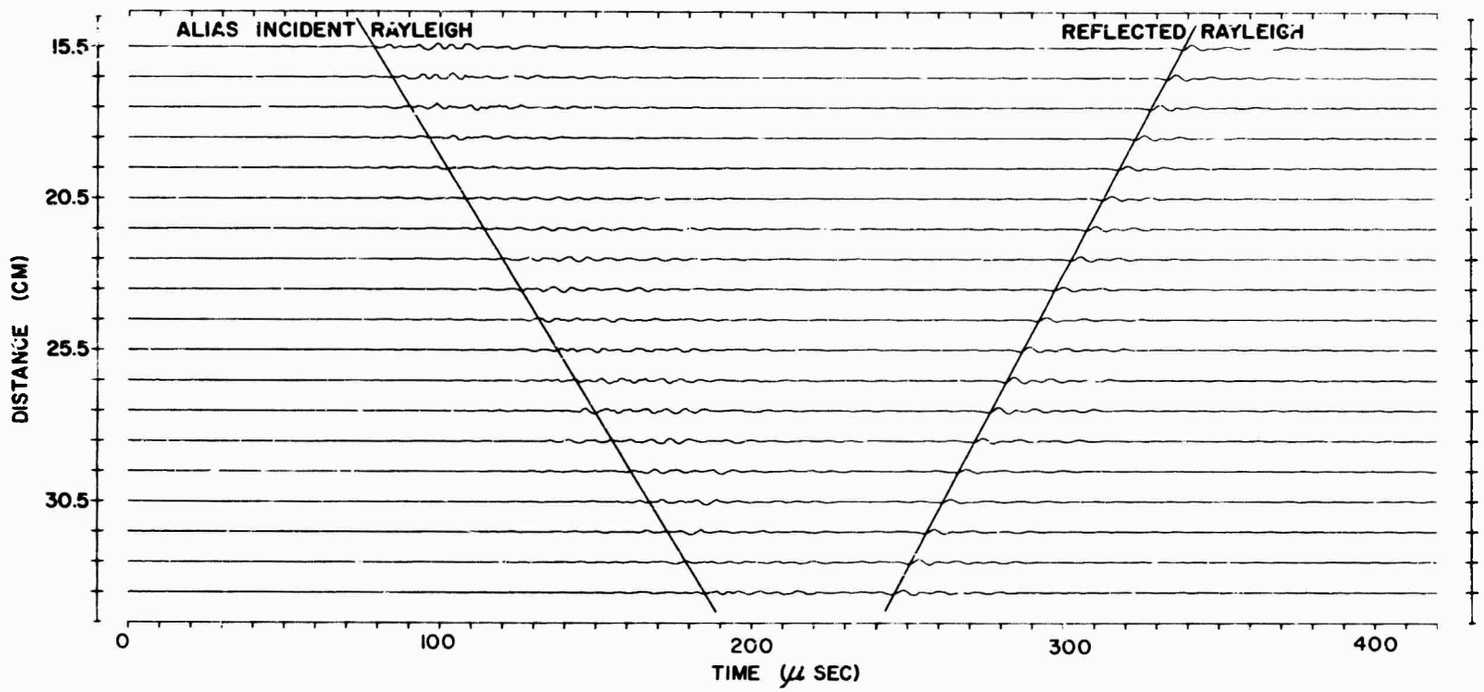

Figure III-33. Crossequalization and Subtraction Results for Scatterer 1 Pie Sliced at -2.0 mm/μsec (Output distance is from 15.5 to 33.5 cm, zero gain)

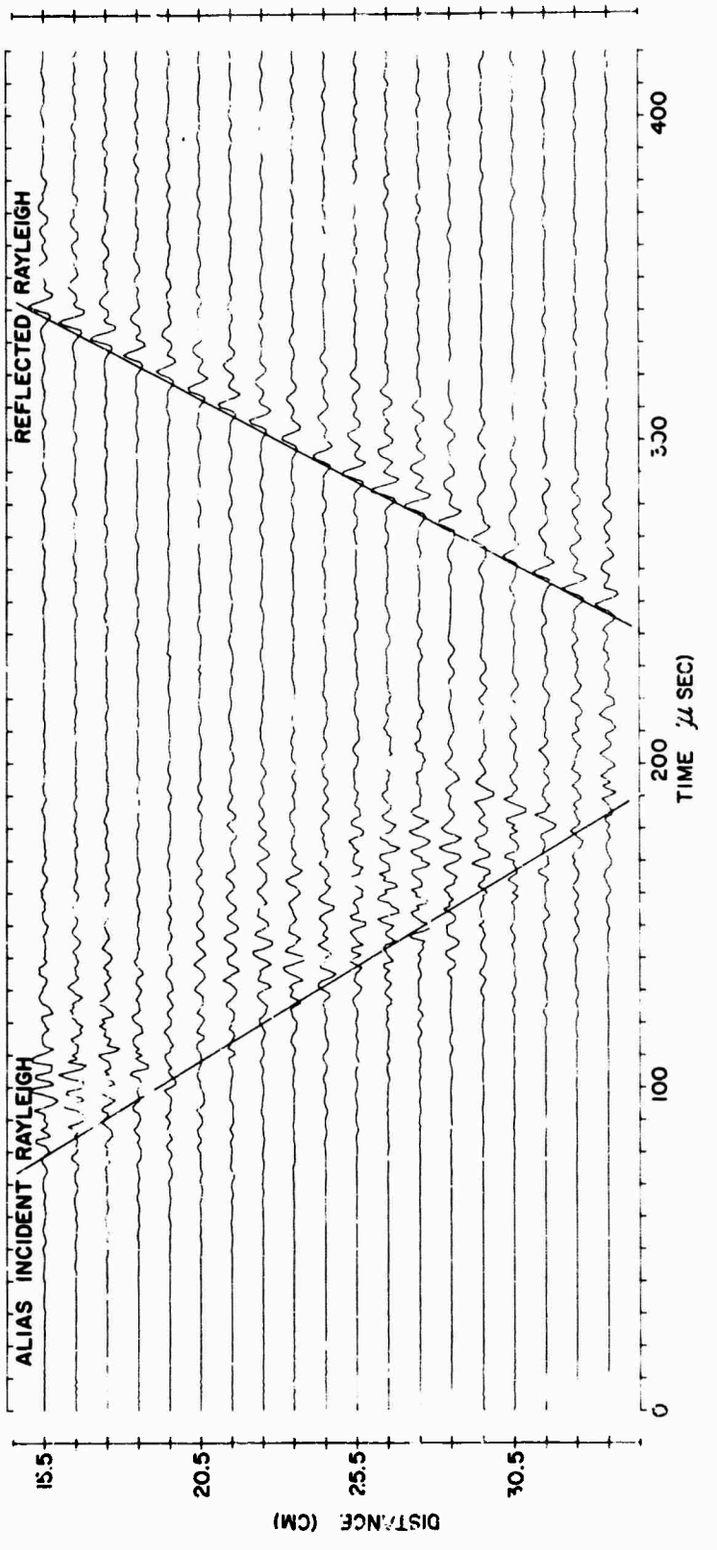

Figure III-34. Crossequalization and Subtraction Results for Scatterer 1 Pie Sliced at -2.0 mm/μsec (output distance is from 15.5 to 33.5 cm, 12 db gain)

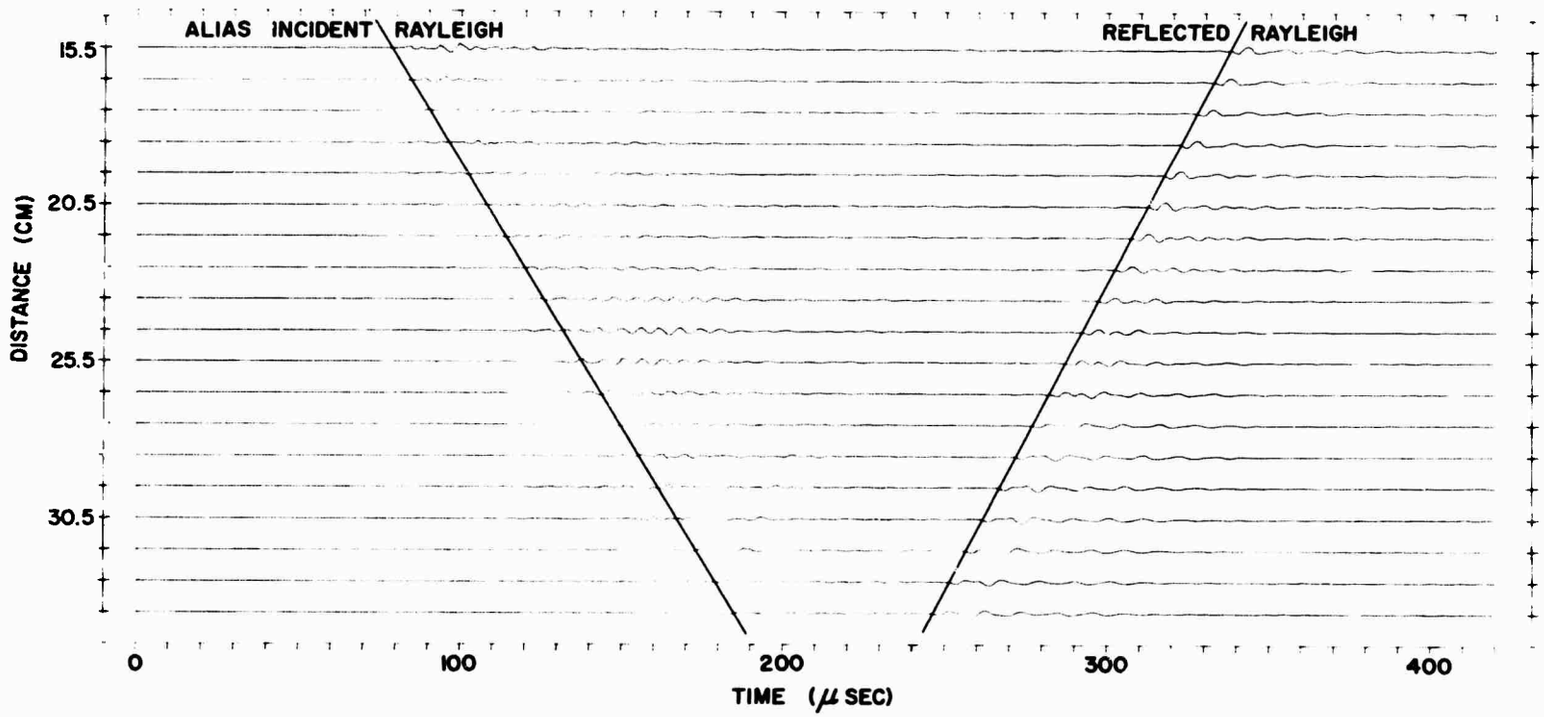

Figure III-35. Crossequalization and Subtraction Results for Scatterer 2 Pie Sliced at -2.0 mm/μsec (Output distance is from 15.5 to 33.5 cm, zero gain)

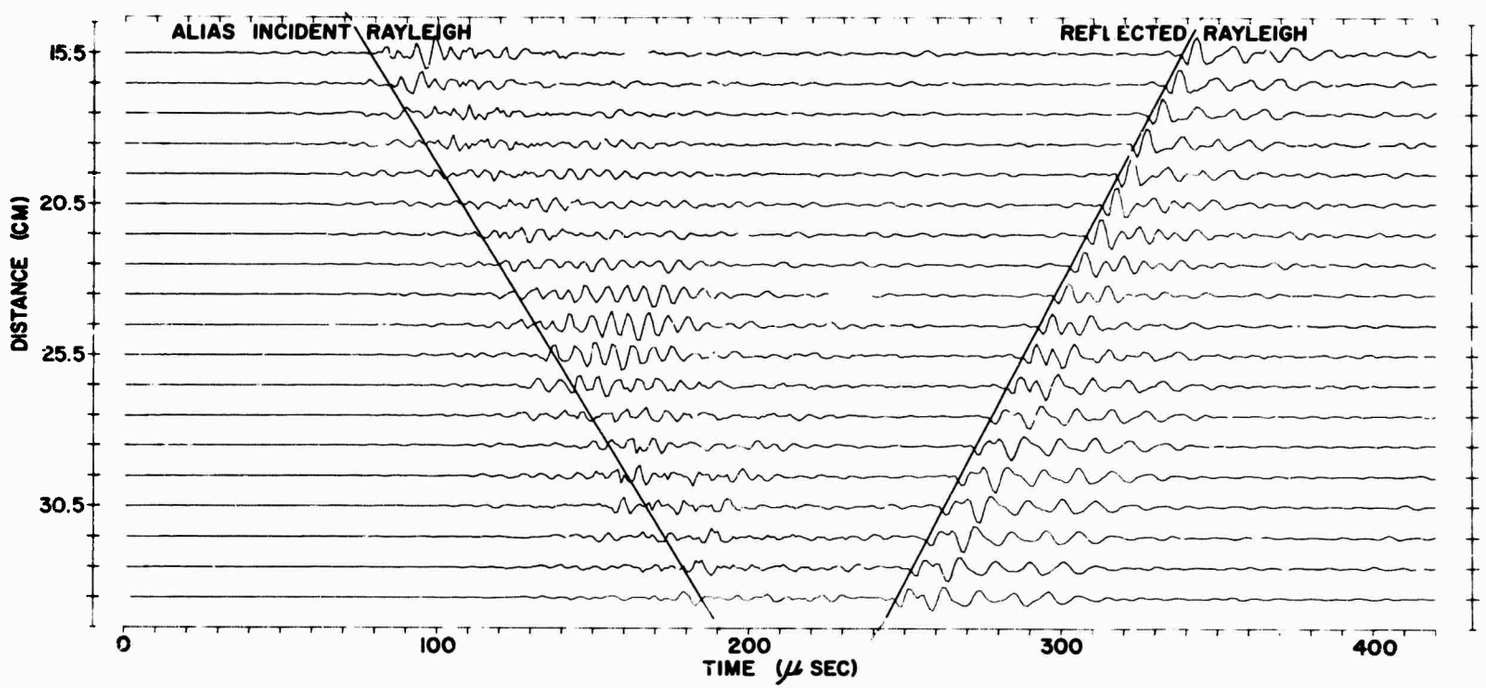

Figure III-36. Crossequalization and Subtraction Results for Scatterer 2 Pie Sliced at -2.0 mm/μsec (Output distance is from 15.5 to 33.5 cm, 12 db gain)

SECTION IV

REFERENCES

1. Steinhart, John S. and Robert P. Meyer, 1961: Explosion Studies of Continental Structure, Carnegie Institution of Washington, Publication 622, Washington, D.C.

   Texas Instruments Incorporated, 1965: Basic Research in Crustal Studies, Final Rpt., Appendix D, Contract AF 49(638)-1244, 31 Dec.

3. Laster, S.J. and A. Frank Linville, 1966: Application of Multichannel Filtering to the Separation of Dispersive Modes of Propagation, J. of Geophysical Research, v. 71, n. 6, 15 Mar., p 1669-1701.

4. Texas Instruments Incorporated, 1965: Basic Research in Crustal Studies, Final Rpt., Appendix F, Contract AF 49(638)-1244, 31 Dec.

5. Texas Instruments Incorporated, 1965: Basic Research in Crustal Studies, Final Rpt., Appendix G, Contract AF 49(638)-1244, 31 Dec.

6. Laster, Stanley J., Joe G. Foreman, and A. Frank Linville, 1965; Theoretical Investigation of Modal Seismograms for a Layer Over a Half-Space, Geophysics, v. XXX, n. 4, Aug., p 571-596.

7. Ewing, W. Maurice, Wenceslas S. Jardetsky, Frank Press, 1957: Elastic Waves in Layered Media, McGraw-Hill Book Company, Inc.,

8. Linville, A. Frank and Stanley J. Laster, 1966: Numerical Experiments in the Estimation of Frequency Wavenumber Spectra of Seismic Events Using Linear Arrays, Bull. Seis. Soc. Amer., v. 56, n. 6, Dec., p 1337-1355.

9. Embree, Peter, J.B. Burg, and Milo M. Backus, 1963: Wideband Velocity Filtering — the Pie-Slice Process, Geophysics, n. 6, Dec., p 948-974.

DOCUMENT CONTROL DATA - R & D

(Security classification of title, body of abstract and indexing annotation must be entered when the overall report is classified)

1. ORIGINATING ACTIVITY (Corporate author)
TEXAS INSTRUMENTS INCORPORATED
Science Services Division
P.O. Box 5621, Dallas, Texas 75222

2a. REPORT SECURITY CLASSIFICATION
UNCLASSIFIED

2b. GROUP

3. REPORT TITLE
CONTINUATION OF BASIC RESEARCH IN CRUSTAL STUDIES, ANNUAL REPORT

4. DESCRIPTIVE NOTES (Type of report and inclusive dates)
Scientific, ---Interim

5. AUTHOR(S) (First name, middle initial, last name)
Linville, A. Frank
Miller, Max K.
Harris, Hugh K.

6. REPORT DATE
30 January 1967

7a. TOTAL NO. OF PAGES
133

7b. NO. OF REFS
9

8a. CONTRACT OR GRANT NO.
AF 49(638)-1588

b. PROJECT NO.
8652

c.
6250601R

d.

9a. ORIGINATOR'S REPORT NUMBER(S)
ARPA Order No. 292
Amendment 20

9b. OTHER REPORT NO(S) (Any other numbers that may be assigned this report)
AFOSR 67-0519

10. DISTRIBUTION STATEMENT
Distribution of this document is unlimited

11. SUPPLEMENTARY NOTES

12. SPONSORING MILITARY ACTIVITY
AIR FORCE OFFICE OF SCIENTIFIC RESEARCH (SRPG)
1400 Wilson Blvd., Arlington, Va. 22209

13. ABSTRACT

The work performed under Contract AF 49(638)-1588 falls into (1) mode theory and applications and (2) scattering studies.

Crustal models have been constructed for TFO in Arizona and LASA in Montana.

A long period event recorded at TFO with epicenter in Southern California was time partitioned and Rayleigh wave dispersion in the frequency range of 0.025 to 0.175 was derived. By use of these data, the adequacy of the TFO model crust has been substantiated at low frequencies by a direct comparison of theoretical and experimental dispersion curves.

The mode separation studies include the design and application of mode separation processors to separate the M_{21} mode from the Rayleigh mode in the frequency range 0.0 to 0.25 cps by use of field data.

An analog model having a crustal layer with an abrupt thickness change (3 cm to 5 cm) was used for scattering studies. The source was located on the surface of the model. The dominant leaking mode of propagation in the thin end of the model is is PL_{22}. Theory predicts that this energy is primarily scattered into the leaking mode PL_{23} in the 5-cm end. There is also some evidence of wave propagation which is not readily explained in terms of modes.

Filtering techniques were used to analyze energy scattered by small surface irregularities. The primary scattered energy is a reflection of a portion of the incident Rayleigh wave.

14. KEY WORDS	LINK A		LINK B		LINK C	
	ROLE	WT	ROLE	WT	ROLE	WT
Mode Theory and Applications						
Scattering Studies						
Crustal Models for TFO and LASA						
Design and Application of Mode Separation Processors						
Analog Model of a Crustal Layer Having a Lateral Inhomogeneity						
Analysis of Energy Scattered by Small Surface Irregularities						